Side-polished and Tilted Fiber Bragg Grating Refractive Index Sensors for Structural Health Monitoring Applications

by
Chun-Fan Chan

A thesis submitted to the Faculty of Graduate Studies of
The University of Manitoba
in partial fulfilment of the requirements of the degree of

MASTER OF SCIENCE

Department of Electrical and Computer Engineering
University of Manitoba
Winnipeg

UNIVERSITY OF MANITOBA

THE UNIVERSITY OF MANITOBA

FACULTY OF GRADUATE STUDIES

*****

COPYRIGHT PERMISSION

Side-polished and Tilted Fiber Bragg Grating Refractive Index Sensors for Structural Health Monitoring Applications

BY

Chun-Fan Chan

A Thesis/Practicum submitted to the Faculty of Graduate Studies of The University of Manitoba in partial fulfillment of the requirement of the degree

MASTER OF SCIENCE

Acknowledgements

I would like to express my sincere appreciation and gratitude to my advisor, Dr. D.J. Thomson, for his advice, encouragement and insight throughout my research. I would also like to thank Dr. J. Albert (Carleton University, Ottawa, Canada) for his directions and advice. The work presented in this thesis would not have been possible without their guidance and support.

I would also like to acknowledge Dr. A. Vincelette (LxSix Photonics Inc.), Mr. P. Lefebvre (LxSix Photonics Inc.) and Dr. T. Coroy for their constant support and for providing me with tremendous knowledge in the field of fiber optic sensing. In addition, I would like to thank the ECE technicians, especially Mr. A. McKay, Mr. C. Smit, and Mr. D. Chrusch, for their assistance. I would like to thank LxSix Photonics Inc. (Montréal, Canada) and the Natural Sciences and Engineering Research Council of Canada for their financial assistance on this research project. I would also like to acknowledge Mr. S. Allard, Mr. J.F. Nadeau, Mr. G. Tourte, and Mr. S. Gagnon at LxSix Photonics Inc. for offering their assistance. Furthermore, I would like to acknowledge Mme. A. Laronche (Photonics Laboratory at Carleton University) for assisting me to manufacture the tilted fiber Bragg gratings for my research; as well as Mr. C. Chen for assisting me with Opti*Grating* simulation on the tilted fiber Bragg gratings.

Finally, I would like to thank my colleagues, friends, and my family for their continuous support and understanding.

Abstract

Fiber Bragg gratings are one of several fiber optic sensor technologies currently being used in structural health monitoring systems. When the effective index of a fiber Bragg grating is changed by external environmental variations (such as temperature, acidity, etc), the wavelength at which the incident light experiences a maximum reflection from the grating will correspondingly shift. To detect small environmental variations that occur during certain chemical processes, one can enhance the sensitivity using either side-polished or tilted fiber Bragg gratings. Enhanced sensitivity in each case is achieved by polishing the fiber on one side or writing the grating at some tilt angle. Side-polished grating sensors having a 1542 nm Bragg wavelength and cladding thickness values from 1–3 μm provide a maximum refractive index sensitivity of 7×10^{-4}. Tilted grating sensors having a 1566 nm Bragg wavelength and written at 4° tilt angle provide a maximum refractive index sensitivity of 5×10^{-5}. Experiments on the side-polished and tilted gratings were done by immersing the fiber sensors in solutions with the index range 1.31-1.44. Since tilted gratings have enhanced sensitivity and the advantage of maintaining their full mechanical strength, they show greater promise as reliable sensors for structural health monitoring applications.

Table of Contents

Acknowledgements i
Abstract ii
Table of Contents iii
List of Figures vi
List of Tables ix

Chapter 1 Introduction 1
1.1 Fiber-Optic Sensors 1
1.2 Outline of Research 3
1.3 Contribution of Research 5

Chapter 2 Background 6
2.1 Essential Theory of Optics 6
2.1.1 Light 6
2.1.2 Plane Waves in Matter 6
2.1.3 Reflection and Transmission of Light at an Interface 11
2.2 Optical Fibers 17
2.3 Fiber Bragg Gratings 21
2.3.1 Coupled-Mode Equations 24
2.3.2 Strain and Temperature Response of Fiber Bragg Gratings 26
2.3.3 Cladding and Radiation Mode Coupling 27
2.4 Tilted (Blazed) Fiber Bragg Gratings 29
2.5 Refractive Index Sensing via Fiber Bragg Gratings 31
2.5.1 Side-polished Fiber Bragg Gratings 32
2.5.2 Tilted Fiber Bragg Gratings for Refractive Index Sensing 34

Chapter 3 Simulation 37
3.1 Introduction 37

3.2 Simulation Geometry 37
3.3 Basic Simulation 40
3.3.1 Finite-Element Method 40
3.3.2 Opti*Grating* 42
3.4 Parameter Variation 45
3.5 Results 45

Chapter 4 Sensor Design and Fabrication 47
4.1 Introduction 47
4.2 Device Structure and Materials 47
4.3 Fabrication 49
4.3.1 Side-polished Fiber Bragg Grating 49
4.3.2 Tilted Fiber Bragg Grating 51
4.4 Chemical Etching 53

Chapter 5 Side-polished Fiber Bragg Gratings 55
5.1 Introduction 55
5.2 Characterization Tests 55
5.3 Sucrose Solution Tests 61
5.3.1 Experimental Setup and Procedure 61
5.3.2 Results and Analysis 65
5.4 Simulation Prediction versus Experimental Results 68

Chapter 6 Tilted Fiber Bragg Gratings 70
6.1 Introduction 70
6.2 Characterization Tests 70
6.3 Refractive Index Measurements via Sucrose Solutions 76
6.3.1 Experimental Setup and Procedure 76
6.3.2 Resonance Location Methods 78
6.3.3 Results 79
6.4 Refractive Index Measurements via Refractive Index Liquids 83

6.4.1 Experimental Setup and Procedure 83
6.4.2 Interrogation and Resonance Location Methods 84
6.4.3 Experimental Results 86
6.5 Simulation Prediction versus Experimental Results 90

Chapter 7 Summary and Conclusion 93
7.1 Refractive Index Sensitivity Comparison and Enhancement 93
7.2 Conclusion 95
7.3 Recommendations for Future Work 95

REFERENCES 97

List of Figures

Figure 2.1 Linear, circular, and elliptically polarized light. 9
Figure 2.2 Plane waves incident on the boundary between two homogeneous, isotropic, lossless dielectric media....12
Figure 2.3 Internal reflection and the critical angle....14
Figure 2.4 Propagation vectors for internal reflection....16
Figure 2.5 Total internal reflection of light through optical fiber. 18
Figure 2.6 Multimode and single-mode optical fibers....19
Figure 2.7 Illustration of a uniform fiber Bragg grating....22
Figure 2.8 Schematic transmission profile of fiber Bragg gratings showing cladding modes. 27
Figure 2.9 A schematic diagram of a tilted (blazed) fiber Bragg grating....30
Figure 2.10 Transmission spectrum of a fiber Bragg grating with a 4° tilt angle. 31
Figure 2.11 A schematic diagram of a side-polished fiber Bragg grating....32
Figure 3.1 Side-polished fiber simulation geometry (cross-sectional view). 38
Figure 3.2 Tilted grating simulation geometry 39
Figure 3.3 Bragg wavelength positions versus surrounding refractive index values. 42
Figure 3.4 Screenshot of an Opti*Grating* simulation plot. 43
Figure 3.5 Plot of simulation results and fitted curves. 44
Figure 3.6 Plot of Bragg wavelength versus external refractive index with different residual cladding thickness. 45
Figure 4.1 A typical side-polished fiber with cladding over the grating partially removed. 48
Figure 4.2 A fiber Bragg grating manufactured by exposing the fiber core to UV interference patterns through a phase mask. 50
Figure 4.3 Fiber Bragg grating reflection spectrum before and after side-polishing. 51
Figure 4.4 A fiber Bragg grating with its grating planes tilted at an angle θ with respect to the fiber axis. 52

Figure 4.5 Setup for chemical etching on the side-polished fiber Bragg grating sensor with *in-situ* monitoring. 54
Figure 5.1 FBG sensors held by a fiber holder ready for characterization testing. 56
Figure 5.2 Characterization experiment setup for side-polished FBG sensors. 57
Figure 5.3 Spectra of a side-polished FBG sensor in response to temperature variation. 58
Figure 5.4 Bragg wavelength versus temperature of side-polished FBG sensors. 60
Figure 5.5 U-shaped sensor probe design with the side-polished FBG sensor suspended. 62
Figure 5.6 Sucrose solution experiment setup for side-polished FBG sensors. 63
Figure 5.7 Experimental setup for side-polished FBG sensor involving IDERS™ SHM unit. 65
Figure 5.8 Spectra of a side-polished FBG sensor in different sucrose concentrations. 66
Figure 5.9 Side-polished FBG wavelength shift versus surrounding refractive index... 67
Figure 5.10 Side-polished experimental results compared with simulated data..... 68
Figure 6.1 Characterization experiment setup for tilted FBG sensors..... 71
Figure 6.2 Temperature-induced shift of tilted FBG spectrum. 72
Figure 6.3 Wavelength shifts of different modes versus temperature variation. 74
Figure 6.4 Tilted FBG sucrose solution experiment setup. 77
Figure 6.5 Differential response of cladding modes to surrounding refractive index. ... 80
Figure 6.6 Relative distances between cladding modes and the Bragg resonance versus sucrose concentration..... 80
Figure 6.7 Transmission spectra of a tilted FBG to different external refractive indices. 86
Figure 6.8 Relative distances between cladding modes and the Bragg resonance at different surrounding refractive index values (taken with JDS Uniphase swept wavelength system)..... 87
Figure 6.9 Relative distances between cladding modes and the Bragg resonance at different surrounding refractive index values (data taken with MicronOptics si720 interrogator). 89
Figure 6.10 Tilted FBG experimental data compared with Opti*Grating* simulation results. 91

Figure 6.11 Tilted FBG measured refractive index versus actual refractive index. 92

List of Tables

Table 2.1 Critical angles. 15
Table 3.1 Relative distances between selected cladding modes and the Bragg resonance at different surrounding refractive index values 44
Table 4.1 Summary of side-polished fiber design parameters 50
Table 4.2 Summary of tilted fiber Bragg grating design parameters 53
Table 5.1 Characterization test conditions 56
Table 5.2 Summary of Bragg wavelengths in response to temperature/humidity variation. 59
Table 6.1 Summary of temperature-induced wavelength shifts of Bragg and select cladding modes of different diameter fibers. 75
Table 7.1 Summary of refractive index sensitivities of the fiber modes analyzed. 93

Chapter 1

Introduction

1.1 Fiber-Optic Sensors

As structural health monitoring continues to grow as a field of increasing interest for civil engineers, fiber optic sensor technology is a promising alternative to conventional sensors. Traditionally used in the telecommunications field, optical fibers have garnered interest in other fields due to their inherent advantages such as compact size, low loss, rapid response, resistance to corrosion, and electromagnetic interference immunity. Fiber optic sensors have been used in a wide range of applications such as strain measurements in civil infrastructure [1], oil pipeline monitoring [2], and composite structures [3].

Structural health monitoring of civil infrastructure has been a growing issue over the past decade. As structures continue to age and become damaged by fatigue and corrosion, it becomes increasingly important to create a reliable monitoring system in order to assess their structural integrity. Thus, to successfully monitor the condition of a structure, the measurement device must be able to provide reliable and accurate data over long periods of time. A suitable measurement device must also meet many requirements including high sensitivity to the desired parameter such as corrosion and signal stability as well as minimal cross-sensitivity to other changes in the environment, such as temperature and humidity [4]. The measurement technique should allow multiple sensors to be placed on a structure which will provide a thorough profiling of the corrosion distribution.

Fiber optic sensors are classified according to the sensing technique by which they operate. These techniques are based on modulating the intensity, phase, or polarization of the light passing through the sensor. Fiber sensors are now being used to monitor various parameters such as strain, temperature, pressure, and with some modification they can be used to monitor chemical composition as well as corrosion. One optical technique used to measure corrosion is the combined use of polymer chemical-transducer and refractometry [5]. A polymer material absorbs target analytes and changes its index of refraction, one of the main physical properties. By measuring the refractive index change in the polymer, the corresponding chemical change is detected. Refractometry is the method of assessing the composition or purity substances by measuring their refractive index, and it is used in many important areas including industrial process monitoring, quality control in the food industry, and biomedical applications. Most refractometers in use today are derived from the Abbe refractometer [6]. This instrument measures refractive indices of liquids and solids by determining changes in the angle of total internal reflection for a high index prism on which the material with the unknown refractive index is placed in contact. While these instruments can be very accurate they cannot be used in structural health monitoring because of their size and they are unable to be embedded in civil infrastructure. Therefore fiber optic versions have been developed for this purpose, in which the sensor is a fiber Bragg grating embedded in the core of the fiber [4, 7-14].

The purpose of the research work in this thesis is to develop a chemical sensing platform based on fiber Bragg gratings that can be applied to the field of structural health monitoring. The main sensor concept involves the use of fiber Bragg gratings as

refractive index sensors. These refractive index sensors may then be applied to structural health monitoring with a suitable chemically reactive polymer (whose refractive index changes when exposed to target chemical analytes). In this research, the refractive index sensing concept was tested using side-polished and tilted fiber Bragg gratings [15-17]. Details of this research work will be described later in this thesis.

1.2 Outline of Thesis

An overview of the essential background on fiber optics and fiber Bragg grating technology is presented in Chapter 2. The overview includes the essential theories of optics, uniform fiber Bragg gratings and tilted fiber Bragg gratings, and how they can be used as refractive index sensors to be potentially applied in structural health monitoring. A review of the simulations done on the two fiber Bragg grating technologies of interest, the side-polished fiber Bragg grating and the tilted fiber Bragg grating, is presented in Chapter 3. The simulation geometries, along with the rationale behind the chosen simulation geometries, are also presented in Chapter 3. Furthermore, simulation parameters were varied to observe the effect of changing the surrounding environment. A discussion of the simulation results will be presented in the end of Chapter 3.

A description of the sensor design and fabrication is presented in Chapter 4. Side-polishing the fiber Bragg grating is briefly described, as well as the specifications of the grating designs. Tilted Bragg grating fabrication is also outlined in brief, including the angles of the tilt and the type(s) of optical fibers used. Chemical etching is also described in this Chapter to demonstrate a method to enhance the sensor's sensitivity.

Experiments pertinent to side-polished fiber Bragg gratings are described in detail

in Chapter 5. This chapter begins with the results and analysis of the temperature/humidity characterization tests, followed by a description of the sucrose solution tests. Experimental apparatus and the interrogation equipment, as well as the peak location methods are presented. Result analysis includes a comparison between the experimental results and the simulation prediction, and possible reasons for any discrepancy.

Tilted fiber Bragg grating experiments are detailed in Chapter 6. This chapter begins with the temperature/humidity characterization test results and analysis, followed by a detailed description of the refractive index measurement tests done using highly calibrated refractive index liquids. Interrogation systems used, the advantages and disadvantages of the equipment are presented. The peak location method, different from that of the side-polished fiber Bragg gratings, is also described. The sucrose solution tests performed on the tilted fiber Bragg gratings are also presented, including the apparatus and the controlled experimental conditions. The results are compared with simulation to verify the theoretical model and computer software used to carry out the simulation task.

In Chapter 7, a summary of the findings is presented and a refractive index sensitivity comparison is presented. Conclusions as to the use of the side-polished fiber Bragg grating and tilted fiber Bragg grating technologies are drawn. This chapter concludes with recommendations for future work in this area.

1.3 Contribution of Research

Investigating a suitable optical fiber Bragg grating, refractometry based platform for future use in chemical sensing and structural health monitoring is the core work of this thesis. Methods to enhance the refractive index sensitivity and locating the resonance peak locations accurately, as well as a study on the capabilities of several equipment used for interrogation, are also significant contributions of the research work presented in this thesis.

Chapter 2

Background

2.1 Essential Theory of Optics

2.1.1 Light

Light may be considered in three different ways [18]; the appropriate viewpoint depends on the nature of the phenomenon to be understood.

- Light is composed of photons, vectors of energy exchange, which can explain absorption, emission, and related phenomena.
- Light is an electromagnetic wave that can propagate and be diffracted in a non-dispersive medium without energy exchange.
- Light is composed of luminous rays that obey the principles of geometrical optics.

In this research, emphasis is placed on the electromagnetic wave and geometric optics models to better understand the phenomena exploited to create a sensor technology. Thus, only the latter two of the three viewpoints will be discussed in detail in the next two sections.

2.1.2 Plane Waves in Matter

Light can be considered as an electromagnetic wave. A wave is a vibratory phenomenon that propagates with a given velocity and is hence a varying function of time. An electromagnetic wave can be represented by an oscillation in a given plane that propagates in a direction normal to the plane. In free space, the velocity c of an electromagnetic wave or light in a vacuum is related to two physical constants, the

electrical permittivity ε_o and the magnetic permeability μ_o:

$$c = (\varepsilon_o \cdot \mu_o)^{-1/2} \tag{2.1}$$

Inside a solid matter, the speed of light is reduced by

$$v = c/n \tag{2.2}$$

where v is the speed of light in the matter and n is the index of refraction of the matter. In a homogeneous medium, the wave velocity is

$$\varepsilon \cdot \mu \cdot v^2 = 1 \tag{2.3}$$

where ε and μ are the electric permittivity and the magnetic permeability of the medium, respectively, and are complex in general. The index of refraction, $\tilde{n}$, of a medium is related to its electric permittivity and magnetic permeability by

$$\tilde{n} = c \cdot (\varepsilon \cdot \mu)^{-1/2} \tag{2.4}$$

Since the electric permittivity and the magnetic permeability may generally be complex, this shows that the index of refraction can be complex as well. The complex index of refraction can be written as

$$\tilde{n} = n\,(1 - i\kappa) \tag{2.5}$$

where κ is called the attenuation index or absorption index. In this thesis from this point on, the discussion will only focus on dielectric media whose refractive indices are real. The wavelength λ is related to this velocity and the frequency f by

$$\lambda = v/f = c/nf \tag{2.6}$$

hence $\lambda_o = c/f$ in a vacuum ($n = 1$).

A complete mathematical description of electromagnetic waves and their propagation is provided by the well-known Maxwell's equations. The wave equations for **E** and **H** in a medium, derived from Maxwell's equations, are as follows:

$$\nabla^2\mathbf{E} - \mu\varepsilon\frac{\partial^2\mathbf{E}}{\partial t^2} = 0;\ \nabla^2\mathbf{H} - \mu\varepsilon\frac{\partial^2\mathbf{H}}{\partial t^2} = 0 \tag{2.7}$$

Plane wave solutions to equation (2.7) exist in the form of

$$\mathbf{E} = \mathbf{E}_o e^{i(\omega t - \mathbf{k}\cdot\mathbf{r} + \varphi\, e)} \tag{2.8a}$$

$$\mathbf{H} = \mathbf{H}_o e^{i(\omega t - \mathbf{k}\cdot\mathbf{r} + \varphi\, b)} \tag{2.8b}$$

Where ω is the angular frequency and $\mathbf{k} = k_x + k_y + k_z$ is the propagation vector (or wave vector) and that $k^2 = k_x^2 + k_y^2 + k_z^2 = \mu\varepsilon\omega^2$. (This shows that $\mathbf{k}$ is, in general, complex.) From equation (2.4), the propagation constant k can be rewritten as

$$k = \tilde{n}\frac{\omega}{c} \tag{2.9}$$

In the case of dielectric media

$$k = n\frac{\omega}{c} \tag{2.10}$$

Polarization

Because the electric field is a vector quantity, both its magnitude and direction must be specified. Consider a plane wave with wave vector $\mathbf{k}$. The electric field $\mathbf{E}$ may point to any direction perpendicular to $\mathbf{k}$, and $\mathbf{H}$ is along the vector $\mathbf{k} \times \mathbf{E}$. Let k be along the z-axis, the monochromatic wave can be written in the form

$$\mathbf{E}(x, y, z, t) = E_x\hat{\mathbf{x}} + E_y\hat{\mathbf{y}} \tag{2.11}$$

where

$$E_x(x, y, z, t) = A_x \cos(\omega t - kz + \phi_x) \tag{2.12}$$

$$E_y(x, y, z, t) = A_y \cos(\omega t - kz + \phi_y) \tag{2.13}$$

with positive real amplitudes A_x, A_y, and phase angles ϕ_x and ϕ_y. The classification of

the types of polarized light will depend on the relative phase

$$\phi = \phi_y - \phi_x \tag{2.14}$$

and on the relative sizes of A_x and A_y.

a) Linearly polarized light: results when $\phi = 0$ or $\phi = \pi$ for then E_y is proportional to E_x. At a fixed position z, the electric field undergoes simple harmonic motion along a line (Figure 2.1a).

b) Circularly polarized light: $A_x = A_y$ and $\phi = \pm\pi/2$. At a fixed point z, the electric field describes a circle (Figure 2.1b).

c) Elliptically polarized light: $A_x \neq A_y$ and $\phi \neq \pm\pi, 0$. This is the general case where at a fixed point z, the electric field traces out an ellipse (Figure 2.1c).

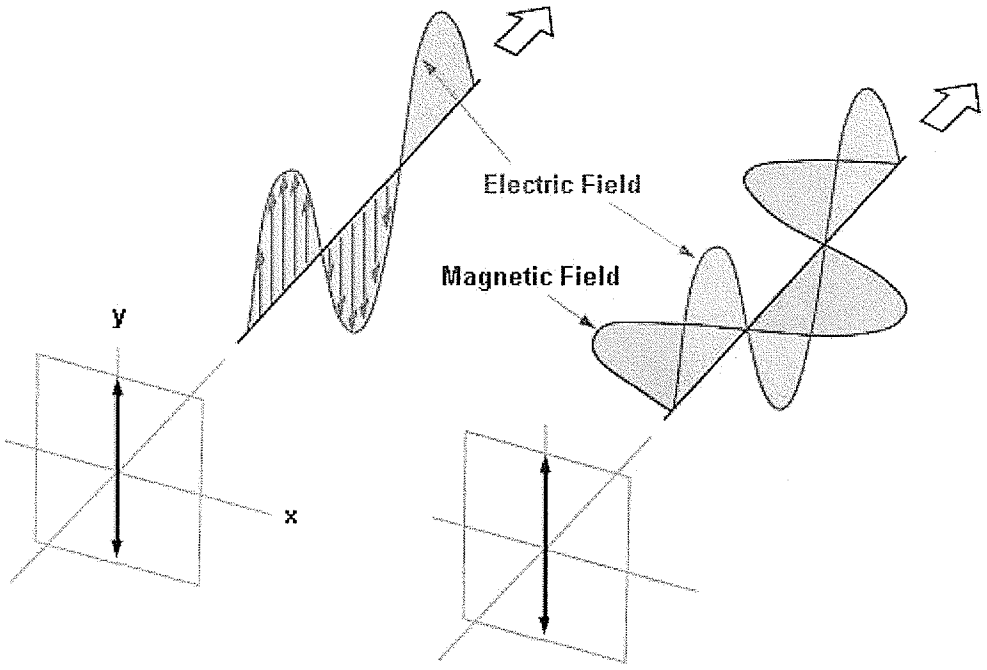

Figure 2.1a Linearly polarized light.

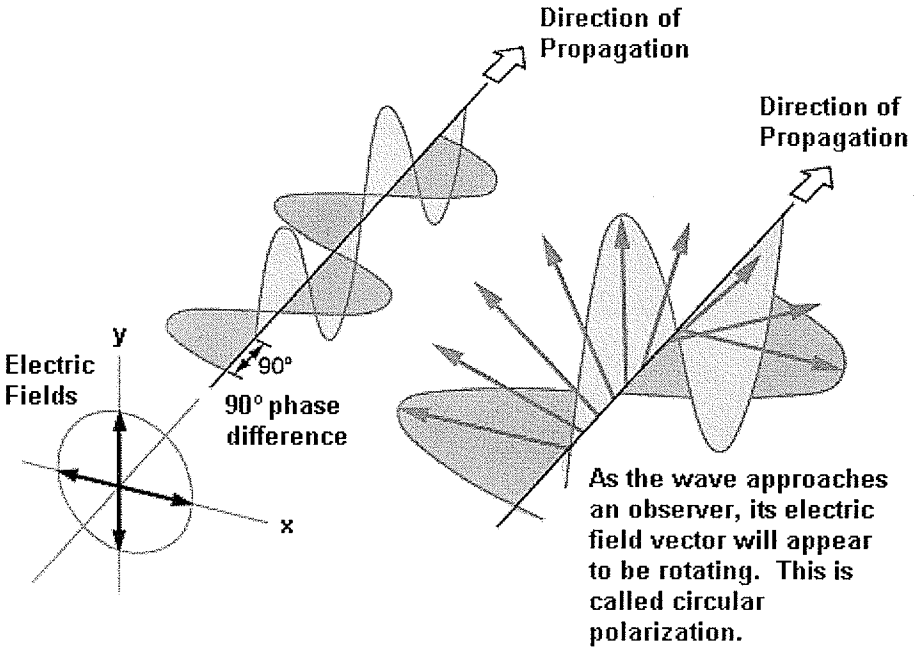

Figure 2.1b Circularly polarized light.

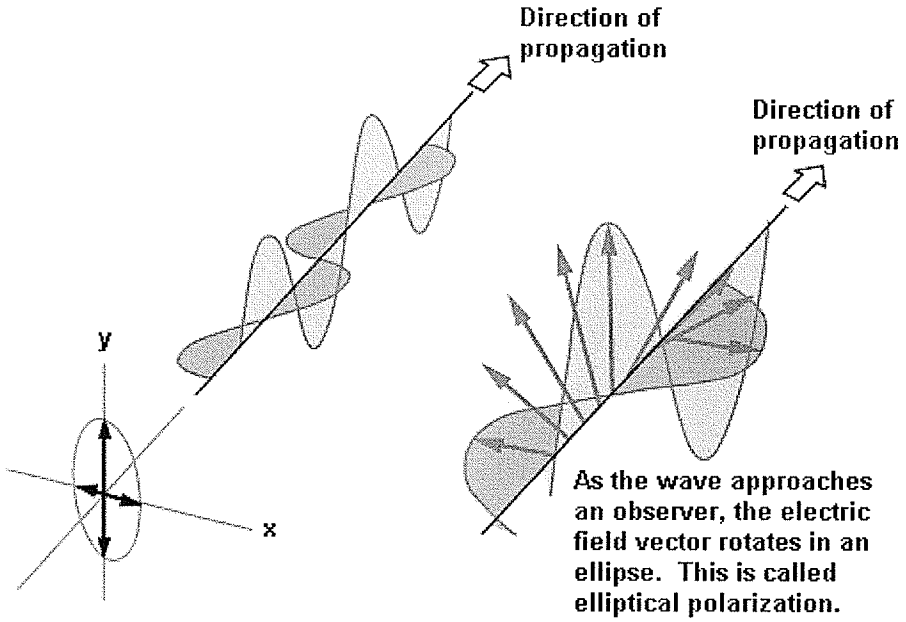

Figure 2.1c Elliptically polarized light.

2.1.3 Reflection and Transmission of Light at an Interface

Suppose that the incident monochromatic light wave is planar, so that it has the form

$$\mathbf{E}_i = \mathrm{E}_{oi} e^{i(\omega_i t - \mathbf{k}_i \cdot \mathbf{r})} \tag{2.15}$$

or more simply,

$$\mathbf{E}_i = \mathrm{E}_{oi} \cos(\omega_i t - \mathbf{k}_i \cdot \mathbf{r}) \tag{2.16}$$

Assume that E_i is linearly polarized, meaning that E_{oi} is constant in time. From the previous section it is obvious that any form of light can be represented by two orthogonal linearly polarized waves; hence, the above assumption imposes no restriction. Making no assumptions about their directions, frequencies, wavelengths, phases, or amplitudes, the reflected and transmitted waves can be written as

$$\mathbf{E}_r = \mathrm{E}_{or} \cos(\omega_r t - \mathbf{k}_r \cdot \mathbf{r} + \phi_r) \tag{2.17}$$

and

$$\mathbf{E}_t = \mathrm{E}_{ot} \cos(\omega_t t - \mathbf{k}_t \cdot \mathbf{r} + \phi_t) \tag{2.18}$$

where ϕ_r and ϕ_t are phase constants relative to $\mathbf{E}_i$. Figure 2.2 depicts the waves in the vicinity of the planar interface between two homogeneous lossless dielectric media of indices n_i and n_t.

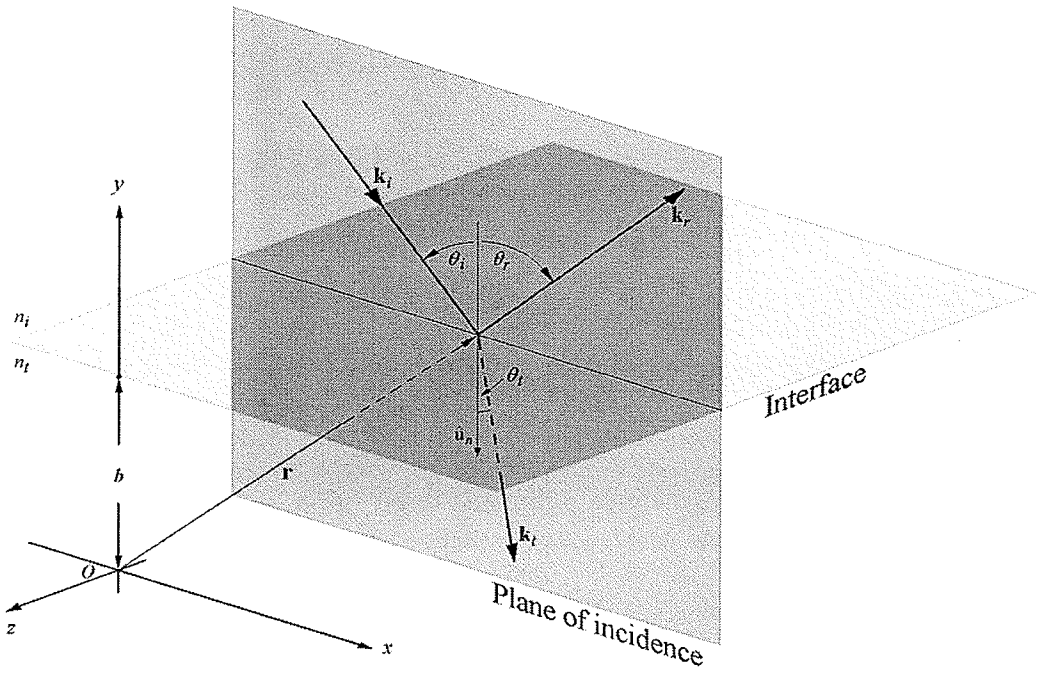

Figure 2.2 Plane waves incident on the boundary between two homogeneous, isotropic, lossless dielectric media.

The laws of electromagnetic theory lead to certain requirements that must be met by the fields, referred to as the boundary conditions. By imposing these conditions, it leads to

$$\omega_i = \omega_r = \omega_t = \omega \tag{2.19}$$

This means that the reflected light and the transmitted light waves have the same frequency as the incident wave. Furthermore,

$$\left(\mathbf{k}_i \cdot \mathbf{r}\right)\Big|_{y=0} = \left(\mathbf{k}_r \cdot \mathbf{r} + \phi_r\right)\Big|_{y=0} = \left(\mathbf{k}_t \cdot \mathbf{r} + \phi_t\right)\Big|_{y=0} \tag{2.20}$$

The reflected light wave lies in the same plane as the incident wave and in the same medium, $k_r = k_i$. This means that the angle of reflection θ_r is equal to the angle of incidence θ_i. This is the law of reflection:

$$\theta_r = \theta_i \tag{2.21}$$

Then, from

$$\left[(\mathbf{k}_i - \mathbf{k}_t)\cdot\mathbf{r}\right]_{y=0} = \phi_t \tag{2.22}$$

Tangential components of k_i and k_t must be equal, or

$$k_i \sin\theta_i = k_t \sin\theta_t \tag{2.23}$$

Since $\omega_i = \omega_t = \omega$, this leads to Snell's law of refraction

$$n_i \sin\theta_i = n_t \sin\theta_t \tag{2.24}$$

2.1.3.1 Total Internal Reflection

Laws of reflection and refraction help to predict the behaviour of light waves as they encounter an interface between two dielectric media. Now assume a lightwave propagating in a medium with a refractive index n_i, towards an interface with a second medium having a refractive index n_t; and assume that $n_i > n_t$. This presents an interesting case because when θ_i increases gradually, as depicted in Figure 2.3, from the Fresnel equations (described in detail in numerous other literature [19-23]), the reflection coefficients

$$\rho_\sigma = \frac{n_i\cos\theta_i - n_t\cos\theta_t}{n_i\cos\theta_i + n_t\cos\theta_t} \quad (\sigma - \text{polarization}) \tag{2.25}$$

$$\rho_\pi = \frac{n_t\cos\theta_i - n_i\cos\theta_t}{n_i\cos\theta_i + n_t\cos\theta_t} \quad (\pi - \text{polarization}) \tag{2.26}$$

increase with increasing θ_i; therefore, the reflectance increases while the transmittance decreases with increasing θ_i. Moreover, $\theta_t > \theta_i$, thus as θ_i becomes larger, the transmitted ray gradually approaches tangency with the boundary, and as it does so more and more of the available energy appears in the reflected beam. Finally, when $\theta_t = 90°$, $\sin\theta_t = 1$ and

$$\sin \theta_c = n_t/n_i \tag{2.27}$$

Or in other words, the critical angle is that special value of incident angle for which the transmitted angle equals 90°. For incident angles greater than the critical angle, all the incoming energy is reflected back into the incident medium in the process known as total internal reflection.

The critical angle for air-glass interface is roughly 42° (See Table 2.1), 48.6° for air-water interface, and the critical angle for a typical single-mode optical fiber is roughly 84° (n_{core} = 1.4507 and n_{clad} = 1.444025).

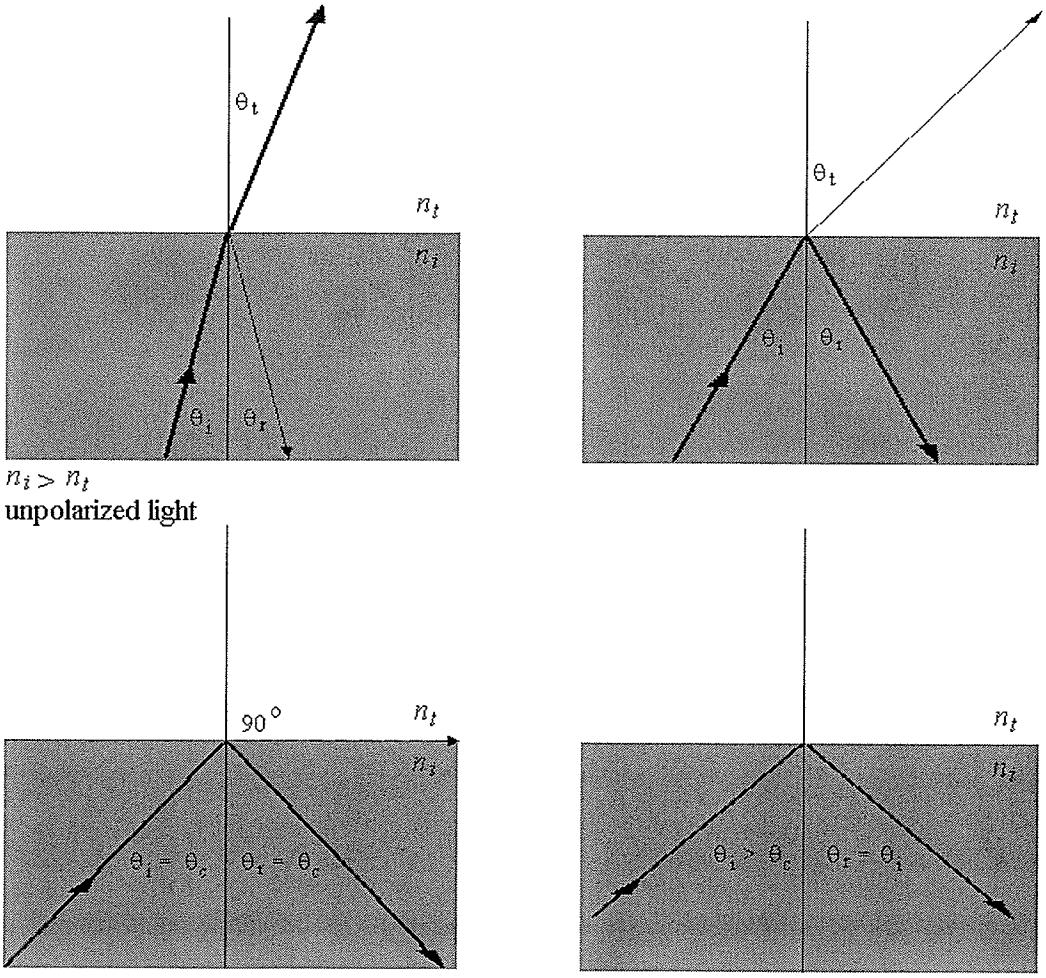

Figure 2.3 Internal reflection and the critical angle.

Table 2.1 Critical angles.

n_t/n_i	θ_c	n_t/n_i	θ_c
1.31	49.7612	1.46	43.2302
1.32	49.2509	1.47	42.8649
1.33	48.7535	1.48	42.5066
1.34	48.2682	1.49	42.1552
1.35	47.7946	1.50	41.8103
1.36	47.3321	1.51	41.4718
1.37	46.8803	1.52	41.1395
1.38	46.4387	1.53	40.8132
1.39	46.0070	1.54	40.4927
1.40	45.5847	1.55	40.1778
1.41	45.1714	1.56	39.8683
1.42	44.7670	1.57	39.5642
1.43	44.3709	1.58	39.2652
1.44	43.9830	1.59	38.9713
1.45	43.6028	1.60	38.6822

2.1.3.2 Evanescent Field

If one assumes that there is no transmitted wave in total internal reflection, it becomes impossible to satisfy the boundary conditions required by the electromagnetic theory using only the incident and reflected waves. A detailed derivation and computation to demonstrate how the boundary conditions are met is described in other literature [20, 21]. This section presents a simple formulation.

The wave function for the transmitted electric field is

$$\mathbf{E}_t = E_{ot} \cos(\omega_i t - \mathbf{k}_t \cdot \mathbf{r}) \tag{2.28}$$

where

$$\mathbf{k}_t \cdot \mathbf{r} = k_{tx}x + k_{tz}z \tag{2.29}$$

there being no y-component of $\mathbf{k}$. But

$$k_{tx} = k_t \sin\theta_t \tag{2.30a}$$

and

$$k_{tz} = k_t \cos\theta_t, \tag{2.30b}$$

as seen in Figure 2.4. Once again, using Snell's law and the trigonometric identity,

$$k_t \cos\theta_t = \pm k_t \sqrt{\left(1 - \frac{n_i^2 \sin^2\theta_i}{n_t^2}\right)}. \tag{2.31}$$

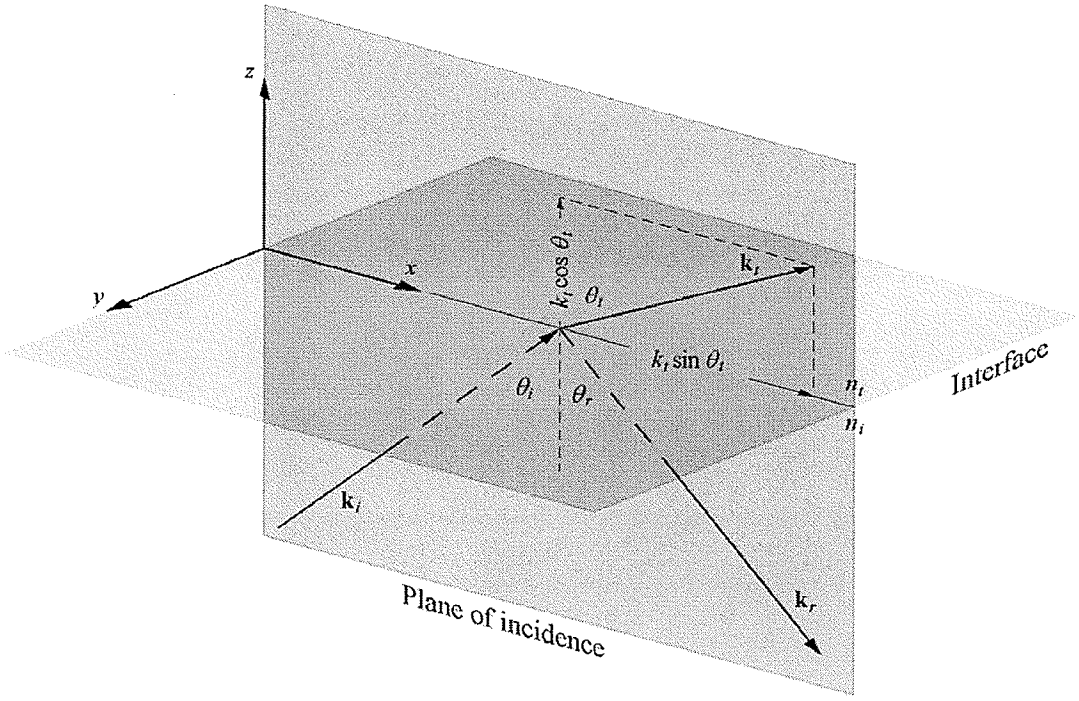

Figure 2.4 Propagation vectors for internal reflection.

Since $\sin\theta_i > n_t/n_i$ in total internal reflection,

$$k_{tz} = \pm i k_t \sqrt{\left(\frac{n_i^2 \sin^2\theta_i}{n_t^2} - 1\right)} = \pm i\beta \tag{2.32}$$

and

$$k_{tx} = \frac{n_i k_t}{n_t} \sin\theta_i \tag{2.33}$$

Hence,

$$\mathbf{E}_t = \mathrm{E}_{ot} e^{-\beta z} e^{i(\omega t - x k_x)} \tag{2.34}$$

The negative sign in Eq (2.32) in front of β is dropped because it has no physical meaning as the electromagnetic wave must not be exponentially increasing. The transmitted wave has a skin depth given by

$$\delta = \frac{1}{\beta} = \frac{\lambda_o}{2\pi\sqrt{n_i^2 \sin^2\theta_i - n_t^2}} \tag{2.35}$$

This wave, whose amplitude drops off exponentially as it penetrates the second medium, advances in the *x*-direction as an evanescent wave.

2.2 Optical Fibers

Optical fibers are the basic elements in optical sensing, and an understanding of their characteristics is essential for the work described in this thesis. An optical fiber can be thought of as a long rod of transparent material (a cylindrical dielectric structure) consisting of an inner core whose refractive index, n_{co}, is higher than the refractive index, n_{clad}, of the outer cladding, as shown in Figure 2.5. Optical fibers guide light waves based on total internal reflection as described in the earlier section. Total internal reflection takes place at the walls of the core-cladding interface, and the propagating light is confined within the core.

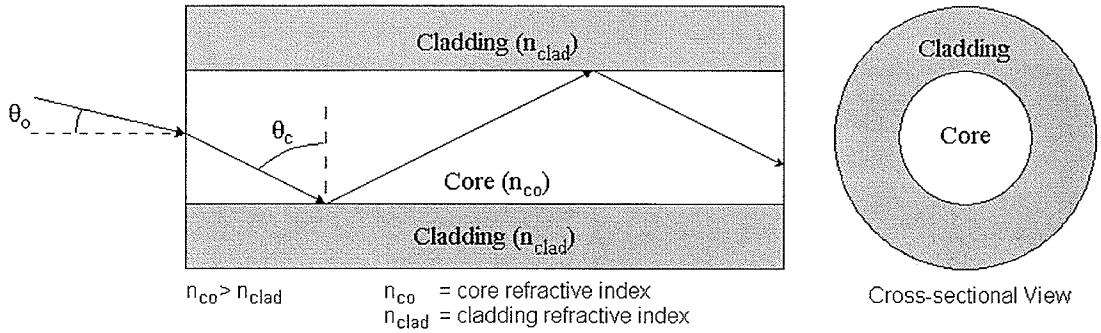

Figure 2.5 Total internal reflection of light through optical fiber.

From Snell's laws, the angle of reflection θ at the core-cladding interface is greater than the critical angle θ_c. Light, which is injected into the fiber at an angle θ_o smaller than the limiting angle θ_{lim}, will be totally internally reflected at the core-cladding interface. The numerical aperture (NA) is defined by this limiting value of the acceptance angle at the input to the fiber:

$$NA = n_o \sin \theta_{lim} = (n_{co}^2 - n_{clad}^2)^{1/2} \qquad (2.36)$$

Increasing the refractive index difference between the core and the cladding of the fiber increases the acceptance angle and the numerical aperture. A large acceptance angle gives rise to a large number of rays with different reflection angles (i.e. different transmission modes), which propagate down the fiber.

Optical fibers can be created in different sizes to accommodate various applications. However, it is the size of the core that affects the way light travels through it. The size of the core is small compared to the cladding and can range from 6 to 100 μm. Light rays can travel different paths in the fiber because the incident angles determine how the rays will propagate. For optical fibers with core sizes in the range of 50 to 100 μm, several ray paths or modes can be supported (see Figure 2.6). These types

of fibers are called multimode and since the travel time of different modes can vary, the rays exiting the fiber will become out of sync. Therefore, narrow pulse sent into the fiber start to broaden and exit the fiber wider than the original signal. This effect is called intermodal dispersion and it limits the fiber bandwidth and the maximum pulse rate the fiber can handle.

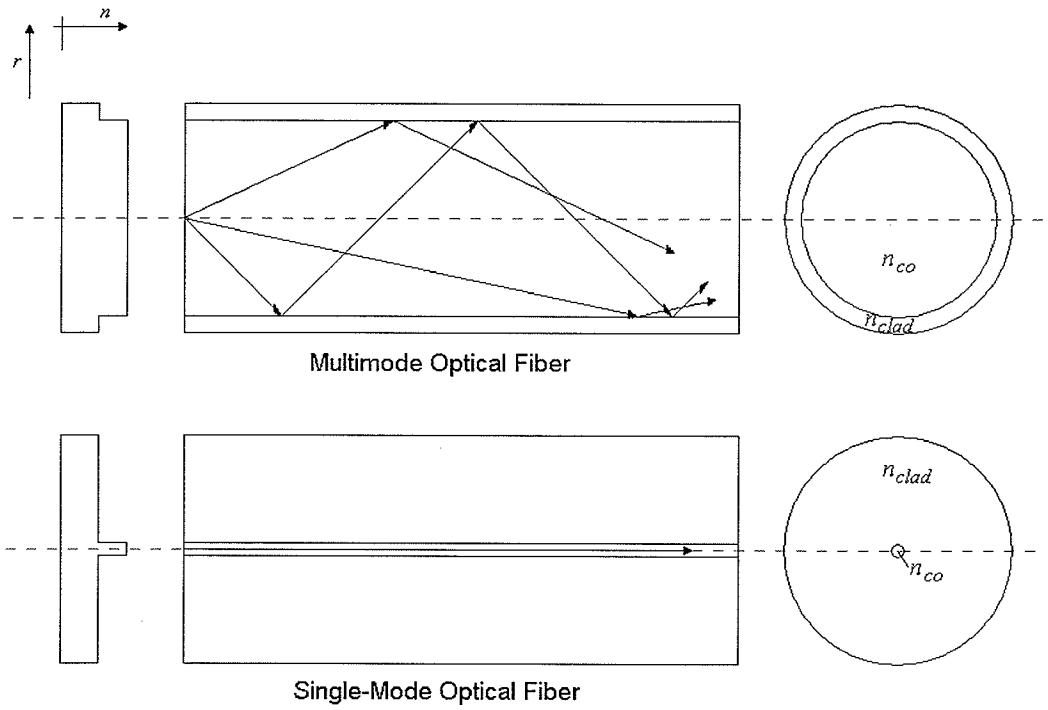

Figure 2.6 Multimode and single-mode optical fibers.

On the other hand, single-mode fibers have core sizes less than 10 μm which produces a condition in which only a single electromagnetic mode propagates. As a result, single-mode fibers have a broader bandwidth than multimode fibers and experience less attenuation as well. Therefore, this type of fiber is better suited for sensor and transmission purposes. The number of modes that can be supported by a fiber is calculated using the fiber's normalized frequency, V. This frequency is expressed as

$$V = \frac{(\pi d_{fiber} \mathrm{NA})}{\lambda} \tag{2.37}$$

where d_{fiber} is the diameter of the fiber core. For $V < 2.405$, only one mode will propagate down the fiber, which then becomes known as single-mode fiber.

Modifications to the cylindrical conventional fiber geometry yield different properties that one may take advantage of. For example, polishing off one side of the optical fiber cladding, making a D-shaped fiber, allows the evanescent field to penetrate the surrounding medium and coupling between the guided waves in the core and the environment surrounding the polished side. This technique is useful in detecting refractive index changes in the environment and has been used, in conjunction with a thin-film polymer deposited on the polished side, to detect changes in humidity [24, 25]. This technique is also used in this research, and will be described later.

Evanescent Modes

Evanescent modes describe those of evanescent fields arising from total internal reflection in an optical fiber core-cladding interface (see section 2.1.3.2). These modes decay exponentially with distance from the interface. With standard optical fibers having a cladding thickness much larger than that of the core diameter, these modes essentially have no effect on the optical fiber core mode. Their existence, however, constitutes an important factor in determining the power confinement factor in an optical fiber – the portion of optical power that is guided in the core of an optical fiber as a ratio of the total optical power sent in the optical fiber.

Although in standard optical fibers and their applications, the effect of evanescent modes are negligible; however, there are applications, particularly in optical sensing,

where effects of evanescent modes are desirable. This can be achieved by reducing the cladding surrounding the optical fiber core, allowing the evanescent fields to penetrate deep into the surrounding medium before it vanishes. This will be described in detail later in this Chapter.

2.3 Fiber Bragg Gratings

This section is concerned with the main sensing mechanism used in this research: the fiber Bragg gratings. This section focuses on the propagation of light in Bragg grating structures in the low intensity regime where optical non-linearities are negligible.

A fiber Bragg grating is comprised of a periodic modulation of the refractive index in the core of a single-mode fiber [26]. Bragg gratings are fabricated using different methods. One method involves placing a mask pattern over the optical fiber and shining ultraviolet (UV) light through it to change the refractive index of the core. Another method makes use of two UV beams shining onto the core of the fiber to produce a refractive index modulation as a result of the UV beam interference pattern. The advantage of a Bragg grating is it is very flexible to work with in terms of being able to choose the wavelength range one would want to use. Since the Bragg wavelength depends on the spacing between the gratings, it is possible to create gratings at different wavelengths. The refractive index modulation is on the order of 10^{-4} to 10^{-3}. Therefore, it takes a large number of periods to increase the reflection to over 90% which is usually desired. The number of grating periods will also determine the bandwidth (full-width-half-maximum) of the reflected peak, and this will be shown later in this section.

These types of uniform fiber gratings, where the phase fronts are perpendicular to

the fiber's longitudinal axis and with grating planes having constant period (Figure 2.7), are considered the fundamental building blocks for most Bragg grating structures. Light, guided along the core of an optical fiber, will be scattered by each grating plane. If the Bragg condition is not satisfied, the reflected light from each of the subsequent planes becomes progressively out of phase and will eventually cancel out. Additionally, light that is not coincident with the Bragg wavelength resonance will experience very weak reflection at each of the grating planes because of the index mismatch. This reflection accumulates over the length of the grating. Where the Bragg condition is satisfied, the contributions of reflected light from each grating plane add constructively in the backward direction to form a back-reflected peak with a center wavelength defined by the grating parameters.

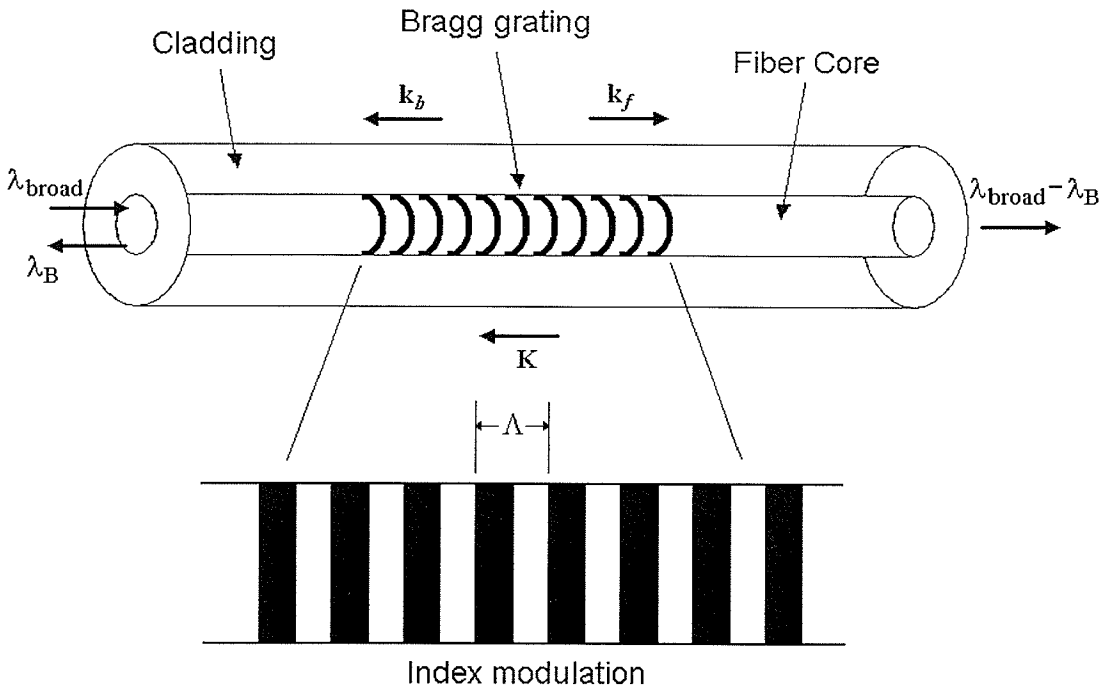

Figure 2.7 Illustration of a uniform fiber Bragg grating having constant index modulation amplitude and period, with the incident, diffracted, and grating wave vectors for momentum conservation.

The Bragg grating condition is simply the requirement that satisfies both energy and momentum conservation. Energy conservation requires that the frequency of the incident radiation and the reflected radiation is the same, or

$$h\nu_f = h\nu_b \tag{2.38}$$

Momentum conservation requires that the incident wave vector, $\mathbf{k}_f$, plus the grating wave vector, $\mathbf{K}$, equal the wave vector of the back-reflected radiation $\mathbf{k}_b$. This is simply stated as [27]

$$\mathbf{k}_f + \mathbf{K} = \mathbf{k}_b \tag{2.39}$$

where the grating wave vector, K, has a direction perpendicular to the grating planes with a magnitude $2\pi/\Lambda$ (Λ is the grating spacing shown in Figure 2.7). The back-reflected wave vector is equal in magnitude, but opposite in direction, to the incident wave vector. Therefore, the momentum conservation becomes

$$2\left(\frac{2\pi n_{\text{eff}}}{\lambda_B}\right) = \frac{2\pi}{\Lambda} \tag{2.40}$$

which simplifies to the first-order Bragg condition

$$\lambda_B = 2n_{\text{eff}}\Lambda \tag{2.41}$$

where the Bragg grating wavelength, λ_B, is the free space center wavelength of the input light that will be back-reflected from the Bragg grating, and n_{eff} is the effective refractive index of the guided fundamental (LP_{01}) mode at the free space center wavelength. This means that changes in the effective refractive index or the grating spacing induced by external factors results in a change in the Bragg condition, thus causing a shift in the back-reflected center wavelength. It is for this precise reason that fiber Bragg gratings

have been used for sensing applications.

Another important parameter here is the bandwidth of the reflected peak. This bandwidth is determined by the number of periods present in a Bragg grating. A general expression for the approximate full-width-half-maximum bandwidth of a grating is given by [28]:

$$\Delta\lambda = \lambda_B s \sqrt{\left(\frac{\Delta n}{2n_o}\right)^2 + \left(\frac{1}{N}\right)^2} \tag{2.42}$$

where s is the fringe visibility [29] and is approximately 1 for strong grating (near 100% reflection) and approximately 0.5 for weak gratings. The average refractive index of the core is denoted as n_o and the amplitude of the refractive index modulation is denoted as Δn. From (2.42), it can be seen that larger number of grating periods gives rise to narrower resonance peaks given the same refractive index modulation.

2.3.1 Coupled-Mode Equations

Aside from the energy and momentum conservation analysis of fiber Bragg gratings described earlier, one powerful technique for obtaining quantitative information about the diffraction efficiency and spectral dependence of fiber gratings is the coupled-mode theory. It is one of the most popular techniques utilized in describing the behaviour of Bragg gratings, mainly due to its simplicity and accuracy in modeling the optical properties of most fiber gratings of interest. A complete derivation of the coupled mode equations are described in other texts [30, 31] and thus will not be described in detail in this thesis.

Coupled-mode equations describe the interaction between the forward and

backward (reflected) waves. The grating itself has a periodic variation in its refractive index, so for incident waves close to the Bragg grating wavelength, there is a near fully constructive interference, and thus the dominant interaction lies near the wavelength for which reflection occurs from a mode of amplitude $A(z)$ into an identical counter-propagating mode of amplitude $B(z)$. The coupled-mode equations are given by [32]

$$\frac{dA^+}{dz} = i\zeta^+ A^+(z) + i\kappa B^+(z) \tag{2.43a}$$

$$\frac{dB^+}{dz} = -i\zeta^+ B^+(z) - i\kappa A^+(z) \tag{2.43b}$$

where $A^+(z) = A(z)\exp(i\delta_d z - \varphi/2)$, $B^+(z) = B(z)\exp(-i\delta_d z + \varphi/2)$, and ζ^+ is the general self-coupling coefficient defined as

$$\zeta^+ = \delta_d + \zeta - \frac{1}{2}\frac{d\varphi}{dz} \tag{2.44}$$

with δ_d being the detuning, which is independent of z and is defined in the following way:

$$\begin{aligned} \delta_d &= \beta - \frac{\pi}{\Lambda} \\ &= 2\pi n_{eff}\left[\frac{1}{\lambda} - \frac{1}{\lambda_B}\right] \end{aligned} \tag{2.45}$$

here $\lambda_B = 2n_{eff}\Lambda$ is the designed Bragg reflection wavelength. For a single-mode uniform Bragg grating with no grating chirp, $d\varphi/dz = 0$ and the average index change, δn_{eff}, is constant, and

$$\zeta = \frac{2\pi}{\lambda}\delta n_{eff} \tag{2.46}$$

$$\kappa = \frac{\pi}{\lambda} s\delta n_{eff} \tag{2.47}$$

The reflection spectrum is given by the equation

$$R = \frac{\sinh^2 \sqrt{(\kappa L)^2 - (\zeta^+ L)^2}}{-\frac{\zeta^{+2}}{\kappa^2} + \cosh \sqrt{(\kappa L)^2 - (\zeta^+ L)^2}} \tag{2.48}$$

where L is the grating length. With some manipulation with the above equation, one finds that the maximum reflectivity occurs when the detuning parameter equals zero. That is, the reflection spectrum has maximum reflectivity at a wavelength exactly equaling that of the Bragg wavelength, which is consistent with the energy and momentum conservation model described earlier.

2.3.2 Strain and Temperature Response of Fiber Bragg Gratings

The Bragg grating resonance depends on the effective index of the fundamental mode and the periodicity of the grating. The effective refractive index as well as the grating spacing will be affected by changes in strain and temperature. From (2.41), the shift in the Bragg center wavelength due to strain and temperature changes is given by

$$\Delta\lambda_B = 2\left(\Lambda\frac{\partial n_{eff}}{\partial l} + n_{eff}\frac{\partial\Lambda}{\partial l}\right)\Delta l + 2\left(\Lambda\frac{\partial n_{eff}}{\partial T} + n_{eff}\frac{\partial\Lambda}{\partial T}\right)\Delta T \tag{2.49}$$

The first term in (2.49) represents the strain effect on a fiber Bragg grating. This corresponds to a change in the grating spacing and the strain-optic induced change in the refractive index. The second term in (2.49) represents the effect of temperature on a fiber Bragg grating. A shift in the Bragg wavelength due to thermal expansion changes the grating spacing and the thermo-optic induced change in the refractive index. The above parameters are very important in sensing applications involving fiber Bragg gratings because if the desired sensing parameter is neither strain nor temperature, it is essential to be able to differentiate the effect of strain and temperature from the gathered optical

spectra.

2.3.3 Cladding and Radiation Mode Coupling

Bragg gratings written in a highly photosensitive fiber, or in fiber that has been hydrogenated, have a very pronounced transmission structure (Figure 2.8(a)) on the short wavelength side of the Bragg peak [33]. This feature is only observable in the transmission spectrum (only the main Bragg peak appears when viewed in reflection); therefore, this structure must result from energy loss from light leaving the side of the fiber. To analyze this, one must take into account radiation mode coupling. Usually radiation mode coupling is a smooth function of wavelength; however, the transmission spectrum (Figure 2.8(b)) of the Bragg grating consists of multiple sharp peaks that modulate this coupling, which is a direct consequence of the cylindrical cladding-air interface. Dipping the cladding into a liquid whose refractive index matches that of the cladding, such as glycerin, to effectively eliminate the cladding-air interface, eliminates this effect.

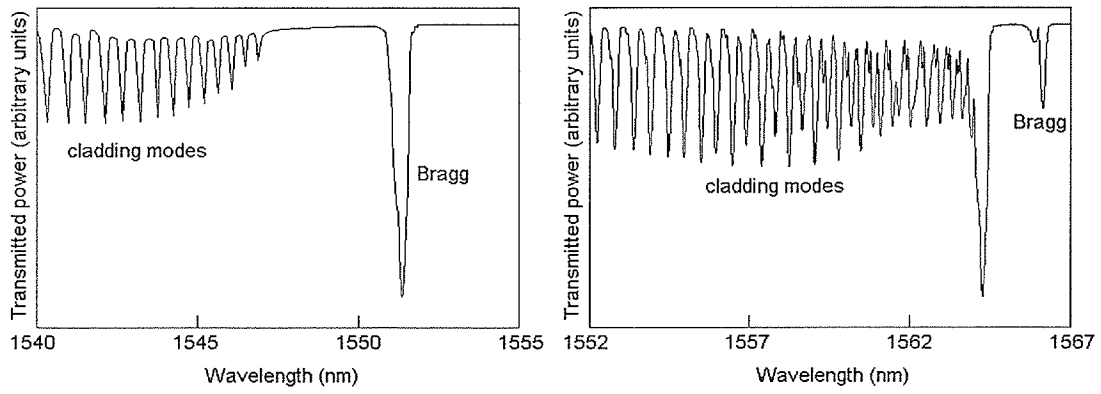

Figure 2.8 a) Schematic transmission profile of a strong fiber Bragg grating, showing loss to radiation modes on the short wavelength side, sharply modified by the cladding mode structure (*After*: [33]); b) Transmission spectrum of a blazed (tilted) fiber Bragg grating (4° tilt), showing pronounced coupling into the asymmetric backward-propagating cladding modes.

The cladding mode coupling can also be described by coupled-mode theory. Limiting the argument to uniform (i.e. no chirp, no tilting) gratings, the only nonzero coupling coefficients between the core and cladding modes involve cladding modes having azimuthal order $l = 1$. Using the salient equations as described in [34], which take in to account the coupling of the core mode to itself and with both counter- and co-propagating $l = 1$ cladding modes (i.e. with the exact cladding modes of order 1μ), one finds

$$\frac{dA^{co}}{dz} = i\zeta_{01-01}^{co-co}A^{co} + i\frac{s}{2}\zeta_{01-01}^{co-co}B^{co}\exp\left(-2i\delta_{01-01}^{co-co}z\right) + i\sum_{\mu}\kappa_{1\mu-01}^{cl-co}B_{\mu}^{cl}\exp\left(-2i\delta_{1\mu-01}^{cl-co}z\right) \tag{2.50}$$

$$\frac{dB^{co}}{dz} = -i\zeta_{01-01}^{co-co}B^{co} - i\frac{s}{2}\zeta_{01-01}^{co-co}A^{co}\exp\left(2i\delta_{01-01}^{co-co}z\right) \tag{2.51}$$

where A^{co} and B^{co} are the amplitudes of the core mode, and B_{μ}^{cl} is the amplitude for the μth cladding mode. The corresponding detuning parameters are given by

$$\delta_{01-01}^{co-co} \equiv \frac{1}{2}\left(2\beta_{01}^{co} - \frac{2\pi}{\Lambda}\right) \tag{2.52}$$

$$\delta_{1\mu-01}^{cl-co} \equiv \frac{1}{2}\left(2\beta_{01}^{co} + \beta_{1\mu}^{cl} - \frac{2\pi}{\Lambda}\right) \tag{2.53}$$

The radiation mode coupling can be analyzed using the coupled-mode theory as well. Sipe and co-workers [29, 35] have studied radiation-mode coupling as a loss mechanism on core mode transmission. The coupled-mode equations in radiation mode coupling becomes [36]

$$\frac{dA}{dz} = i\zeta_{01-01}^{co-co}A + i\sum_{j}\int\kappa_{j\rho-01}^{ra-co}B_{j\rho}\exp\left(-2i\delta_{j\rho-01}^{ra-co}z\right)d\rho \tag{2.54}$$

$$\frac{dB}{dz} = -i\kappa_{01-j\rho}^{co-ra}A\exp\left(2i\delta_{j\rho-01}^{ra-co}z\right) \tag{2.55}$$

with the detuning parameter

$$\delta_{j\rho-01}^{ra-co} \equiv \frac{1}{2}\left(\beta_{01} + \beta_{j\rho} - \frac{2\pi}{\Lambda}\right) \tag{2.56}$$

where A is the amplitude of the core mode and $B_{j\rho}$ is the amplitude of the continuous spectrum of radiation modes. Additionally, δ_{01-01}^{co-co} is the LP_{01} mode self-coupling coefficient and $\kappa_{01-j\rho}^{co-ra} = \left(\kappa_{j\rho-01}^{ra-co}\right)^*$ is the cross-coupling coefficient. The above equations can be used to show that the core mode amplitude approximately obeys an equation of the form [36]:

$$\frac{dA}{dz} = i\zeta_{01-01}^{co-co} A - \left[\sum_j \frac{\pi\beta_{j\rho}}{\rho}\left|\kappa_{j\rho-01}^{ra-co}\right|^2\right] A \tag{2.57}$$

where the term in the square bracket is evaluated at $\beta_{j\rho} = 2\pi/\Lambda - \beta_{01}$. This real term gives rise to exponential loss in the amplitude of the core mode. Furthermore, the loss coefficient is proportional to the square of the cross-coupling coefficient and therefore to the square of the induced index change. This simplified analysis can nevertheless be used to predict the radiation-mode coupling loss spectrum, even when the grating is tilted. As the tilt angle is increased, many radiation mode azimuthal orders must be included in the summation to accurately model radiation modes propagating more normal to the fiber axis. Cladding and radiation mode coupling is essential to understanding the experimental analysis in this thesis.

2.4 Tilted (Blazed) Fiber Bragg Gratings

Tilting the Bragg grating planes at angles to the fiber axis (Figure 2.9), will result in light that is otherwise guided in the fiber core being coupled into loosely bound,

guided-cladding or radiation modes. The tilt of the grating planes and strength of the index modulation determines the coupling efficiency and bandwidth of the light that is tapped out. In a single mode fiber, the tilt of the grating planes enhances the coupling of the light from the forward propagating core mode to backward propagating cladding modes, and reduces the coupling to the backward core mode [12, 34]. Therefore, in the transmission spectrum, both a core mode resonance (satisfying the Bragg condition) and several cladding mode resonances appear (Figure 2.10). A cladding mode is a mode that is confined to the cladding of an optical fiber by virtue of the fact that the cladding has a higher refractive index than the surrounding medium, which is either air or the primary polymer overcoat. Modern fibers have polymer overcoat whose refractive index is slightly higher than that of the cladding, so that light propagating in the cladding is rapidly attenuated and eliminated.

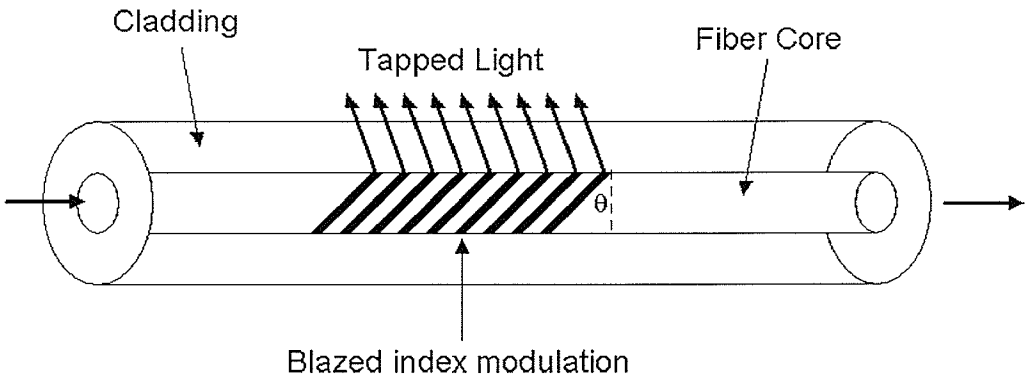

Figure 2.9 A schematic diagram of a tilted (blazed) fiber Bragg grating.

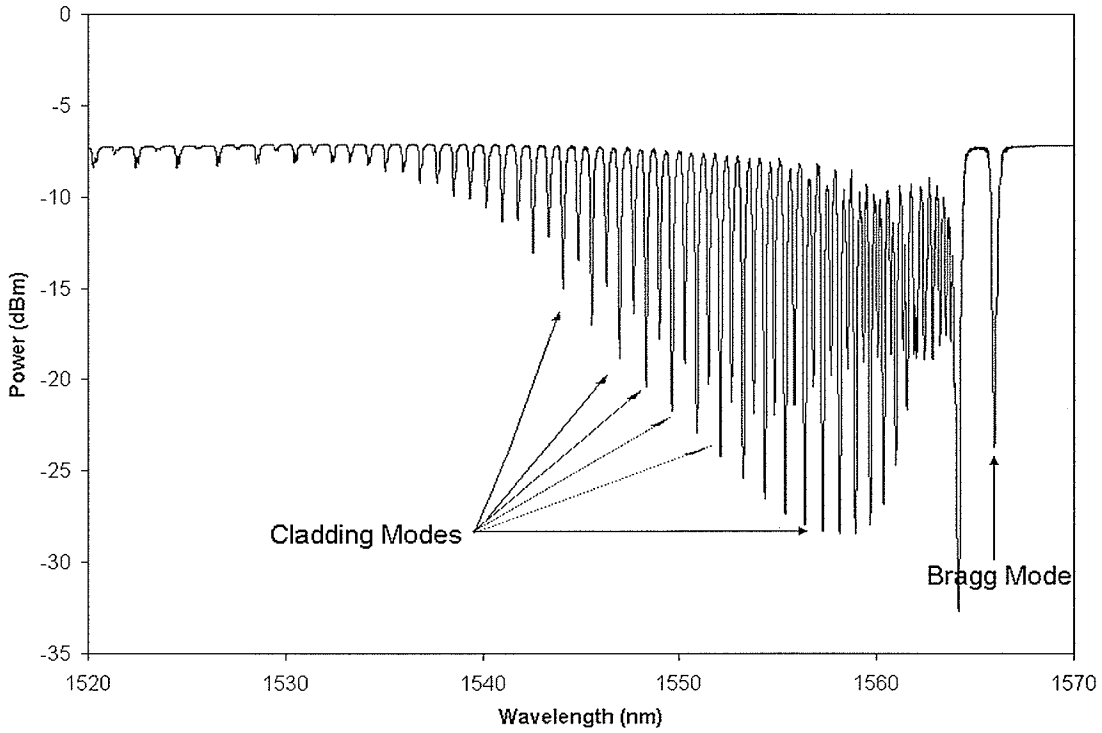

Figure 2.10 Transmission spectrum of a fiber Bragg grating with a 4° tilt angle.

2.5 Refractive Index Sensing via Fiber Bragg Gratings

From the Bragg condition (2.41) it is evident that changes to the Bragg grating spacing or the effective index of the core mode affect the center wavelength that will be reflected. As mentioned before, changes in strain and/or temperature result in changes in the Bragg wavelength; hence, by monitoring shifts in the Bragg wavelength and compare that to the designed Bragg wavelength one gathers the information regarding changes in the temperature and strain. Changes in the effective index of the guided core mode are negligible in uniform (non-tilted) Bragg gratings written in standard single mode optical fibers since the outer cladding is much thicker compared to the core and effectively 'shields' the core mode from any refractive index changes in the surrounding environment. Therefore, to be able to detect changes in the refractive index of the

surrounding environment, there needs to be modifications to the optical fiber geometry or the Bragg grating design to allow the guided core mode to 'see' the refractive index change.

2.5.1 Side-polished Fiber Bragg Gratings

Besides the influences of temperature and strain on the Bragg wavelength of a FBG, the effective refractive index of the guided core mode can respond also to changes in the refractive index of the material within the evanescent field region. This effect has been demonstrated in previous reports using uniformly etched fiber [9]. However, since the evanescent field region of a single mode optical fiber is only a few microns, the uniformly etched fiber method results in an optical fiber whose overall diameter is approximately 10 to 15 microns, thus having a low mechanical stability. Applying the so-called polished fiber half-coupler technology to the fiber segment containing fiber Bragg gratings results in mechanically more stable fiber optic structure with the possibility of exposing an evanescent field of the FBG to the analyte (Figure 2.11).

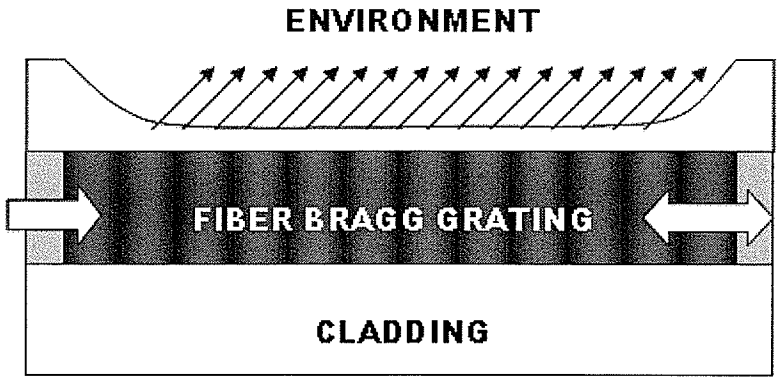

Figure 2.11 A schematic diagram of a side-polished fiber Bragg grating.

The properties of the sensor are determined by the Bragg wavelength λ_B or rather by its shift $\Delta\lambda_B$ as a function of the refractive index of the external medium, n_{ext}. The shift $\Delta\lambda_B$ is assumed to be linearly related to changes Δn_{eff} of the effective refractive index n_{eff} of the guided fiber core mode:

$$\frac{\Delta\lambda_B}{\lambda_B} = \frac{\Delta n_{eff}}{n_{eff}} \tag{2.58}$$

The relations $\lambda_B(n_A)$ and $n_{eff}(n_A)$, respectively, are the characteristics of the refractive index sensor. Because of the asymmetrical removal of the fiber cladding, the characteristics of the sensor depend on the polarization of light (see section 2.1.2). The effective depth of the sensor in a fluid is determined by the penetration depth of the evanescent field. That is, the sensing analyte (the surrounding medium) should cover a depth region that is more than the penetration depth of the evanescent field; otherwise the efficiency of the refractive index sensor decreases [37].

Note that from the evanescent field skin-depth equation (2.35), the penetration depth is fixed according to the wavelength of light being used. Thus, to allow the evanescent field to extend deeper into the analyte or surrounding medium, one can decrease the residual cladding thickness. Intuitively, by reducing the residual cladding thickness, the refractive index sensitivity increases, as will be evident in Chapter 3. It is essential for this type of refractive index sensor to keep the temperature and strain constant so that the wavelength shifts come directly from the result of refractive index change. Another method is to write a reference fiber Bragg grating, at a different design wavelength, in the non-polished segment such that the temperature and strain effect will be eliminated by taking the relative wavelength difference between the two FBGs.

2.5.2 Tilted Fiber Bragg Gratings for Refractive Index Sensing

As mentioned previously that tilted (or blazed) fiber Bragg gratings enhance coupling between the guided core mode and the loosely bound, guided-cladding modes and radiation modes. The cladding mode resonances appear at discrete wavelengths shorter than the core mode Bragg resonance, and they have the same linewidth (determined by the number of grating periods) as the Bragg resonance. The cladding modes are guided by the cladding boundary and as a result their effective index depends on the refractive index of the outer medium. The sensitivity of the cladding mode effective index to changes in the external index increases with mode order since the penetration depth of the evanescent field increases for higher order modes. By monitoring the shifts of the cladding modes relative to the Bragg resonance, an accurate measure of the surrounding refractive index can be obtained.

Recall the Bragg condition for a uniform fiber Bragg grating, the Bragg wavelength is defined by $\lambda_B = 2n_{eff}\Lambda$. In a tilted Bragg grating, Λ is the projection of the actual grating period Λ_g along the fiber axis due to the tilt angle θ:

$$\Lambda = \Lambda_g/\cos\theta \tag{2.59}$$

Similarly, cladding mode resonances can be found through [12]:

$$\lambda_C(i) = (n_{eff}(i) + n_C(i))\,\Lambda \tag{2.60}$$

where $n_{eff}(i)$ is the effective index of the core mode at the wavelength of i^{th} cladding mode resonance, and $n_C(i)$ the cladding mode effective index *at the same wavelength.* Now if one considers the wavelength separation between the Bragg resonance and one of the cladding mode resonances one can estimate the sensitivity of this parameter to

various perturbations. In the case of changes of the external medium refractive index n_{ext}, the differential shift (change in wavelength separation) is due entirely to the dispersion of the cladding mode effective index, multiplied by the grating period:

$$\Delta (\lambda_B - \lambda_C(i)) / \Delta n_{ext} = -\Lambda \ \partial n_C(i)/\partial n_{ext} \tag{2.61}$$

The temperature dependence of the relative wavelength shift of the Bragg resonance and cladding mode resonances can also be obtained by differentiating (2.41) and (2.61) respectively:

$$\Delta\lambda_B/\Delta T = 2 (\Lambda \partial n_{eff}/\partial T + n_{eff} \partial\Lambda/\partial T) \tag{2.62}$$

$$\Delta\lambda_C(i)/\Delta T = \Lambda(\partial n_{eff}(i)/\partial T + \partial n_C(i)/\partial T) + (n_{eff}(i)+n_C(i))\partial\Lambda/\partial T \tag{2.63}$$

Since most fibers (and certainly the fibers used in this research) have a very small composition difference between the core and cladding glass, the thermo-optic coefficients ($\partial n/\partial T$) for the refractive index of the core and cladding are similar and close to the value for pure silica, approximately 11×10^{-6}/°C [38]. Under these conditions, and for typical grating periods near 500 nm (to get Bragg and cladding mode resonances in the 1500-1600 nm wavelength region) the first terms on the right hand side of (2.62) and (2.63) will add up to a worst case value near:

$$\Lambda(2\partial n_{eff}/\partial T - \partial n_{eff}(i)/\partial T - \partial n_C(i)/\partial T)/°C < \Lambda\times10^{-5} = 5 \text{ pm }/°C \tag{2.64}$$

Furthermore, the coefficient of thermal expansion of silica (0.55×10^{-6}/°C) [38] can be used *in lieu* of $(1/\Lambda)\partial\Lambda/\partial T$ to get the relative shift in the resonances due to thermal expansion (from the second terms on the right hand side of (2.62) and (2.63)):

$$\Lambda * 0.55\times10^{-6} (2n_{eff} - n_{eff}(i) - n_C(i))/°C < 0.12 \text{ pm/°C} \tag{2.65}$$

by virtue of the fact that both n_{eff} and $n_{eff}(i)$ lie between 1.446 and 1.448 over the

wavelength range of interest (1500-1600 nm) and that $n_C(i)$ can be as low as n_{ext}. For the worst case estimate given above, the following values were taken: n_{eff}=1.446, $n_{eff}(i)$=1.448, and $n_C(i)$=1.0 ($n_{eff}(i)$ is always larger than n_{eff} because of dispersion). As a result, using the distance between the Bragg resonance and one of the cladding mode resonance to measure the surrounding refractive index, the measurement of $\Delta(\lambda_B - \lambda_C(i))$ will have a cross-sensitivity to temperature of the order of a few pm/°C. Another parameter which could adversely affect the resolution of the surrounding refractive index measurements is strain on the fiber. However, in refractometry applications it is conceivable that the fiber in which the grating is written can be packaged in such a way that minimal strains occur during the measurements.

Chapter 3

Simulation

3.1 Introduction

The first task is to determine the theoretical response of the side-polished and tilted fiber Bragg gratings to changes in the external refractive index. Two different software packages were employed to perform simulations on the two fiber Bragg grating designs: FEMLAB from Comsol Group and Opti*Grating* from Optiwave Systems Inc. The first software used, FEMLAB, is a finite-element based simulation software and it has a built-in optics library including optical fibers. Using the model available in the library, with modifications to the fiber geometry to represent the side-polished fiber structure, effects of varying the external refractive index were recorded. On the other hand, spectral responses of the tilted fiber Bragg grating were simulated with Opti*Grating*. Opti*Grating* uses the Coupled-Mode Theory to model the light and enables analysis and synthesis of gratings. From these results, expected responses can be compared with experimental results later obtained.

3.2 Simulation Geometry

Simulations were performed using step-index fiber profile, meaning that the optical fiber core has a uniform refractive index distribution whose value is slightly higher than that of the cladding material, which also has a uniform refractive index distribution. The side-polished fiber structure was simulated as a small circle in the

middle (the core) and a much larger circle with a straight edge boundary slicing across the larger circle with its nearest edge located at some distance away from the edge of the core, simulating the residual cladding thickness of the side-polished fiber structure. The optical fibers used for this research were Corning SMF28® fibers whose core and cladding parameters were specified as: core radius = 4.15 μm, cladding radius 62.5 μm, n_{core} = 1.4507, and n_{clad} = 1.444025 at 1550 nm. The top half of the cladding was replaced by an external surrounding medium whose refractive index varied, and its geometry was setup to complete the circular structure before half of the cladding was removed (see Figure 3.1 for simulation geometry). This was done to reduce the complexity of the meshing in the finite-element analysis and to avoid any discontinuities across the boundaries. This simplification would have no effect on the optical field distribution simulated by the software since the most important optical interactions occur only in the core and the regions immediately surrounding it.

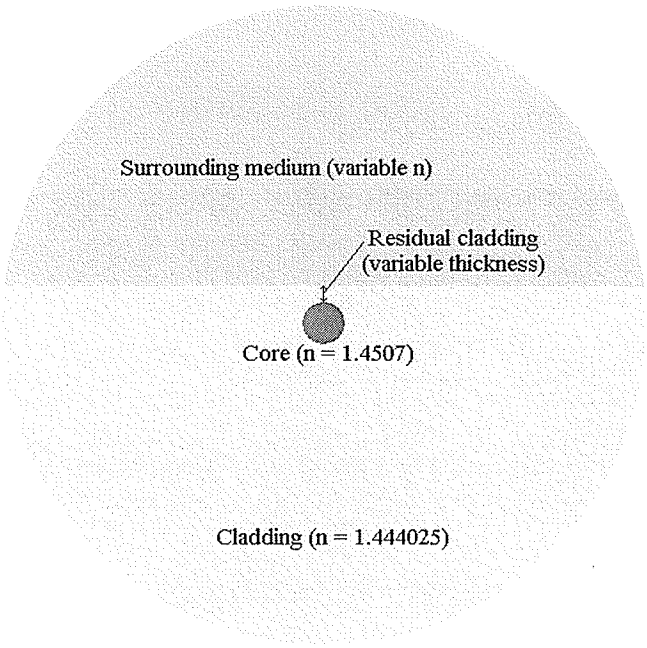

Figure 3.1 Side-polished fiber simulation geometry (cross-sectional view).

In contrast, tilted fiber Bragg gratings required no modifications to its geometry. However, its complex spectral response involving cladding and radiation modes in the transmission mode made it impossible to use a simple software package like FEMLAB. Instead, a more complex but powerful software, Opti*Grating*, was used to simulate their spectral response to varying external refractive index. As was the case in the side-polished fiber Bragg gratings, the core radius for the tilted grating was specified at 4.15 μm, and the cladding radius was specified at 62.5 μm. The external medium was setup surrounding the fiber cladding having a thickness of 50 μm with its refractive index variable. A depiction of the tilted fiber Bragg grating simulation structure is shown in Figure 3.2.

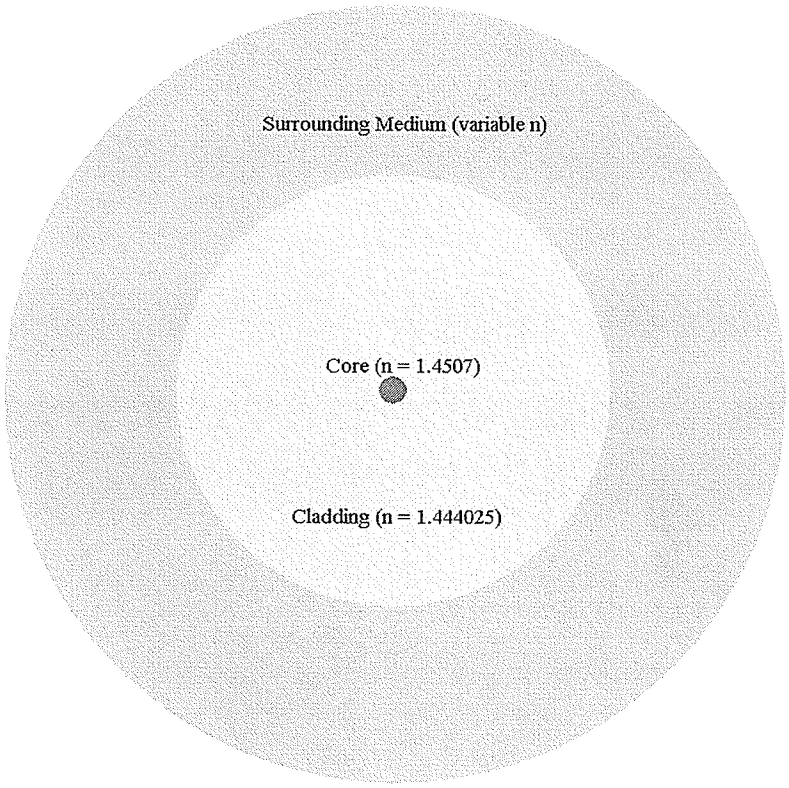

Figure 3.2a Tilted grating simulation geometry (cross-sectional view).

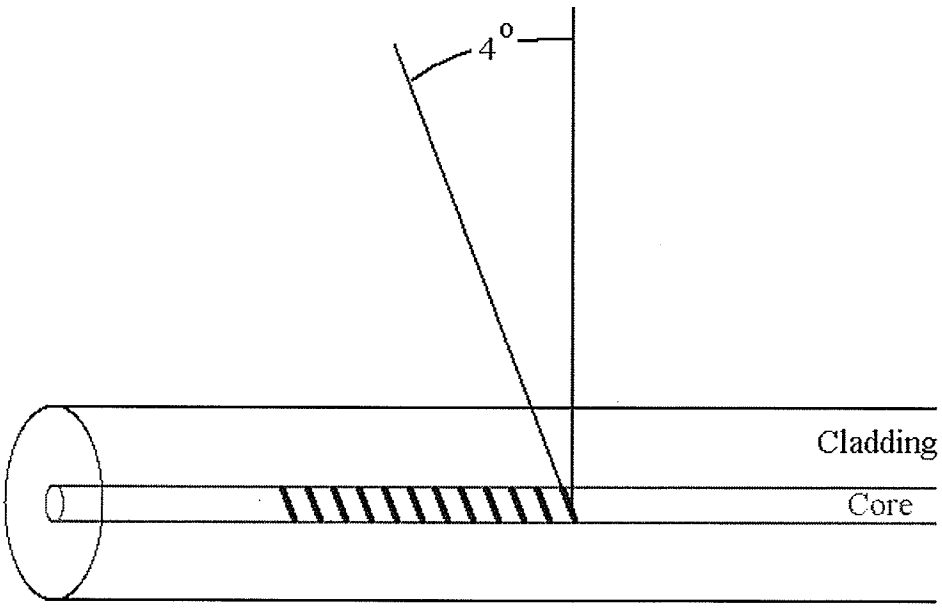

Figure 3.2b Grating planes tilted at 4° with respect to the normal to the fiber axis.

3.3 Basic Simulation

3.3.1 The Finite-Element Method

The finite-element simulation is a simple tool that provides quick snapshot one can expect in an actual experiment, such as the optical field and power distribution, the possible modes that exist, the effective index, etc. Recall that the Bragg grating equation states that the Bragg wavelength depends on the grating pitch and the effective index of the guided mode, i.e. $\lambda_B = 2n_{eff}\Lambda$. The point of interest here is how changes in the external refractive index influence the effective index of the guided mode. This finite-element method was used to simulate the side-polished fiber Bragg gratings because their response, either in reflection or transmission mode, depends only on the change of the effective index and the grating pitch. The grating pitch was assumed to be constant as

strain and temperature were kept constant in the experiments that were carried out, preventing any physical elongation or thermal expansion of the grating. The external medium was only microns away from the core of the optical fiber (Figure 3.1), allowing the evanescent field interactions to take place and FEMLAB calculates the effective index as a result of this interaction.

It is important to specify the number of modes and the approximate mode index that FEMLAB should solve for as incorrect parameters would yield physically meaningless results. The number of modes was specified at two (single-mode optical fiber) and FEMLAB solved for modes whose index were near that of the cladding material as these modes were the only physically meaningful modes. The effective index values were recorded and used to calculate the Bragg wavelengths as a result of varying the refractive index of the external medium. The wavelength results were recorded along with the values of the external refractive index (see Figure 3.3 for example).

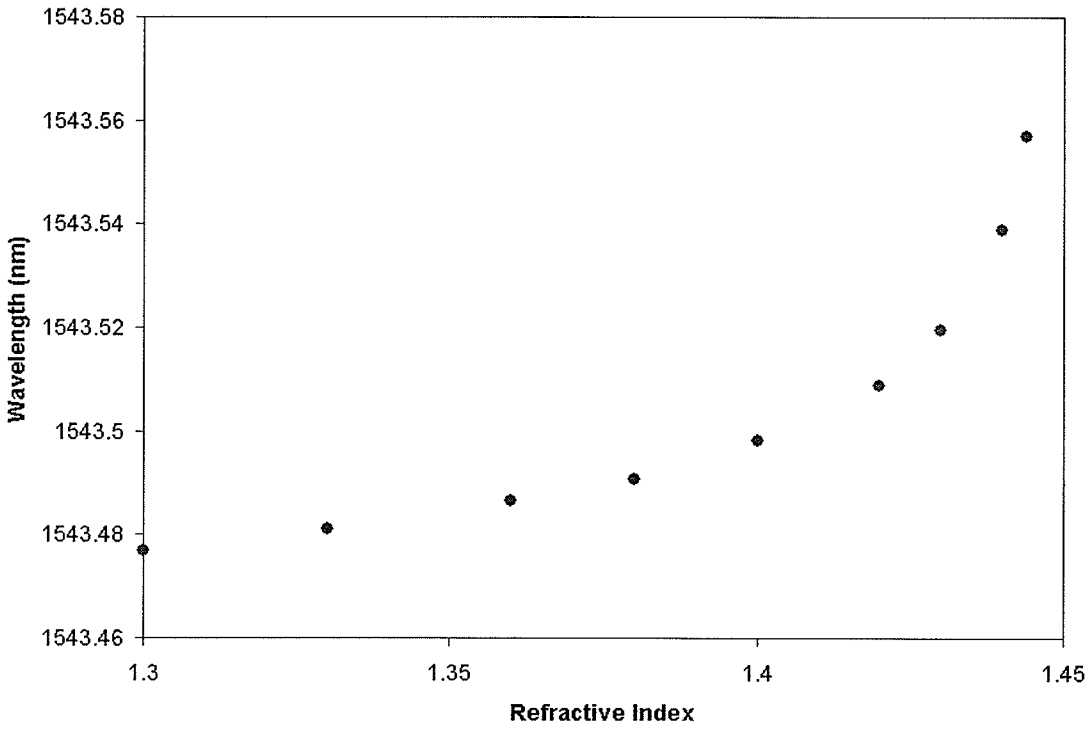

Figure 3.3 Bragg wavelength positions versus surrounding refractive index values.

3.3.2 Opti*Grating*

As previously described, tilted fiber Bragg gratings involve modes other than the guided mode, thus making finite-element method insufficient for providing an understanding of the expected grating behaviour. OptiGrating provides a complete and accurate understanding of the tilted grating behaviours because it uses the Coupled-Mode Theory to model light scattering and interaction, including the cladding modes and continuum of radiation modes. The simulation structure is shown in Figure 3.2 and the Bragg grating had the following parameters: length = 10 mm, center wavelength = 1566 nm, and internal tilt angle = 4°. The refractive index of the surrounding medium was varied and the simulated transmission spectral response of the tilted grating was analyzed. Recall in Chapter 2 that the absolute locations of the different modes are not

important, only the relative distance between the core (Bragg) mode and the individual cladding modes because shifts in the relative distances are directly related to external refractive index changes. Relative distances between the core (Bragg) mode and select cladding modes (see Figure 3.4) were recorded and listed in Table 3.1 and plotted with curve fitting ($R^2 = 0.9999$) in Figure 3.5. The cladding modes selected are located at 23, 14, and 8 nm away from the Bragg resonance and changes in the relative distances are referenced to n_{ext} = air.

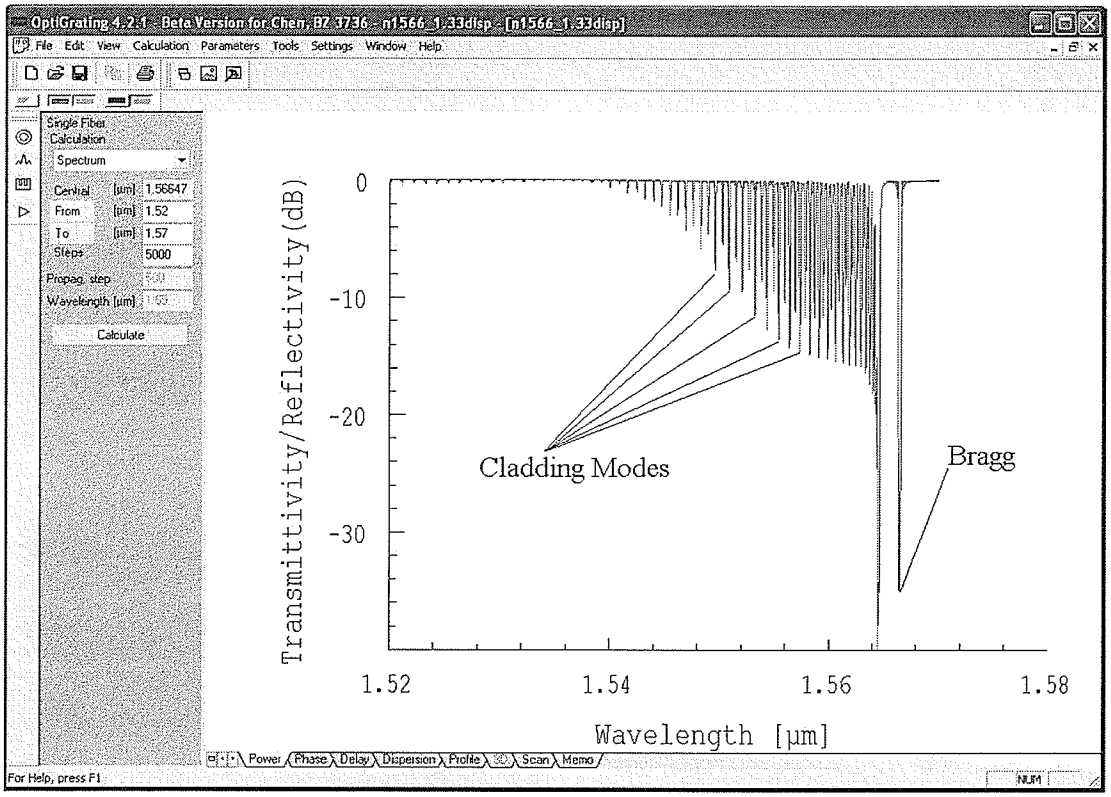

Figure 3.4 Screenshot of an Opti*Grating* simulation plot.

Table 3.1 Relative distances between selected cladding modes and the Bragg resonance at different surrounding refractive index values

Surrounding refractive index	Cladding mode 8 nm away from Bragg	Cladding mode 14 nm away from Bragg	Cladding mode 23 nm away from Bragg
	Shift of relative distance between the cladding modes and the Bragg resonance (pm) with reference to n = 1		
1	0	0	0
1.3	30	57	112
1.33	40	80	147
1.34	45	90	167
1.35	50	97	187
1.36	55	110	207
1.37	60	125	237
1.38	70	143	277
1.39	80	167	327
1.4	95	202	427
1.41	117	257	
1.42	152	380	
1.43	237		

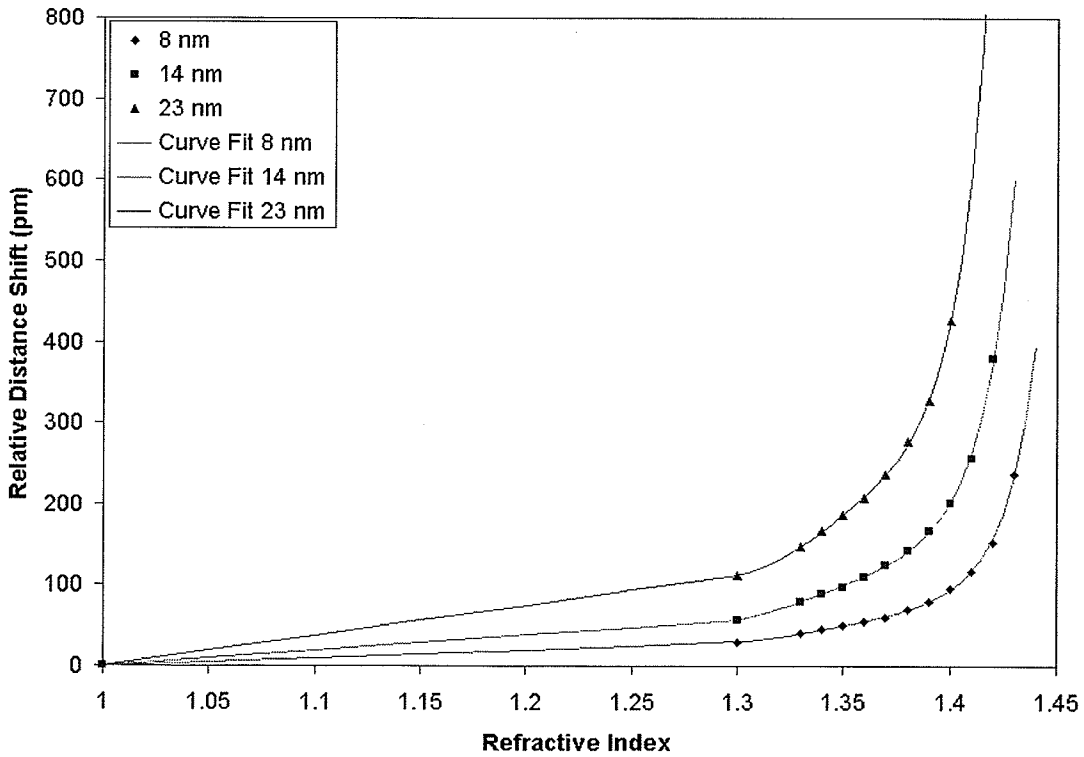

Figure 3.5 Plot of simulation results and fitted curves.

3.4 Parameter Variation

In addition to varying the refractive index of the surrounding medium, the residual cladding thickness was varied to understand its effect on the refractive index sensitivity. Residual cladding thickness values between 0.5 μm and 2 μm were used in the FEMLAB simulation in 0.25 μm increments. The results of varying residual cladding thickness were plotted against the external refractive index (Figure 3.6).

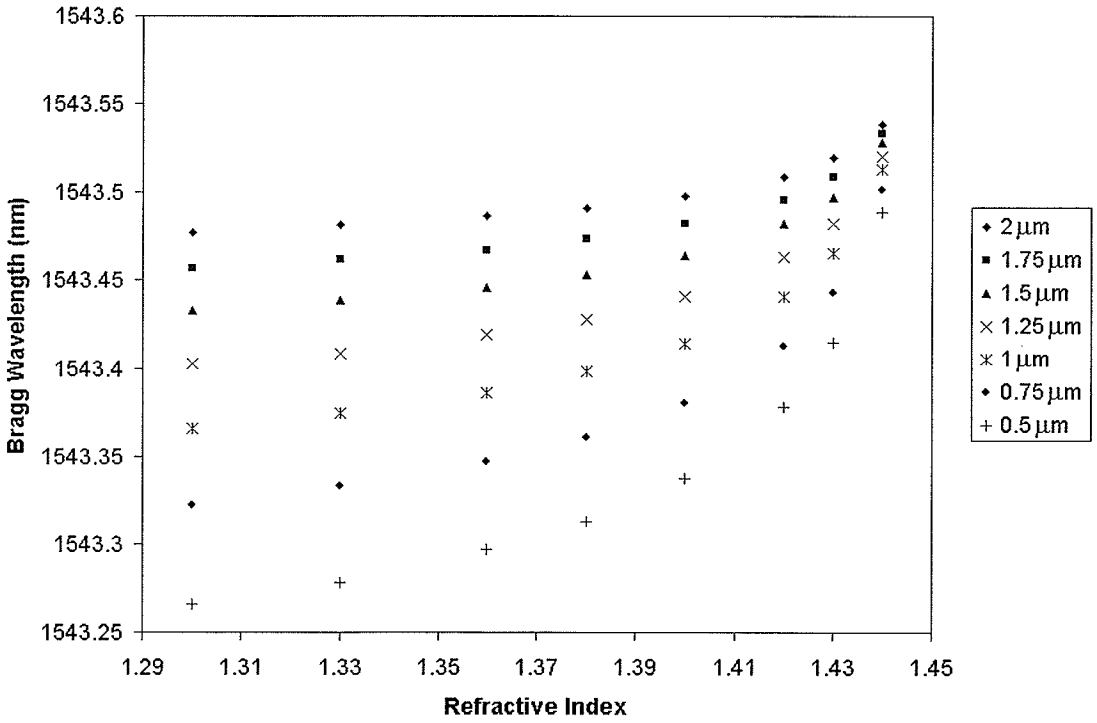

Figure 3.6 Plot of Bragg wavelength versus external refractive index with different residual cladding thickness.

3.5 Results

The results of the simulations provided some very important observations and expectations. In the case of side-polished fiber Bragg gratings, it is evident from the simulation results that reducing the residual cladding thickness increases the refractive

index sensitivity. Moreover, the refractive index sensitivity is much higher when the external refractive index is close to that of the cladding material than when the external medium is air (n = 1.0003) or water (n = 1.333 at 589 nm). Although the simulation does not consider temperature variations, it is very important to keep the temperature constant throughout the experiments for side-polished fiber Bragg gratings as temperature induced shifts of the Bragg wavelength (approximately 10 pm/°C) may distort the testing results.

In contrast, the tilted fiber Bragg gratings eliminate the temperature induced ambiguity since by taking the relative distance between the Bragg resonance and individual cladding modes, only the effects of surrounding refractive index are pronounced. As the simulation results indicate, the maximum refractive index sensitivity can be achieved at different surrounding refractive index values by selecting different cladding modes to perform the analysis. The cut-off value for the surrounding refractive index that can be detected with either the side-polished or tilted fibre-Bragg grating is close to the refractive index of the cladding, which is approximately 1.444 at 1566 nm. Beyond this value, the software packages either could not perform simulations or output physically meaningless results.

Chapter 4

Sensor Design and Fabrication

4.1 Introduction

The simulation results in Chapter 3 provided some of the important design criteria. For the side-polished fiber Bragg grating to be an effective sensor, the residual cladding thickness should be less than 2 μm, with the refractive index sensitivity increasing exponentially for smaller residual cladding thickness. On the other hand, optical power loss becomes a major problem when the residual cladding thickness reaches down to two microns (within the evanescent regime) and may not provide sufficient signal in the reflection or transmission mode. Thus, the optimal residual cladding thickness depends on increasing the sensitivity without losing too much signal in the process. In comparison, the tilted fiber Bragg grating sensor design requires no modifications to the fiber geometry, thus keeping its mechanical strength intact. However, since they must be written at a tilt angle with respect to the fiber axis, the normal procedures for imprinting fiber Bragg gratings must be modified to make it possible. This section examines the design parameters and fabrication techniques.

4.2 Device Structure and Materials

The optical fibers used for fabrication of the side-polished and tilted fiber Bragg grating are Corning SMF28e (single-mode photonic fibers) and Corning SMF28 (single-mode fibers), respectively. These optical fibers are silica based, meaning that the core

and cladding materials are largely silica with germanium doping in the core of the optical fibers to make its refractive index slightly higher than that of the cladding for total internal reflection operation. Side-polished fiber Bragg gratings were fabricated by FiberLogix Ltd. To fabricate these sensors, a uniform grating was first imprinted in a section of the core and then parts of the cladding over the grating were polished off, yielding a D-shaped structure along the length of the grating (Figure 4.1). On the other hand, tilted fiber Bragg gratings were fabricated using an excimer laser source and phase masks at the Photonics Laboratory at Carleton University located in Ottawa, Canada. These gratings were fabricated by imprinting uniform gratings in the core at an angle with respect to the fiber axis. There was no change in the fiber structure for the tilted fiber Bragg gratings. For investigative purposes, this research also employed tilted fiber Bragg gratings written on Corning 80 μm and 50 μm prototypes (still silica based).

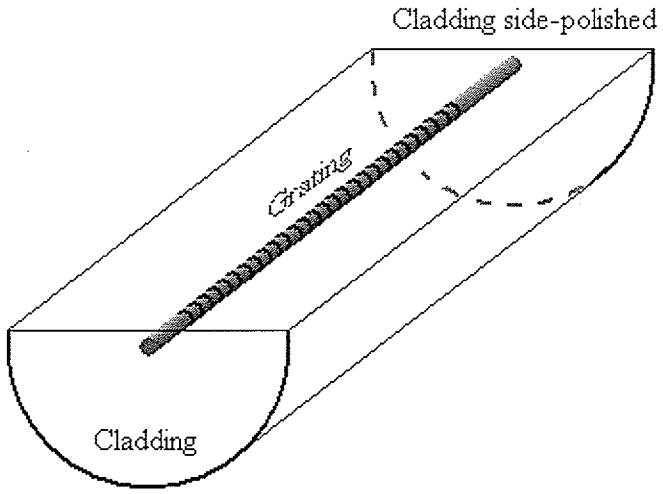

Figure 4.1 A typical side-polished fiber with cladding over the grating partially removed.

4.3 Fabrication

4.3.1 Side-polished Fiber Bragg Grating

The first fiber Bragg grating sensor technology employed in this thesis work was side-polished fiber Bragg grating. The fabrication process for this type of Bragg grating was the same as normal uniform fiber Bragg grating in terms of the grating imprinting. The grating sensors were manufactured by FiberLogix Ltd using Corning SMF28e fibers, having a standard single-mode fiber core diameter of 8.3 μm and cladding diameter of 125 μm. The fibers were photosensitive, allowing the ultraviolet light to induce a structural and compositional change in the core with the pattern transferred from the phase mask (Figure 4.2) and the gratings were written. Once the gratings were written, the optical fibers were mounted and side-polished along the grating section on a circular wheel 1 mm in diameter (much larger compared with the fiber diameter). The polishing was done to yield more evanescent field interaction between the surrounding environment and the gratings. Table 4.1 shows the design and grating parameters.

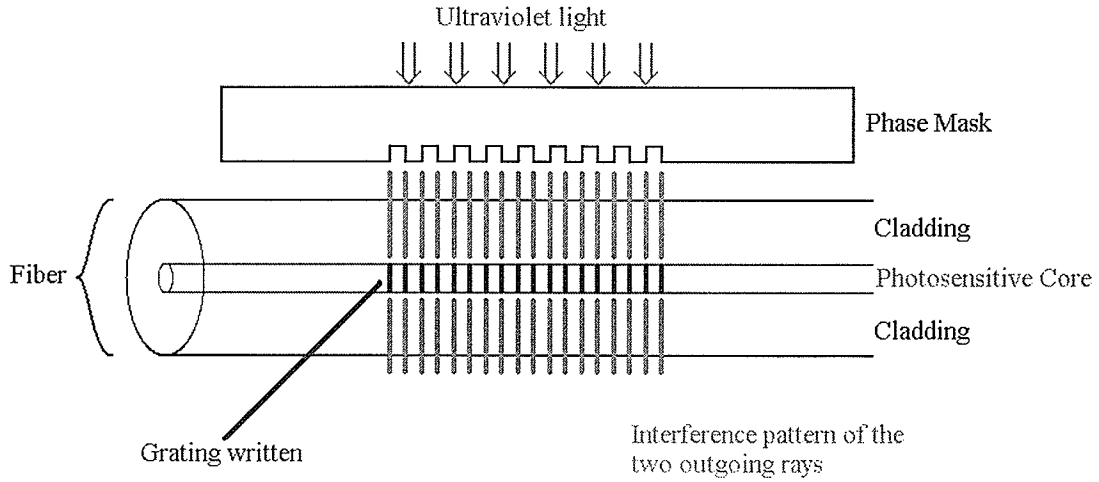

Figure 4.2 A fiber Bragg grating manufactured by exposing the fiber core to UV interference patterns through a phase mask.

Table 4.1 Summary of side-polished fiber design parameters.

Design Parameter	Specification
Optical fiber	Corning SMF28e photonic fiber
Bragg grating center wavelength	1543.7 ± 1 nm
Grating pitch	533.2 nm
Length of grating	22 ± 1 mm
Reflectivity	> 50%
Full-width at half maximum (FWHM)	0.25 ± 0.1 nm
Side bands	≤ -15 dB
Length of side-polishing	≈ 23.5 ± 0.5 mm
Residual cladding thickness	≈ 1 – 2 μm

The manufacturer's process guaranteed all of the above specifications except for residual cladding thickness, which was only estimated to be about 2 μm by the manufacturer. This parameter was very important to this work; therefore, testing was done to decide whether to further reduce the residual cladding thickness. The grating spectra showed a slight change of the Bragg wavelength before and after the side-

polishing (Figure 4.3). This is due to the fact that the grating, after side-polishing the cladding, now interacts with a different surrounding medium (air) compared to before side-polishing.

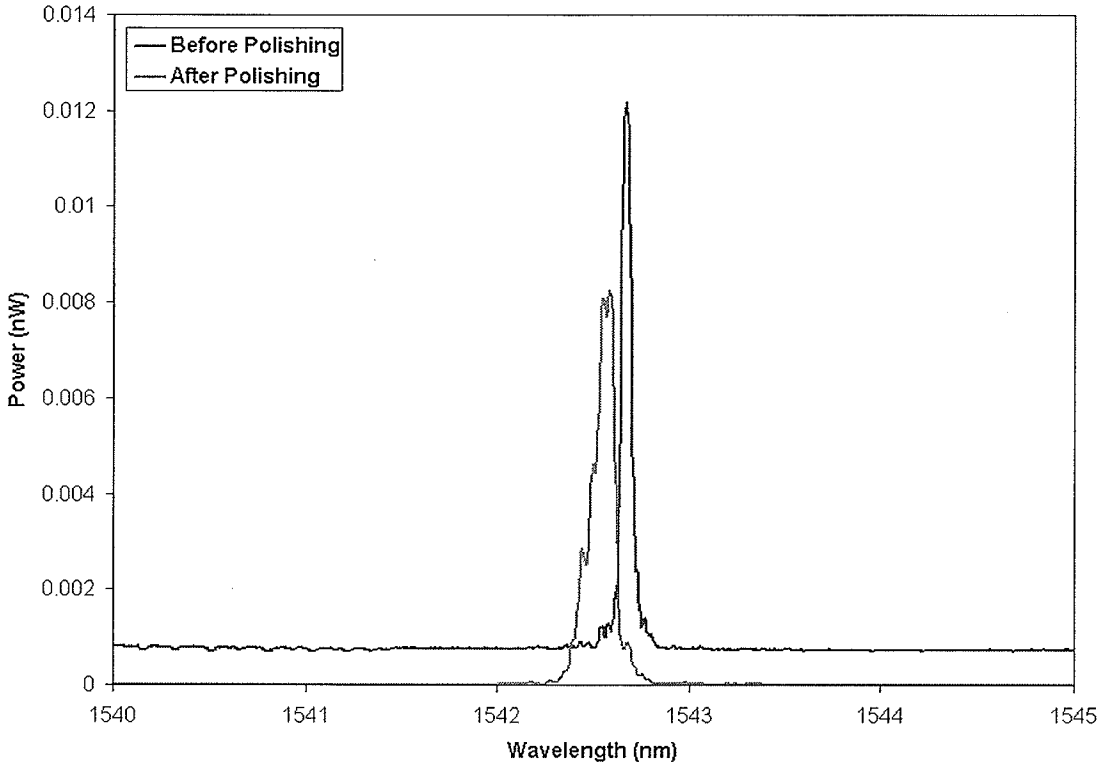

Figure 4.3 Fiber Bragg grating reflection spectrum before and after side-polishing.

4.3.2 Tilted Fiber Bragg Grating

While the side-polished fiber Bragg gratings exploit evanescent field interactions and refractive index sensing by removing parts of the cladding, there exists another method to detect changes in the surrounding refractive index without removing any part of the cladding. Tilted fiber Bragg gratings make use of the cladding modes and the Bragg mode for refractive index sensing and temperature reference. The tilted fiber Bragg gratings for this research were fabricated using hydrogen-loaded (hydrogenated)

Corning SMF28 fibers [37]. The hydrogenation was done to make the optical fiber core sensitive to ultraviolet light source used to imprint the gratings, much the same principle behind photosensitive fibers.

Tilted fiber Bragg gratings were imprinted through the use of phase masks and a pulsed KrF excimer laser source [38]. The grating planes were tilted at 4° with respect to the normal to the fiber axis (Figure 4.4). This angle is the internal tilt angle and it is not the same as the angle that the fibers were tilted with respect to the laser source since the refractive indices of the core, cladding, and air are different. The equation used to determine the angle at which the fiber was to be tilted against the laser source and the internal (core) tilt angle is

$$\theta_{air} = \sin^{-1}\left(\frac{n_{core}\sin\theta_{core}}{n_{air}}\right) \tag{4.1}$$

The internal tilt angle used in this research was 4°. The grating period for the samples was 536 nm, and the grating length was 10 mm. A summary of the design parameters for the tilted fiber Bragg gratings is presented in Table 4.2.

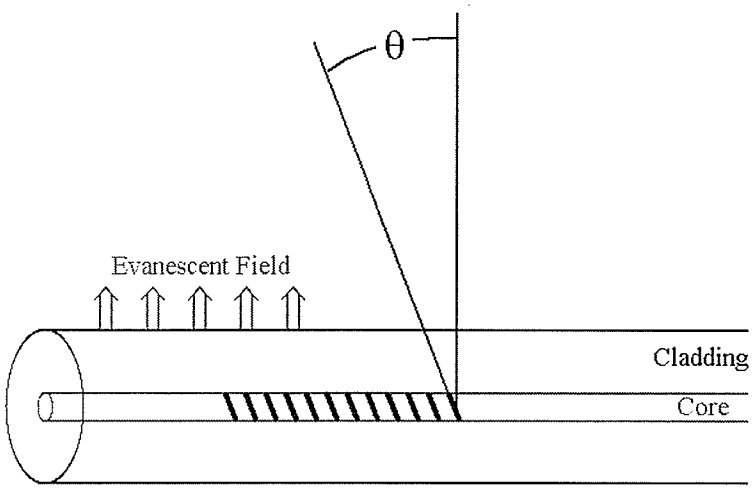

Figure 4.4 A fiber Bragg grating with its grating planes tilted at an angle θ with respect to the fiber axis.

Table 4.2 Summary of tilted fiber Bragg grating design parameters.

Design Parameter	Specification
Optical fiber	Corning SMF28 (hydrogen-loaded)
Bragg grating center wavelength	1566 ± 1 nm
Grating pitch	536 nm
Length of grating	10 ± 1 mm
Linewidth (for individual cladding modes)	< 0.20 nm
Tilt angle	4°
Cladding modes	< -10 dB from reference level

In addition to the batch of samples written at 4° tilt, one sample was written at 6° and some were written at 4° on 80 μm and 50 μm diameter fibers for comparison purposes only. This thesis work places the emphasis on gratings written on standard single-mode fibers.

4.4 Chemical Etching

As previously noted in the side-polished fiber fabrication, the residual cladding thickness was an uncertainty in the production process. While the optical fibers, under microscope, show extensive side-polishing, further testing reveal that its refractive index sensitivity was not as high as expected. The expected wavelength shift was at least 10 pm when the refractive index went from 1 to 1.33 (air to water); however, the observed wavelength shift was negligible. As a result, a chemical etching was done on the side-polished fiber Bragg grating to increase its sensitivity, and the fiber Bragg grating spectrum was monitored in-situ in real-time while the etching was underway (Figure 4.5).

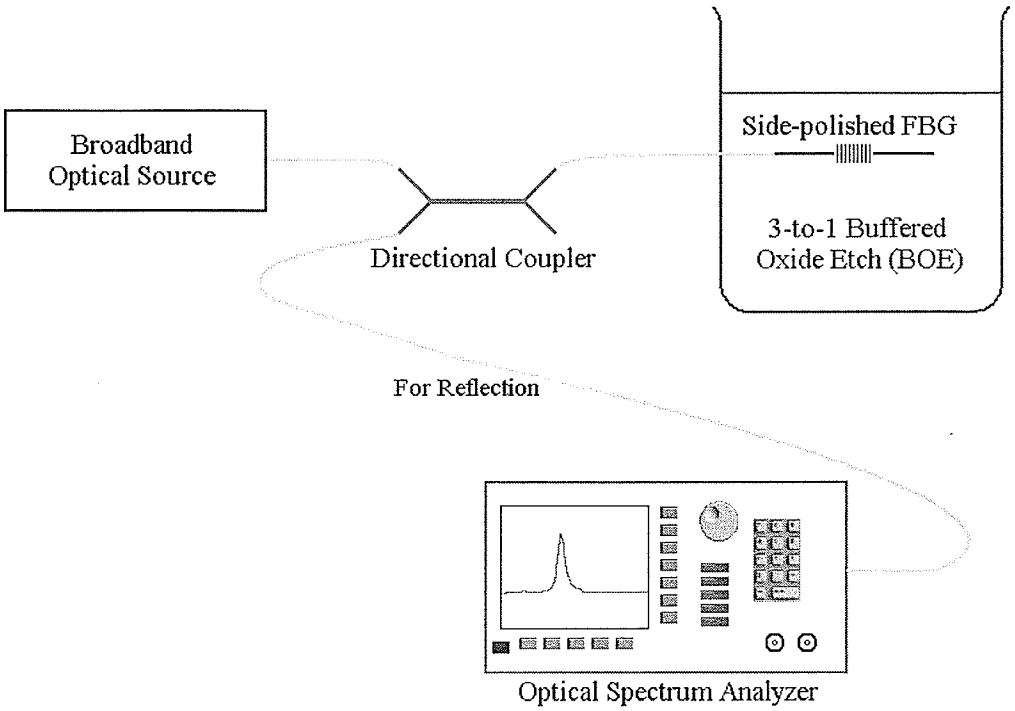

Figure 4.5 Setup for chemical etching on the side-polished fiber Bragg grating sensor with *in-situ* monitoring.

The chemical etching was done using Olin Hunt 10-to-1 buffered oxide etch (BOE) at room temperature, which etches silica materials at an average rate of approximately 0.05 μm/min [39-43]. The chemical etching was performed for 15 minutes and was stopped when the reflected power level had fall to half of that before the etching. After the chemical etching the refractive index sensitivity was enhanced, and a full set of experimental testing was done. The experimental procedures and results for the side-polished fiber Bragg grating and tilted fiber Bragg grating sensors are described in detail in Chapters 5 and 6, respectively.

Chapter 5

Side-polished Fiber Bragg Gratings

5.1 Introduction

This chapter describes the experimental tests that were performed on the side-polished fiber Bragg gratings that included a temperature/humidity characterization and a sucrose solution test to simulate different external refractive indices. A detailed description of the experimental apparatus, including the design of the sensor probe, is also included. This chapter will conclude with a comparison between the simulation and experimental results.

5.2 Characterization Tests

A set of temperature and relative humidity characterization tests were carried out to determine the temperature/humidity dependence of the side-polished fiber Bragg grating sensors. The set of values at which the fiber Bragg grating spectra were recorded is presented in Table 5.1. The side-polished fiber Bragg gratings were taped on a fiber holder (Figure 5.1) and placed inside an environmental chamber that controlled the temperature and humidity to ±0.2 °C and ±0.5%, respectively. Testing temperature started from –40 °C to prevent condensation freezing if the testing temperature started from 80 °C. Relative humidity (RH) values were not set for temperatures below 0 °C because they were meaningless and not controllable. The only RH values recorded for temperatures above 0 °C were the ones that could be well-controlled and maintained

constant throughout the experiment by the environmental chamber. This characterization test served as a general reliability study on the side-polished fiber and provided information on the temperature dependence of the side-polished fiber Bragg grating center wavelength.

Table 5.1 Characterization test conditions.

Testing Conditions					
Temperature (°C)	Relative Humidity (%RH)				
–40	N/A	N/A	N/A	N/A	N/A
–27.5	N/A	N/A	N/A	N/A	N/A
–15	N/A	N/A	N/A	N/A	N/A
–2.5	N/A	N/A	N/A	N/A	N/A
10	N/A	N/A	N/A	N/A	85%
20	N/A	N/A	50%	70%	90%
40	N/A	30%	50%	70%	90%
60	10%	30%	50%	70%	90%
80	10%	30%	50%	70%	90%

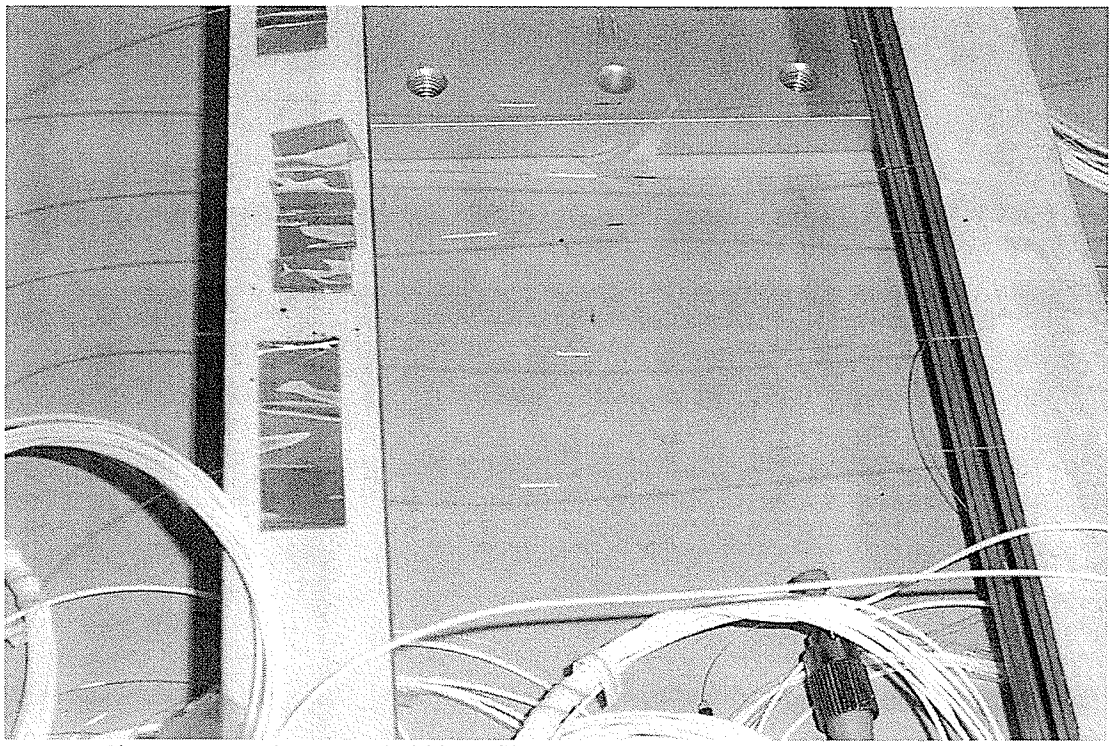

Figure 5.1 FBG sensors held by a fiber holder ready for characterization testing.

The apparatus used in this characterization test included a broadband optical source (functional wavelengths from 1300 – 1600 nm), a directional coupler, an optical spectrum analyzer (9 pm resolution), an environmental chamber, and a computer to record data (see Figure 5.2 for an illustration of the experimental setup). Both the reflection and transmission spectra were recorded during the test, with the Bragg center wavelength determined in the post-experimental data analysis. The side-polished fibers were kept straight and held under constant (albeit minimal) strain to ensure that no strain-induced shifts of the Bragg wavelength occurred. A set of five reflection and transmission spectra were taken at each single testing condition (a ten minute stabilization time was given before the spectra were recorded), with the results averaged. The reflection and transmission spectra showed temperature-induced shifts of the Bragg wavelength to be linear (Figure 5.3), and the Bragg wavelength locations are listed in Table 5.2 with a graphic display of the wavelengths versus temperature in Figure 5.4.

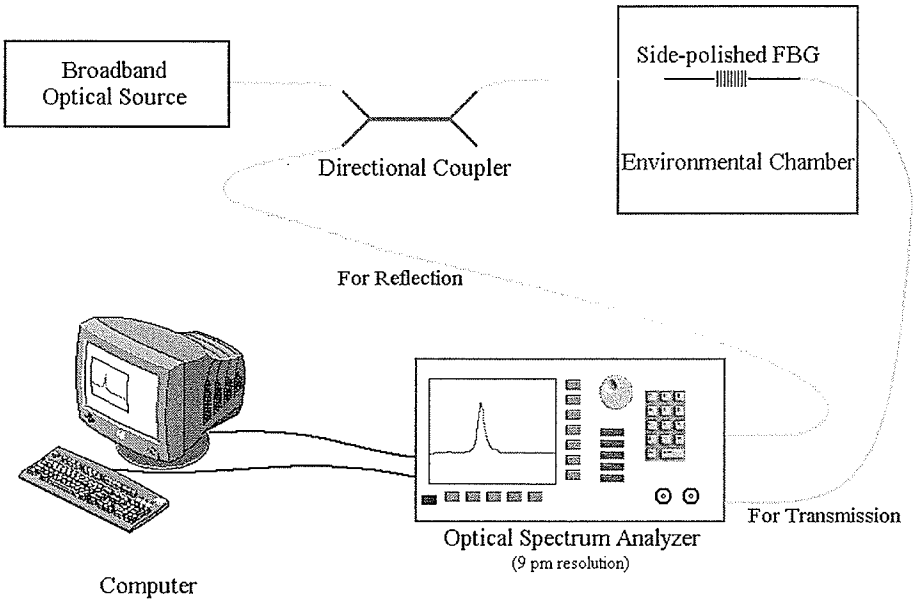

Figure 5.2 Characterization experiment setup for side-polished FBG sensors.

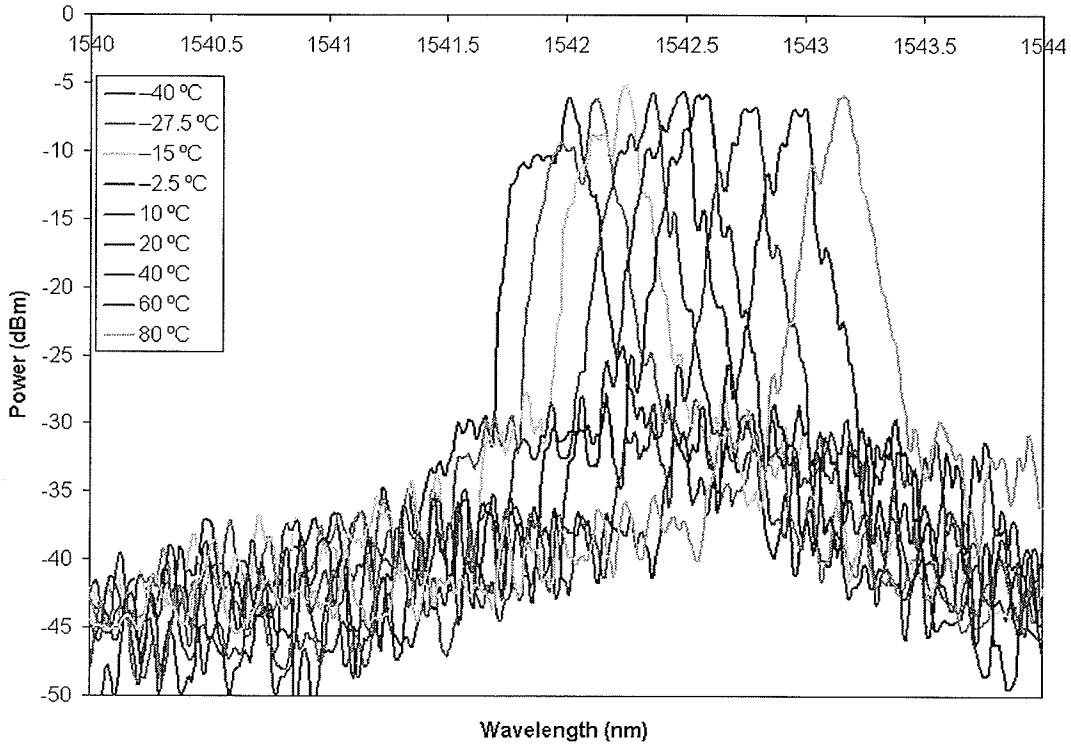

Figure 5.3a Reflection spectra of a side-polished FBG sensor in response to temperature variation.

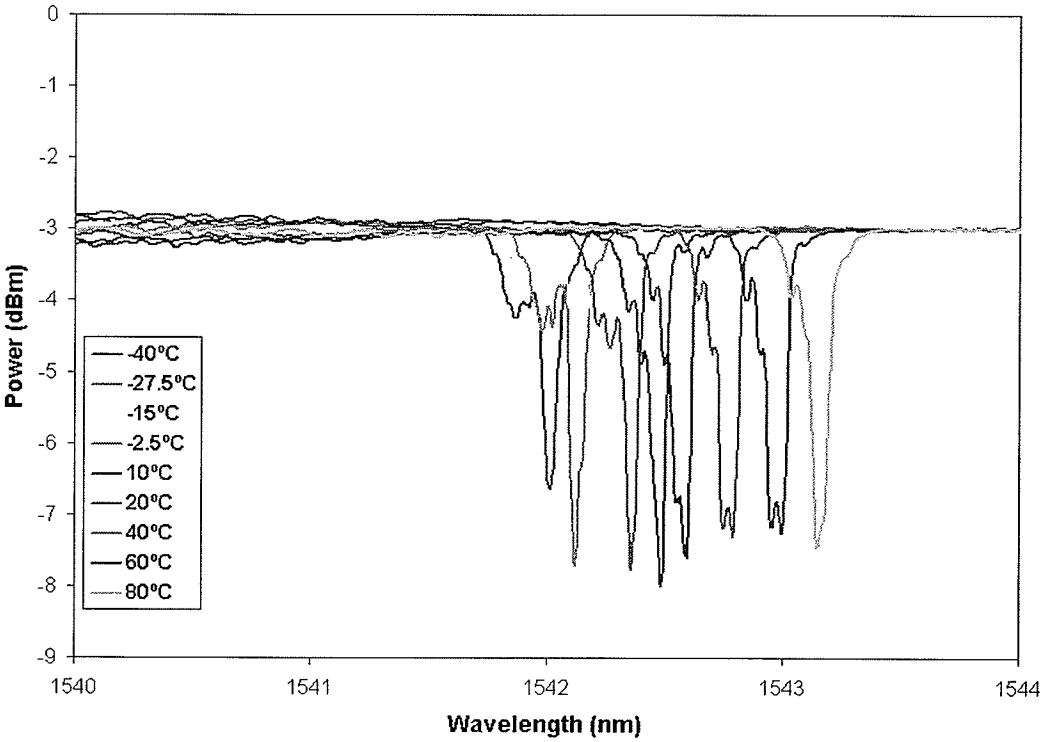

Figure 5.3b Transmission spectra of a side-polished FBG sensor in response to temperature variation.

Table 5.2 Summary of Bragg wavelengths in response to temperature/humidity variation.

Testing Condition	Bragg Wavelength (nm)	Standard Deviation (nm)
–40 °C	1542.011	0.00753
–27.5 °C	1542.114	0.01427
–15 °C	1542.249	0.009
–2.5 °C	1542.364	0.00602
10 °C, 85% RH	1542.493	0.00493
20 °C, 50% RH	1542.587	0.01951
20 °C, 70% RH	1542.592	0.00493
20 °C, 90% RH	1542.587	0.01208
40 °C, 30% RH	1542.758	0.01968
40 °C, 50% RH	1542.782	0.01968
40 °C, 70% RH	1542.777	0.02763
40 °C, 90% RH	1542.756	0.01968
60 °C, 10% RH	1542.013	0.004
60 °C, 30% RH	1542.997	0.02105
60 °C, 50% RH	1542.993	0.0237
60 °C, 70% RH	1542.989	0.0213
60 °C, 90% RH	1542.965	0.02432
80 °C, 10% RH	1543.182	0.0241
80 °C, 30% RH	1543.158	0.01571
80 °C, 50% RH	1543.163	0.01124
80 °C, 70% RH	1543.15	0.01334
80 °C, 90% RH	1543.141	0.01467

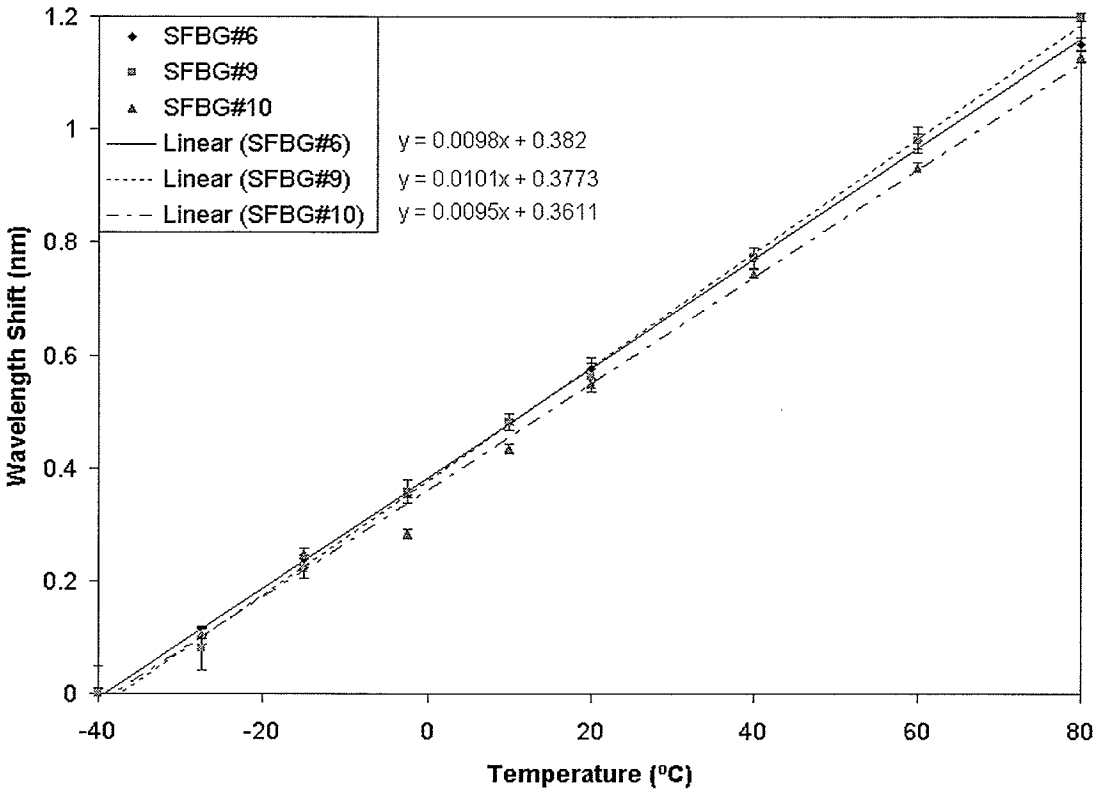

Figure 5.4 Bragg wavelength versus temperature of side-polished FBG sensors (with reference set at -40°C).

The temperature responses of the three side-polished FBG sensors are linearly fitted, with $R^2 > 0.995$, and indicate that the thermal induced Bragg wavelength shift (slope of the trend-line) of the side polished FBG sensors is approximately 9.8 pm/°C. The relative humidity data from Table 5.2 suggests that as the relative humidity increases, the Bragg wavelength shifts to shorter wavelengths, which would indicate lower environmental temperature, even though the temperature was held constant while changing the relative humidity. This may be explained by the fact that as the relative humidity increases, the moisture content in the air increases, and moisture deposition increases on the surface of the optical fiber grating section. With the two-way process of deposition and evaporation, the surface temperature becomes lower than that of the

atmosphere. From this characterization test, it is evident that keeping the temperature constant for refractive index experiment is critical because any temperature change of more than 1 °C introduces more than 10 pm shift of the Bragg wavelength, which would make refractive index change induced Bragg wavelength shift of the same magnitude insignificant.

5.3 Sucrose Solution Tests

This section describes the apparatus setup and experiment to gather the optical response of side-polished fiber Bragg grating sensors to different surrounding refractive indices. Sucrose solutions, mixed at different concentrations, were chosen to simulate different surrounding refractive index because they have fixed refractive index values at concentrations from 0% (n = 1.333) to 80% (n = 1.4906) at 589 nm and 20 °C (full table can be found in [44]). Taking into account for wavelength dependence of refractive indices, one can calculate the corresponding refractive indices at the operating wavelength. In this research work, the operating wavelength was 1550 nm, and sucrose solution concentrations from 30% to 67% were prepared for the experiment (with refractive index values calculated at the 1550 nm). Before the test could begin, however, a sensor probe needs to be fabricated to allow the side-polished FBG to be mounted and kept straight throughout the testing. Design of the sensor probe and experimental setup are described below.

5.3.1 Experimental Setup and Procedure

A sensor probe allowing the side-polished FBG to be immersed in sucrose

solutions for measurements was necessary. A U-shaped Plexiglas probe with a cut opening in the bottom section allows the side-polished FBG to be suspended in the surrounding medium (Figure 5.5). Once this probe is immersed in aqueous solutions, the distribution of force would be balanced throughout the entire length of the suspended section. This cut opening was designed to be 2 cm because the Bragg grating length for the side-polished FBG sensors were 2.2 cm. The optical fiber was then looped around the curvature and taped on the two ends, with the rest of the fiber looped around the circular structure on the top of the probe and ready to be immersed in aqueous solutions with known refractive indices for measurements.

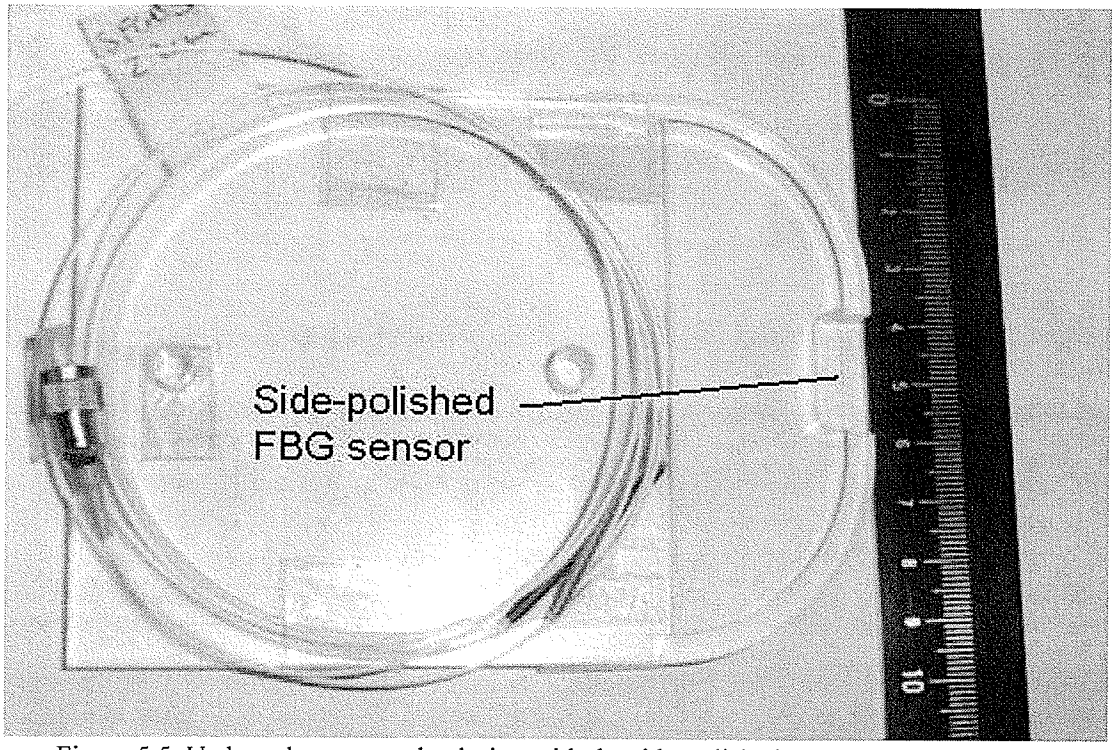

Figure 5.5 U-shaped sensor probe design with the side-polished FBG sensor suspended.

In the first set of tests, a broadband optical source sent light into the side-polished FBG surrounded by sucrose solutions prepared at different concentrations. The Bragg grating reflected light with its spectrum shifted according to the solution's refractive index. The reflected light traveled into a directional coupler and into an optical spectrum analyzer (ANDO^{TM} AQ6331). For transmitted optical spectra, the other end of the side-polished FBG was connected to the optical spectrum analyzer (see Figure 5.6 for a graphic illustration for the experimental setup). A set of five reflection and transmission spectra were recorded for each value of sucrose concentration, with the results averaged. The optical spectrum analyzer used for this experiment could only resolve 10 pm with repeatability; therefore, other interrogation unit capable of much higher resolution was necessary.

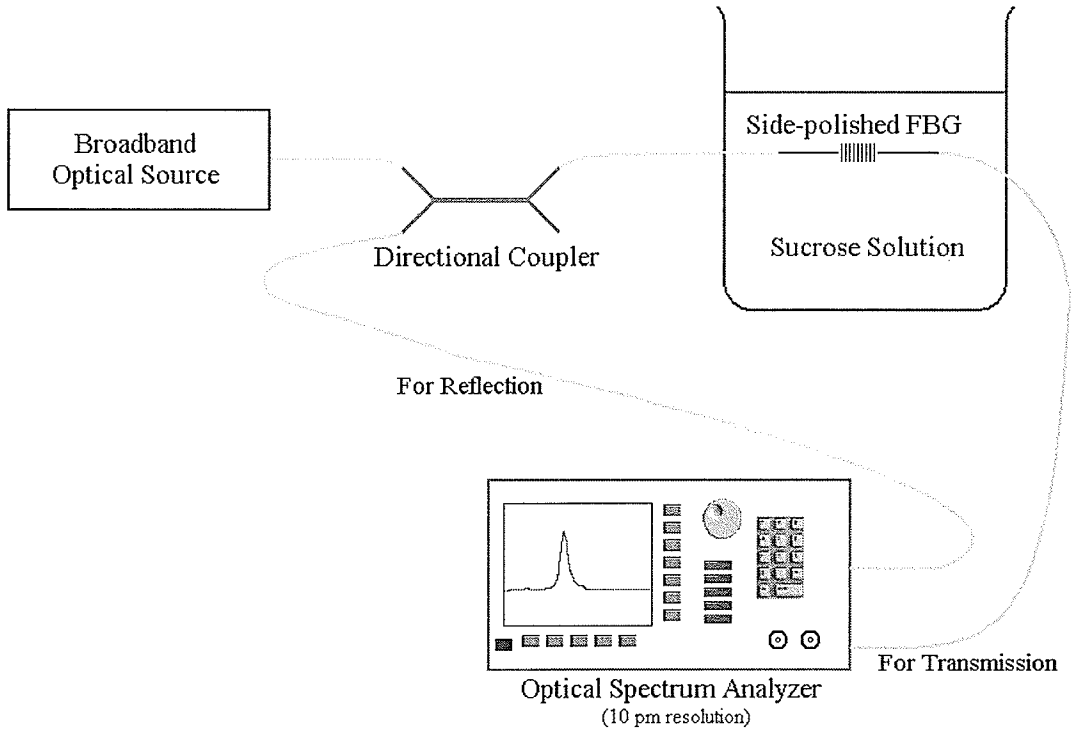

Figure 5.6 Sucrose solution experiment setup for side-polished FBG sensors.

In the second set of tests, an IDERS^{TM} SHM5100A^{TM} unit was employed for recording the Bragg wavelength locations. This interrogator has a built-in swept wavelength laser with gas cells for frequency reference and a peak fitting location detection algorithm [45]. The Bragg wavelengths were recorded at 100 samples per second over a two minute span. The Bragg wavelength locations data were then processed offline to determine the mean value as well as the standard deviation for error estimates. A picture of this setup is shown in Figure 5.7, with the side-polished FBG, immersed in a beaker containing sucrose solution, shown on the right hand side of the picture. One end of the side-polished FBG was connected to the interrogation unit. Since this interrogator required only the reflected spectra of the Bragg grating sensor, it was not necessary to connect the other end of the side-polished FBG.

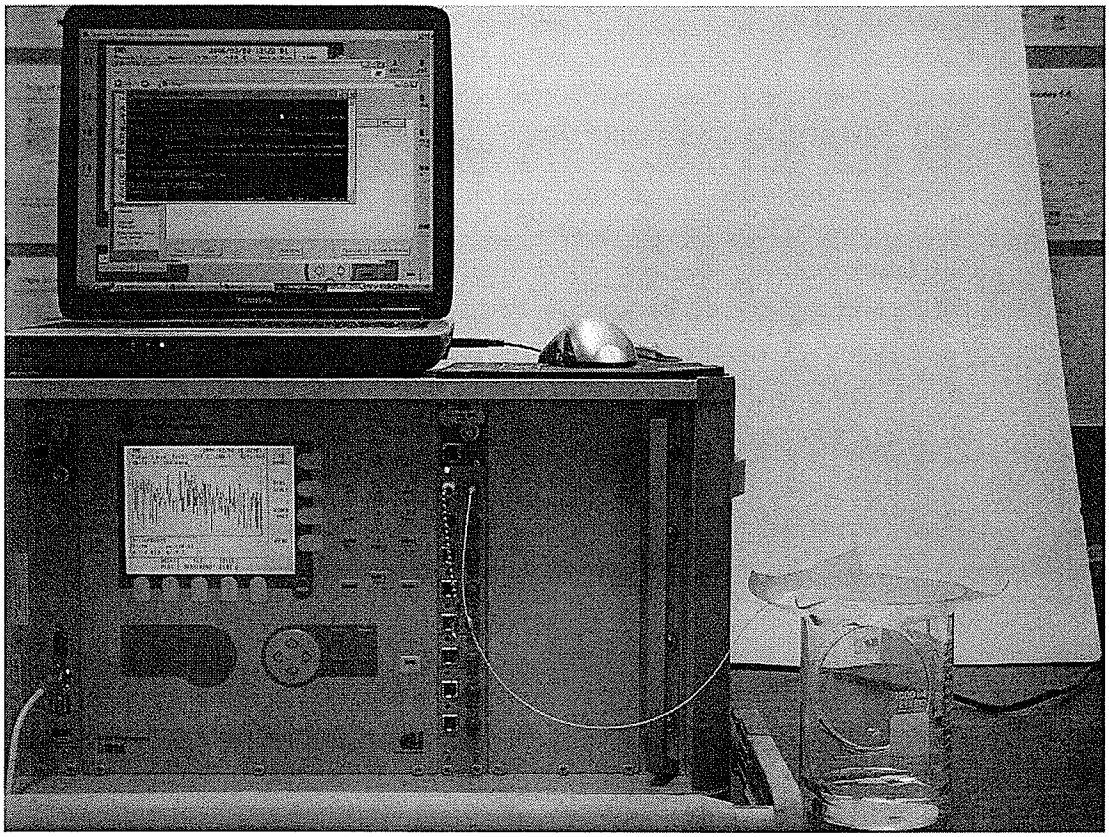

Figure 5.7 Experimental setup for side-polished FBG sensor involving IDERS^{TM} SHM unit.

5.3.2 Results and Analysis

The reflection and transmission spectra of the side-polished fiber Bragg grating sensors, immersed in sucrose solutions of different concentrations (converted into corresponding refractive index values), are shown in Figure 5.8. As the surrounding refractive index values increased, the peak (Bragg wavelength) of the reflected spectrum and the valley (Bragg wavelength) of the transmitted spectrum shifted to longer wavelengths.

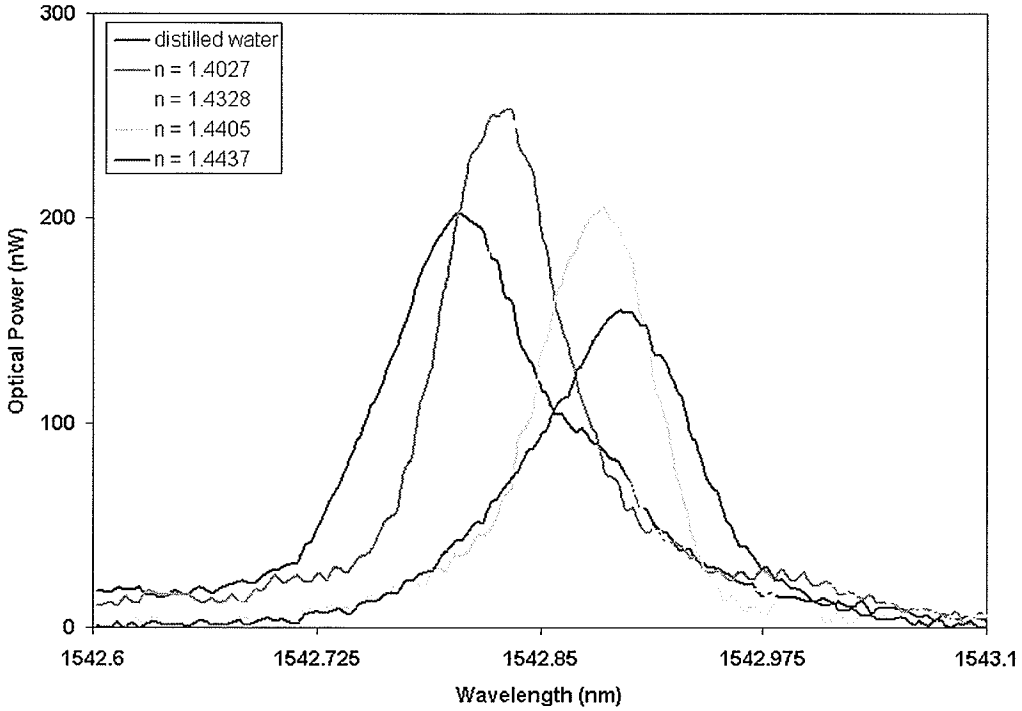

Figure 5.8b Transmission spectra of a side-polished FBG sensor in different sucrose concentrations.

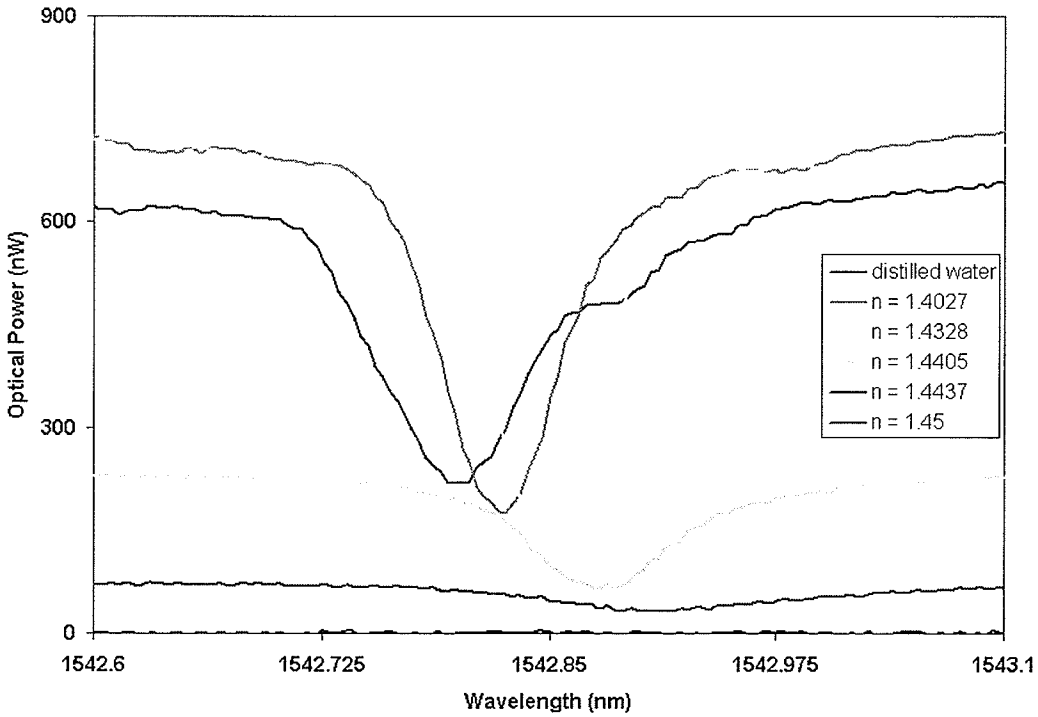

Figure 5.8b Transmission spectra of a side-polished FBG sensor in different sucrose concentrations.

The optical spectra provided insights to the trends that occurred, but the optical spectrum analyzer could only resolve 10 pm with accuracy. Therefore, the same experiment was repeated using an interrogator dedicated to Bragg grating sensors. More than 10,000 Bragg wavelength readings were recorded for each refractive index setting, and the results are shown in Figure 5.9. The wavelength shifts were referenced to the Bragg wavelength when the side-polished FBG sensor is immersed in distilled water. The error bars are specified at ±3 pm for the wavelength (repeatability of the interrogator) and ±0.002 for refractive index (uncertainty in the refractive index values converted from sucrose concentrations).

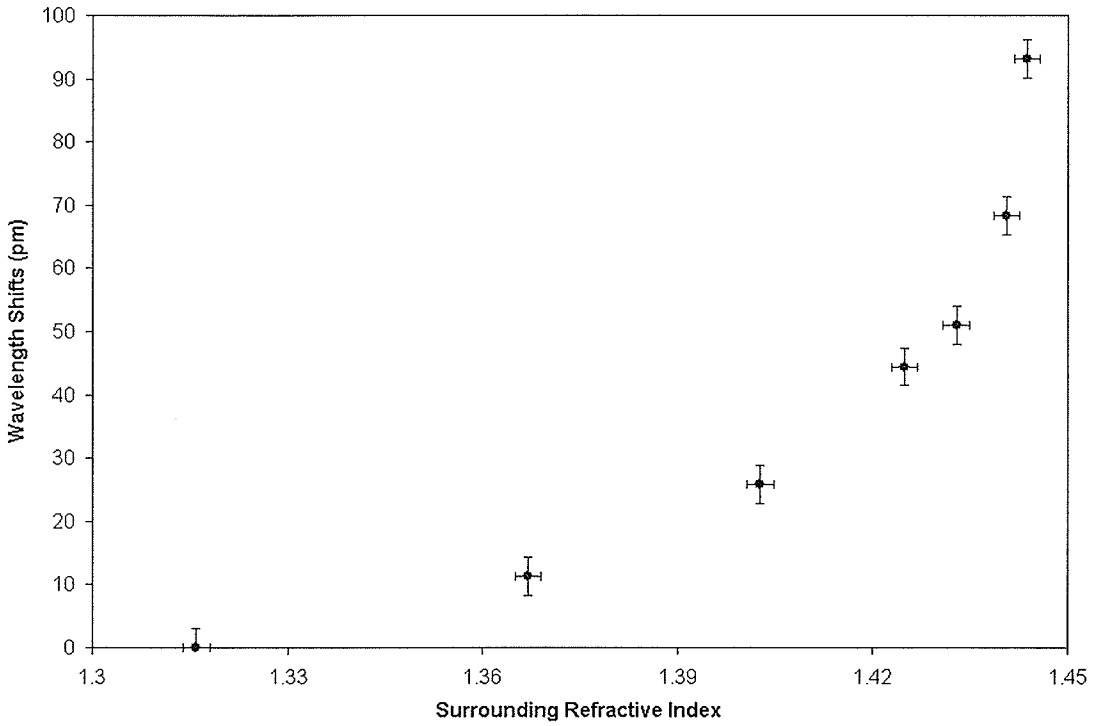

Figure 5.9 Side-polished FBG wavelength shift versus surrounding refractive index.

Slope from the final two data points represent the maximum wavelength shifts per surrounding refractive index, which was calculated to be 4.2 nm/riu. With the

repeatability of the interrogator being 3 pm, this means that the side-polished FBG sensor can detect a 7.14×10^{-4} change in the surrounding refractive index.

5.4 Simulation Prediction versus Experimental Results

The FEMLAB simulation results were compared to the experimental results. The simulation results were obtained in the format of effective index, and with the grating pitch parameter for the fiber Bragg grating, they were converted into Bragg wavelengths and the amount of wavelength shifts were referenced to n = 1.3. The simulated results and the experimental results are shown in Figure 5.10.

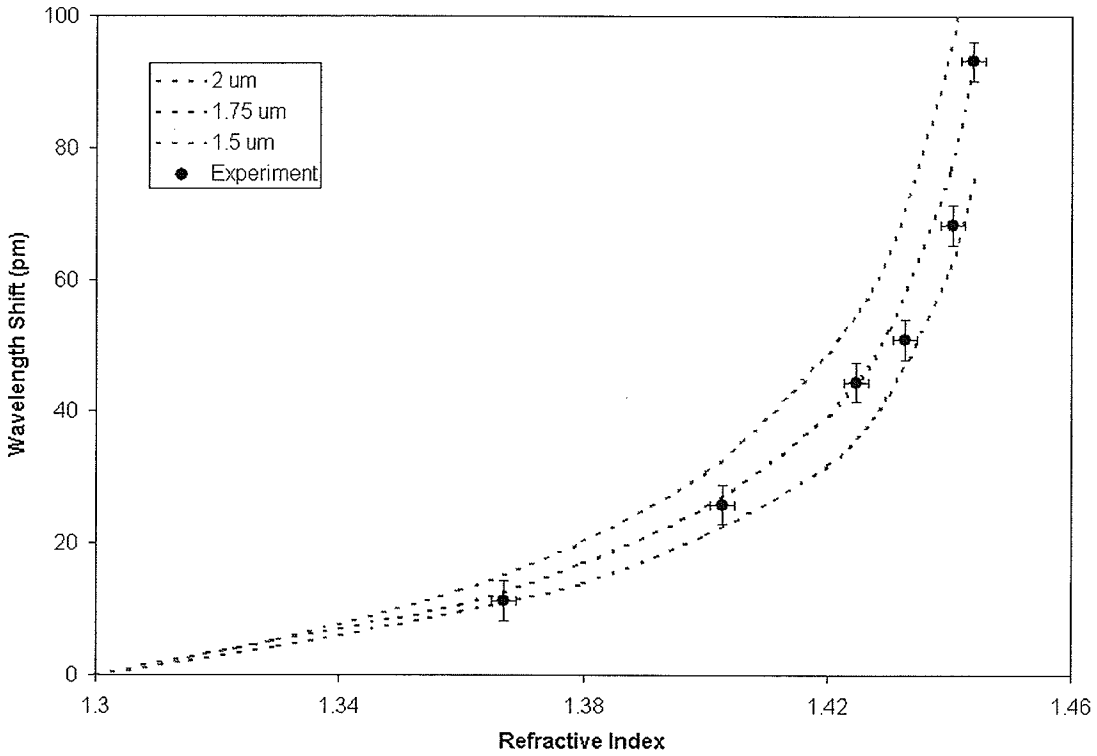

Figure 5.10 Side-polished experimental results compared with simulated data.

The experimental results show that the refractive sensitivity trend matches well against the simulation trend for 1.75 μm residual cladding thickness. The two outliers of

the trend appear at the higher refractive index values, but when the error bars are taken into consideration, the trend still shows a very good match to the simulation results. This indicates that more residual cladding can be removed to enhance the sensitivity according to the simulation results; however, FEMLAB simulation also indicated that the optical power could no longer be confined in the fiber core once the residual cladding thickness reaches less than one wavelength. This power loss (attenuation) trend was also observed while the chemical etching was performed prior to the refractive index experiments.

Chapter 6

Tilted Fiber Bragg Gratings

6.1 Introduction

This section describes the experimental tests that were performed on the tilted fiber Bragg gratings, which included a temperature/humidity characterization, a sucrose solution test, and a refractive index liquid test. A detailed description of the experiment apparatus and procedure is included. This chapter will conclude with the comparison between the simulation prediction and the actual experimental results and observations.

6.2 Characterization Tests

Similar to the side-polished fiber Bragg grating sensors, the tilted FBG sensors were placed in an environmental chamber and a series of temperature/humidity settings were run through to observe the optical response of the tilted FBG sensors. The set of temperature/humidity settings that were run was the same as the ones found in Table 5.1. The testing procedure and apparatus were also the same as the characterization test procedure and apparatus for the side-polished FBG sensors. However, instead of recording both the reflection and transmission spectra of the tilted FBG sensors, only the transmitted spectra were recorded because the cladding modes appear only in the transmitted spectra while only the Bragg resonance appear in the reflected spectra. A graphic illustration of the experimental apparatus is shown in Figure 6.1. A set of five transmission spectra were recorded at each environmental setting, with the individual

resonance wavelength results averaged and standard deviation calculated. The batch of tilted FBG sensors in the characterization tests included three tilted fiber Bragg gratings written on SMF28 fibers at 4°, one at 6°, two tilted fiber Bragg gratings written on 80 μm fibers, and two tilted fiber Bragg gratings written on 50 μm fibers.

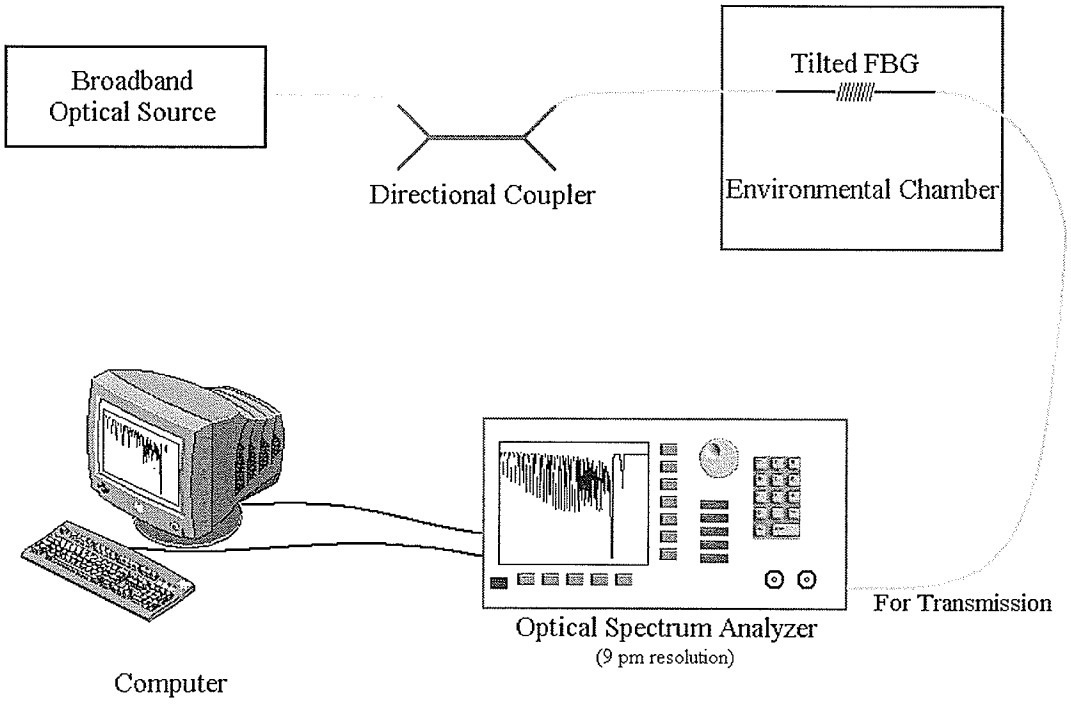

Figure 6.1 Characterization experiment setup for tilted FBG sensors.

The characterization experiment results suggest that the Bragg resonance and the various cladding modes shifted the same order of magnitude in wavelength due to temperature change, and this held true for all cases of tilted FBG sensors written on three different diameter fibers (SMF28, 80 μm, and 50 μm). Graphic illustrations of the thermally induced wavelength shifts of the optical spectra are shown in Figure 6.2. Note the three modes enclosed in each black circle in Figure 6.2, the three are the same mode (either Bragg or cladding mode). Linear fitting of the temperature induced wavelength

shifts are shown in Figure 6.3, with quantitative results of the thermally induced shifts listed in Table 6.1. The cladding modes listed in the table were located at some distances away from the Bragg resonance, and were chosen for analysis randomly. The experimental results strongly suggested that the relative distance between the Bragg resonance and various cladding modes do not depend on the temperature. The relative humidity, which had an influence on the Bragg wavelength shifts of the side-polished FBG sensors, was not a significant factor for tilted FBG sensors. This may be explained by the fact that the tilted FBG sensors retain the entire fiber cladding material, surface moisture deposition and evaporation at high RH take place much further away from the Bragg grating than in the case of the side-polished FBG sensors.

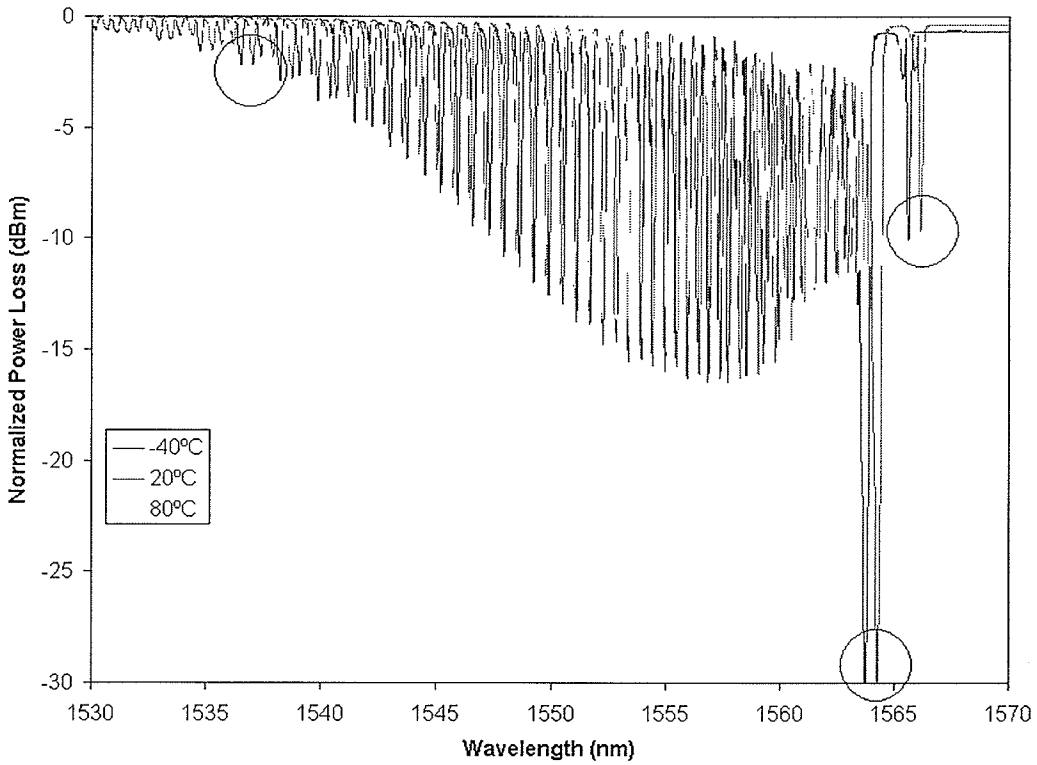

Figure 6.2a Temperature-induced shift of tilted FBG spectrum (125 μm diameter fiber).

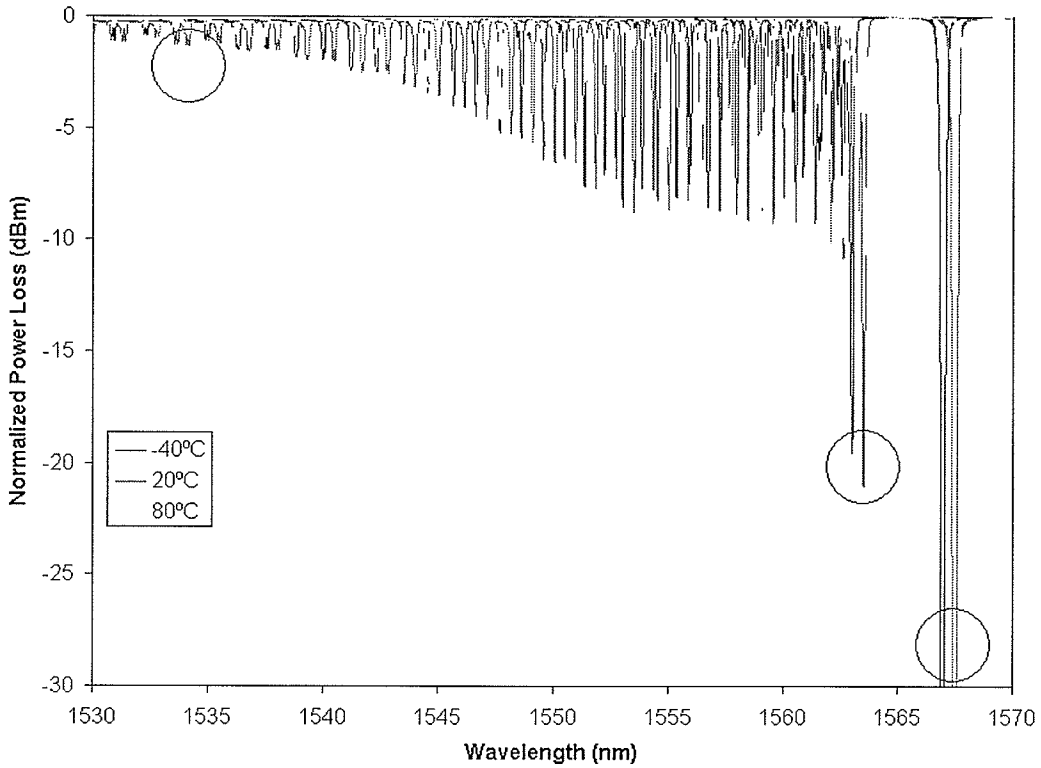

Figure 6.2b Temperature-induced shift of tilted FBG spectrum (80 μm diameter fiber).

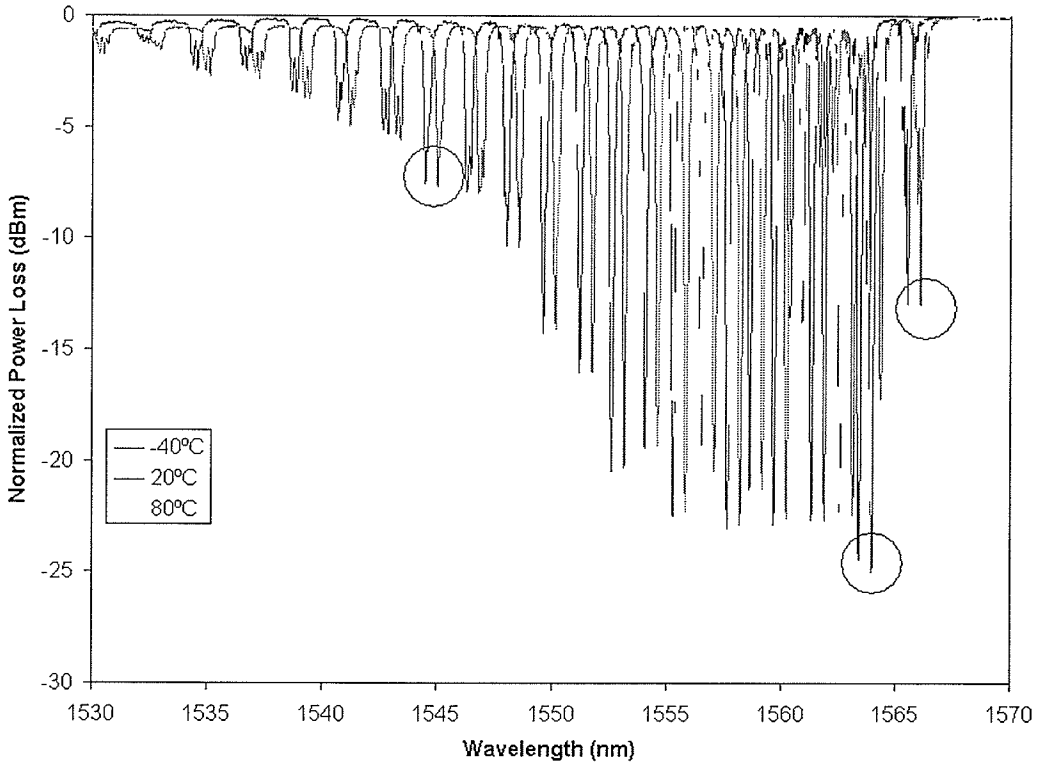

Figure 6.2c Temperature-induced shift of tilted FBG spectrum (50 μm diameter fiber).

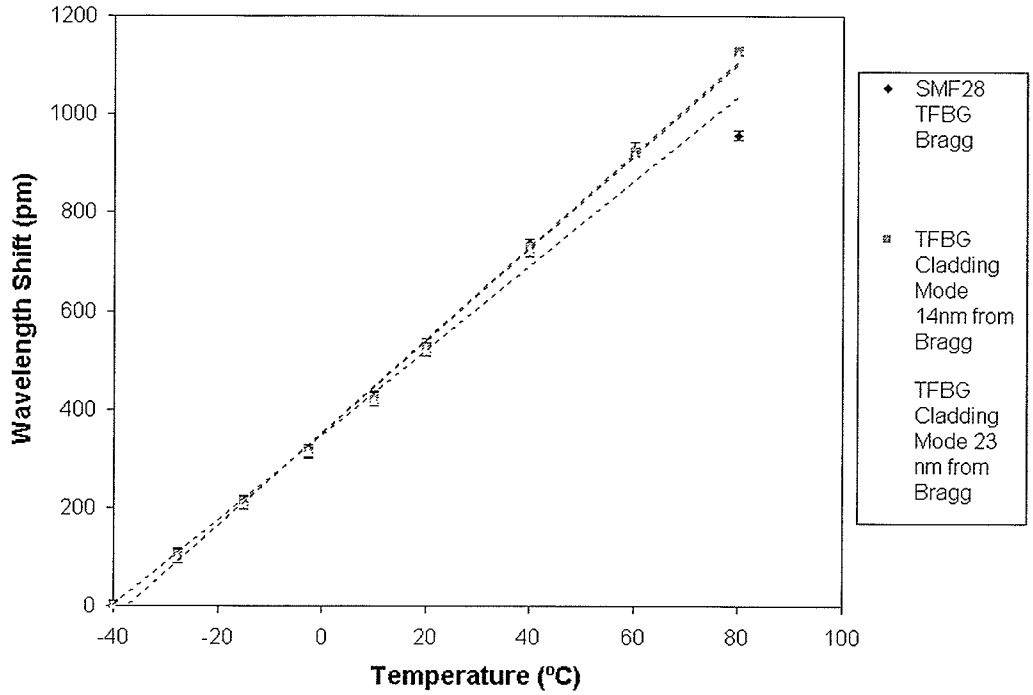

Figure 6.3a Wavelength shifts of different modes versus temperature variation (125 μm diameter fiber).

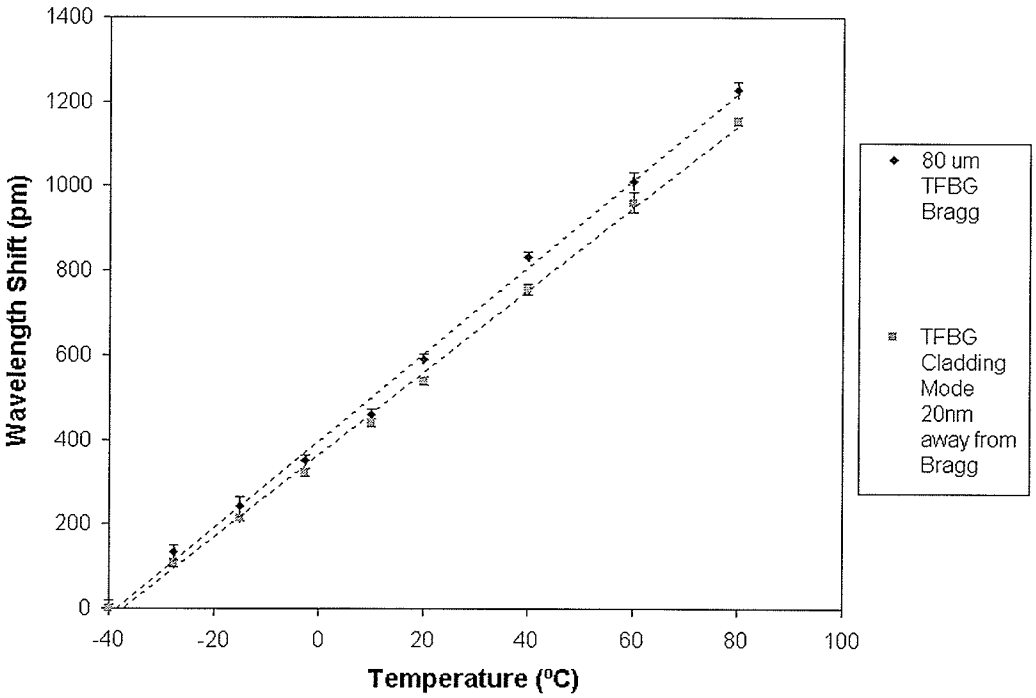

Figure 6.3b Wavelength shifts of different modes versus temperature variation (80 μm diameter fiber).

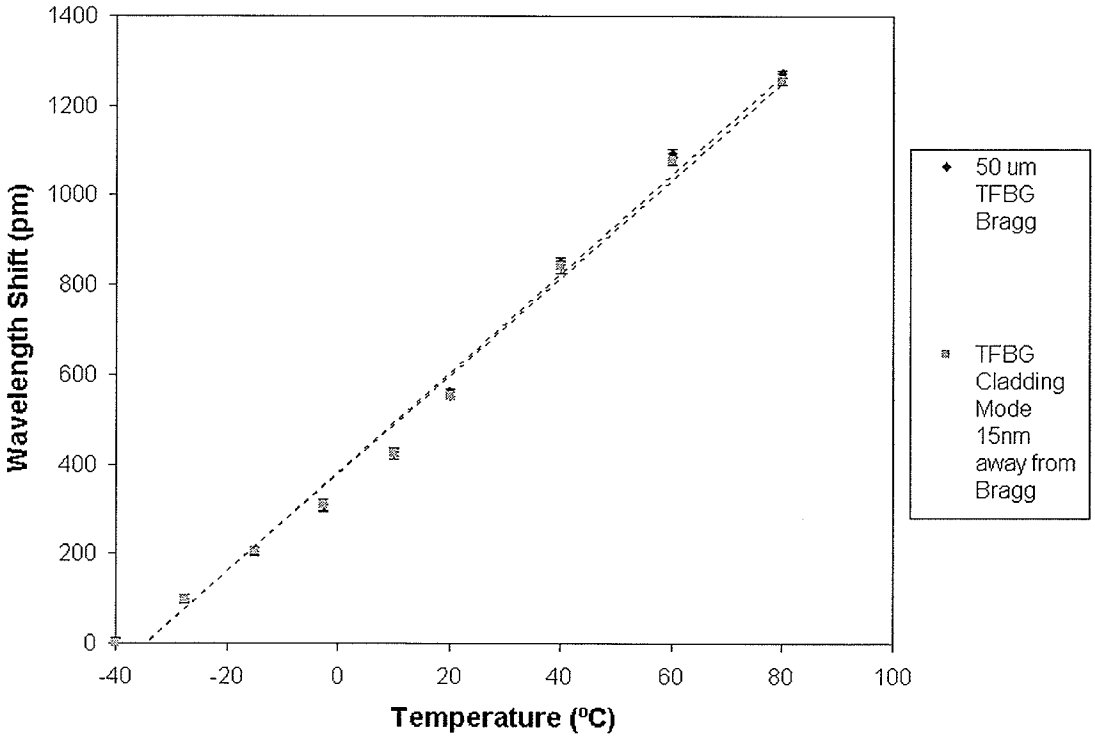

Figure 6.3c Wavelength shifts of different modes versus temperature variation (125 μm diameter fiber).

Table 6.1 Summary of temperature-induced wavelength shifts of Bragg and select cladding modes of different diameter fibers.

Fiber Type	Mode	Thermally induced wavelength shift (pm/°C)	R^2
Corning SMF28	Bragg	8.6	0.9869
	Cladding mode 14 nm from Bragg	9.4	0.9978
	Cladding mode 23 nm from Bragg	9.4	0.9981
Corning 80 μm	Bragg	10.3	0.9974
	Cladding mode 20 nm from Bragg	9.7	0.9982
Corning 50 μm	Bragg	11.1	0.9903
	Cladding mode 15 nm from Bragg	10.9	0.9909

Results from the temperature/humidity characterization test indicate that the temperature fluctuation would not confuse with the refractive index induced wavelength shifts. However, for best experimental accuracy, the temperature at which the refractive index testing was done should be kept constant to minimize the thermo-optic effects of aqueous solutions.

6.3 Refractive Index Measurements via Sucrose Solutions

6.3.1 Experimental Setup and Procedure

The experimental setup for the sucrose solution measurements included a broadband optical source, a directional coupler, a batch of various tilted FBG sensors placed on a fiber holder that was placed in a glass container, a magnetic stir to mix the solutions, an optical spectrum analyzer and a computer connected to the optical spectrum analyzer to record data (see Figure 6.4 for an illustration). Since only the transmitted spectra were of interest for the experiment on tilted FBG sensors, no reflected spectra were recorded. A set of five transmitted spectra for each tilted FBG were recorded at each sucrose concentration setting, and the resonance locations were averaged and the standard deviation taken. The data processing was done offline after the recording all of the optical spectra.

Sucrose solutions were prepared by mixing 400 g of sucrose in 200 g of de-ionized water, and as the experiment went on, more de-ionized water was added to the solution to produce different concentrations. Concentrations used for this experiment were, in sequential order according to the experiment, 66.67%, 66.45%, 65.57%, 64.52%, 62.5%, 60%, 57.14%, 53.33%, 50%, 44.44%, 40%, 36.36%, 33.33%, 30%, and de-

ionized water measurement was taken separately for reference purposed. The magnetic stir was running continuously to ensure uniform concentration distribution across the fluid, and a film covered and sealed the top of the container to prevent evaporation (which would cause the sucrose concentration to increase over time). Before recording the measurements at a new concentration, sufficient amounts of time were given for the stabilization. The temperature, as a result of running the stir continuously, was thus not held constant. However, the temperature independence of the relative distance between the Bragg resonance and the cladding modes means that the effect of thermal drift would be minimized for refractive index measurements.

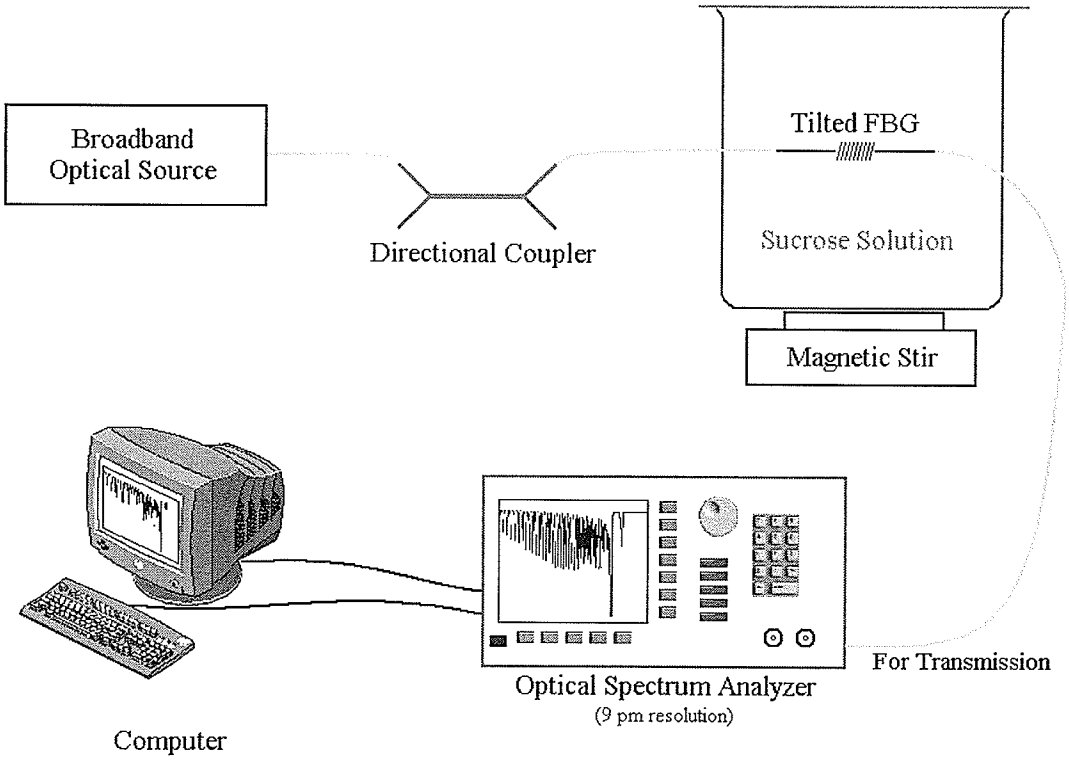

Figure 6.4a Tilted FBG sucrose solution experiment setup.

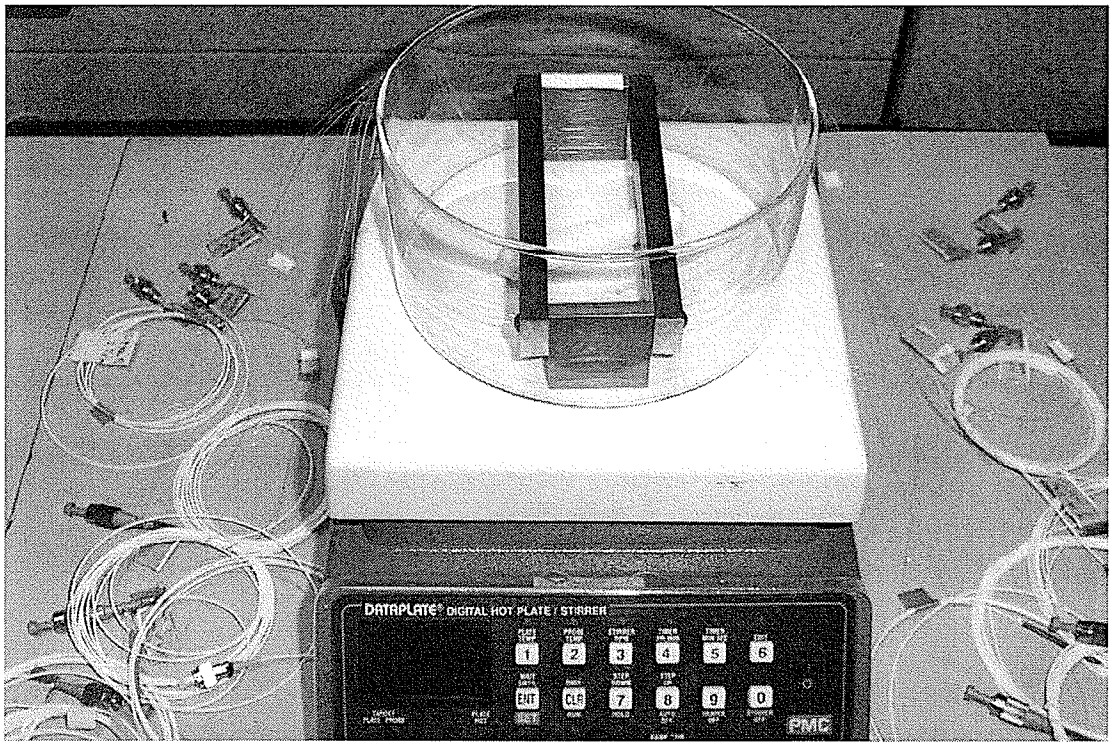

Figure 6.4b Tilted FBG sensors placed in a container on a magnetic stir.

6.3.2 Resonance Location Methods

To accurately analyze the experimental data, a good resonance location algorithm was necessary to accurately locate the Bragg and the cladding mode resonance wavelengths. Each individual resonance in a tilted FBG is asymmetric due to the asymmetric structure of the grating; therefore, peak fitting was not done to extract the resonance locations. The resonance location must satisfy the following criteria:

1) the data point must be a local minimum within ±200 pm;

2) it must be more than 3 dB down from either the shorter or longer wavelength side;

3) only in the case of multiple valleys, peak fitting was done to determine the resonance location.

Resonance wavelengths were outputted using the algorithm. In the cases involving multiple valleys (noise in the mode resonance), they were in fact not considered for experimental analysis. Furthermore, most of the modes whose resonance showed significant noise occurred on the extreme (much shorter wavelength) end of the spectra that they did not satisfy the first two criteria. In the modes chosen for further analysis, only the ones with clearly defined resonance wavelengths were considered.

6.3.3 Results

The experimental data showed that while the Bragg resonance wavelength remained the same throughout the experiment, each individual cladding mode responded differentially to changes in the sucrose concentration (see Figure 6.5). Wavelength shifts in the relative distances between the Bragg resonance and select individual cladding resonances were measured and plotted against the sucrose concentration and shown in Figure 6.6 for 4° and 6° tilted FBG, 80 μm 4° tilted FBG, and 50 μm 4° tilted FBG. Actual refractive index values were not calculated for the sucrose concentrations since the sole purpose of this test was to obtain a picture of the magnitude of wavelength shift of the tilted FBG sensor compared to that of the side-polished Bragg grating sensors. The results demonstrated that the tilted FBG sensors exhibited maximum sensitivities (slope between the final two data points) of 0.02% sucrose concentration change, in the range between 40% and 66% sucrose concentration, by utilizing different cladding modes for analysis. The tilted FBG sensor written on a 50 μm diameter fiber showed a maximum sensitivity of 0.01% sucrose concentration change.

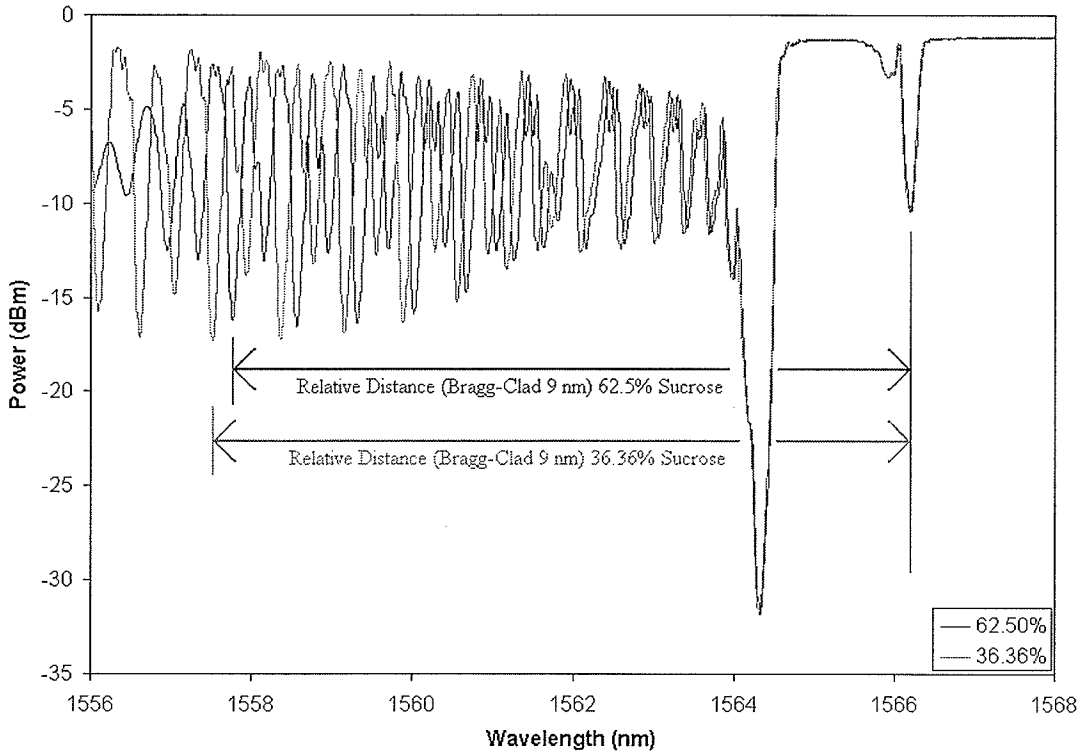

Figure 6.5 Differential response of cladding modes to surrounding refractive index.

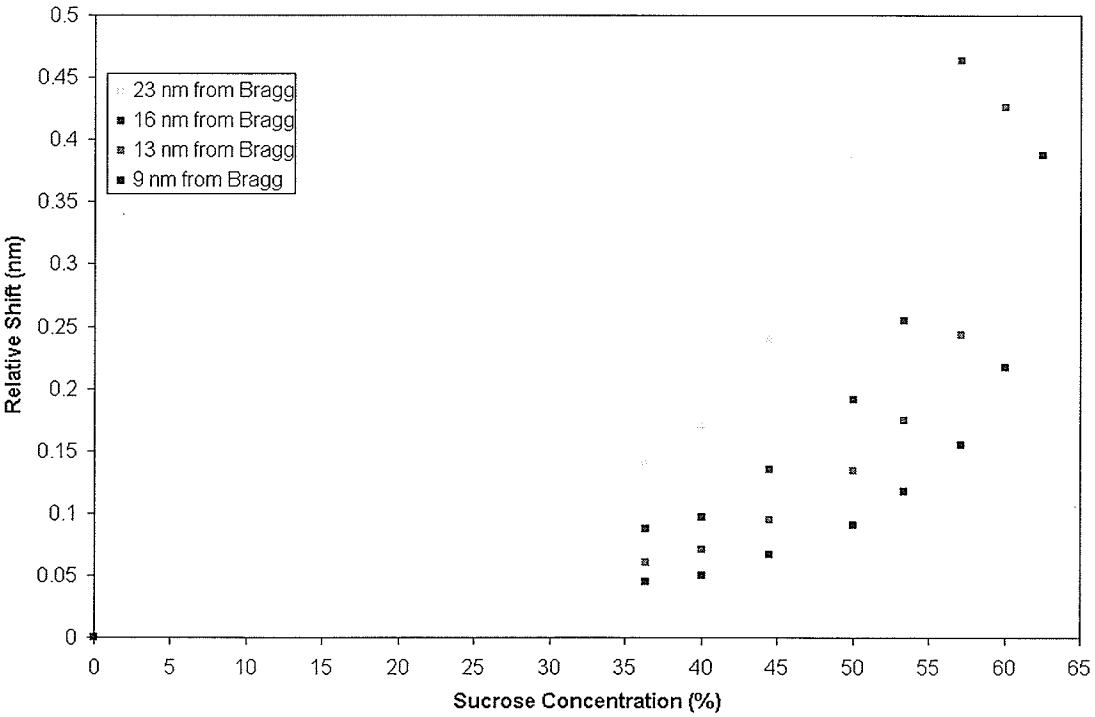

Figure 6.6a Relative distances between cladding modes and the Bragg resonance versus sucrose concentration (125 μm, 4° tilt).

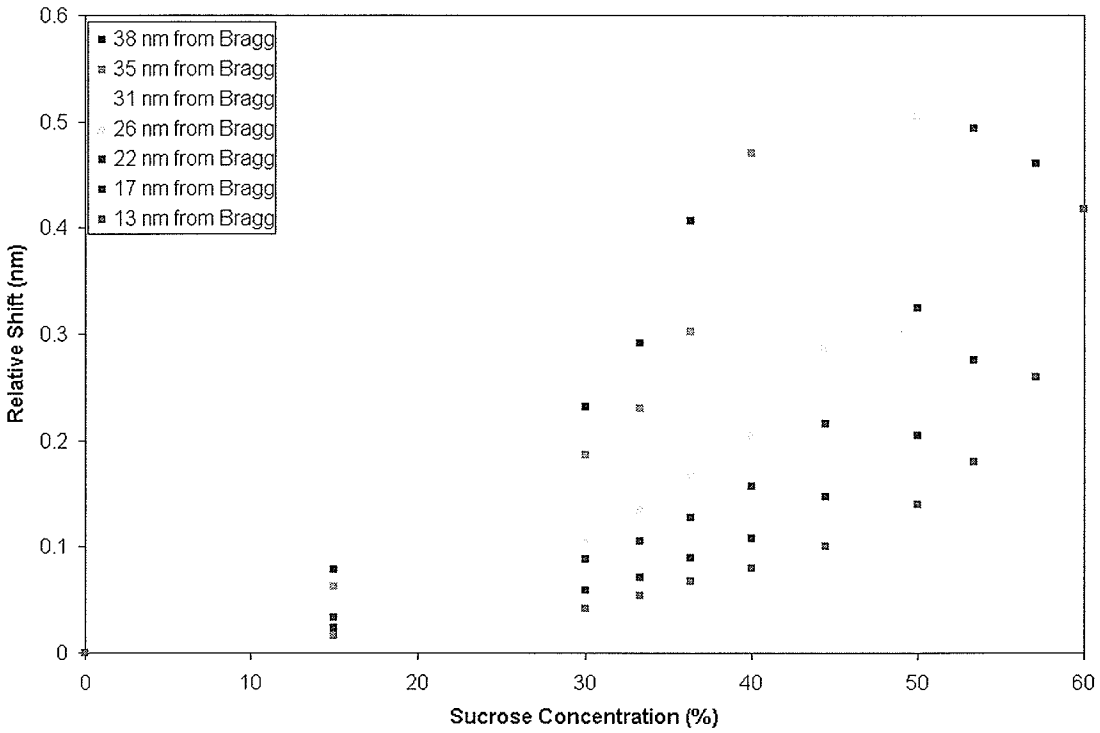

Figure 6.6b Relative distances between cladding modes and the Bragg resonance versus sucrose concentration (125 μm, 6° tilt).

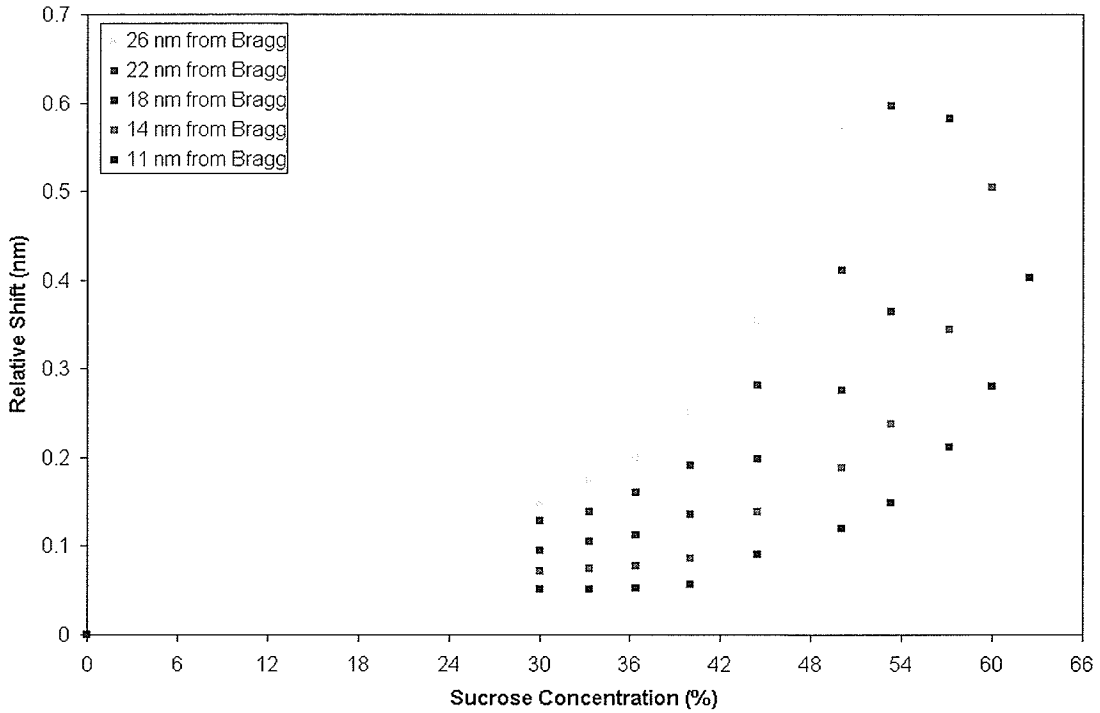

Figure 6.6c Relative distances between cladding modes and the Bragg resonance versus sucrose concentration (80 μm).

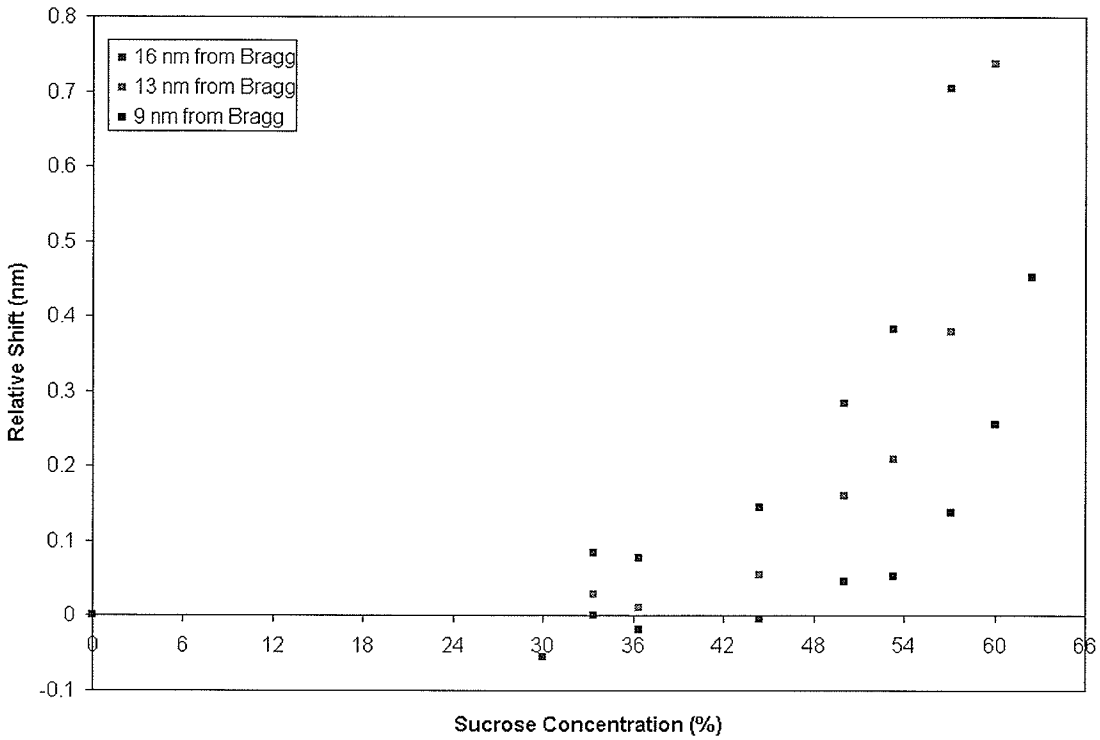

Figure 6.6b Relative distances between cladding modes and the Bragg resonance versus sucrose concentration (50 μm).

The results showed a trend that as the sucrose concentration increased (hence the surrounding refractive increased), the shifts became larger and the sensitivity increased. The ultimate sensitivity increased for tilted FBG written on thinner diameter fibers. The sensitivity trend held true for all of the tilted FBG sensors except for the 50 μm tilted FBG. The reason behind this was that one end of the optical fiber splicing on both 50 μm tilted FBG sensors were broken as the experiment was set underway. As a result, only one was useful for measurement because the cleavage still showed a 4% reflection, which could still be used for monitoring the spectrum. However, the results were so unpredictable because the reflection was noisy. This brings forward an important observation that while reducing the cladding thickness enhanced the ultimate sensitivity, the much reduced mechanical stability negated its benefits.

6.4 Refractive Index Measurements via Refractive Index Liquids

6.4.1 Experimental Setup and Procedure

For this experiment, only the 4° tilted FBG sensors written on SMF28 fiber were used due to its mechanical stability and connector availability. The basic idea in this experiment was to measure the transmission spectra of the tilted FBG sensors immersed in different media with know refractive indices and to record the suitable resonances as a function of surrounding refractive index. The transmission spectra were recorded using a JDS Uniphase swept wavelength system with a wavelength resolution of 3 pm. All the readings were done at room temperature, which was kept near 23 °C. To keep the strain on the fiber constant during the experiments, the fiber region where the grating was written was attached permanently to a microscope slide with the two ends of the fiber fixed and small quantities of liquids with various refractive indices were dispensed with a pipette onto the grating. A second slide was used to cover the interaction region and to maintain the liquid in place by capillarity. The fiber and slides were cleaned thoroughly using distilled water and then methanol between experiments. The transmission spectrum was monitored during the cleaning and compared to the reference spectrum (spectrum when tilted FBG is surrounded by air) real-time, and the cleaning was complete when the two spectra matched. The immersion liquids used in these experiments were calibrated liquids from Cargille Corporation with refractive indices specified for all wavelengths and temperatures of interest in the measurements. Therefore, the experimental conditions were sufficiently well controlled (for strain and temperature) to ensure reliable, reproducible results.

In addition to the JDS Uniphase swept wavelength system measurements, a Micron Optics si720 interrogator, a dedicated fiber Bragg grating interrogation equipment, was used repeat the refractive index experiments. This interrogator has a wavelength measurement accuracy better than 1 pm [46], and it has a built-in resonance location algorithm whose criteria can be adjusted by the user based on the specific sensors. With such an instrument, the refractive index experiments were repeated with the exact same experimental conditions and procedures, the repeatability of the measurement of wavelength distance (standard deviation of successive measurements of a fixed experimental situation) of 0.6 pm. Because of the fact that two separate equipments were used for the exact same sensors and experimental conditions and procedures, reproducibility of the experimental results was verified. The results and analysis are presented in 6.4.3.

6.4.2 Interrogation and Resonance Location Methods

Two separate interrogation systems were used for the refractive index liquids experiments, a JDS Uniphase swept wavelength measurement system and a dedicated fiber Bragg grating interrogator Micron Optics si720. For the JDS Uniphase system, light of four orthogonal polarization states were launched into the tilted fiber Bragg gratings at each wavelength, and collected at the detector, then a built-in software calculated the average power between the four polarization states. Since the measurement system recorded the averaged results of the four orthogonal polarization states, the polarization dependence was negligible in the data recorded. The Micron Optics si720 launched only one state of polarization into the tilted fiber Bragg grating

sensors, thus the polarization dependence was significant (up to 100 pm difference). However, the procedures followed in the experiments ensured that no displacing or twisting of the optical fiber took place because the fiber Bragg gratings were fixed on the two ends and remained so even during and after thorough cleaning. This carefully designed testing procedure not only ensured constant longitudinal strain, but also constant polarization condition.

The resonance locations for transmission spectra taken with the JDS Uniphase swept wavelength system were analyzed after the experimental measurements. As described earlier in the sucrose solution tests, the cladding modes exhibited asymmetry and thus no peak-fitting should be done. The criteria that were used to determine the valid resonance locations are listed below:

1) The resonance must be a local minimum in the full-width at half-maximum (200 pm)

2) The resonant mode must be more than 3 dB deep from either side

Analysis of the entire set of transmission spectra revealed that no multiple peaks/valleys were present for the tilted FBG sensors written on SMF28 fibers, thus the two criteria listed above were sufficient in determining the resonance locations. The same criteria were set as the resonance locating parameters in the Micron Optics si720 interrogator, and the interrogator recorded the resonance locations in real-time. Full transmission spectra were also recorded to carefully analyze the resonance to eliminate any ambiguities (such as the borderline resonances seen by the software that were obviously meaningless). The resonance locations data were taken over a ten minute span and recorded every second; therefore, a sufficiently large number of data points were used for

statistical analysis and interpretation.

6.4.3 Experimental Results

The transmission spectra from the first set of experiments using the JDS Uniphase swept wavelength measurement system are plotted in Figure 6.7. The plots show the tilted FBG spectra when surrounded by different refractive index media. Note that the Bragg resonance remains at the same wavelength location while the cladding modes exhibit differential shift, all in the same direction, when surrounded by different refractive indices. The temperature and strain were held constant throughout the experiment; therefore, shifting of the cladding mode resonances came as a direct result of changes in the surrounding refractive index.

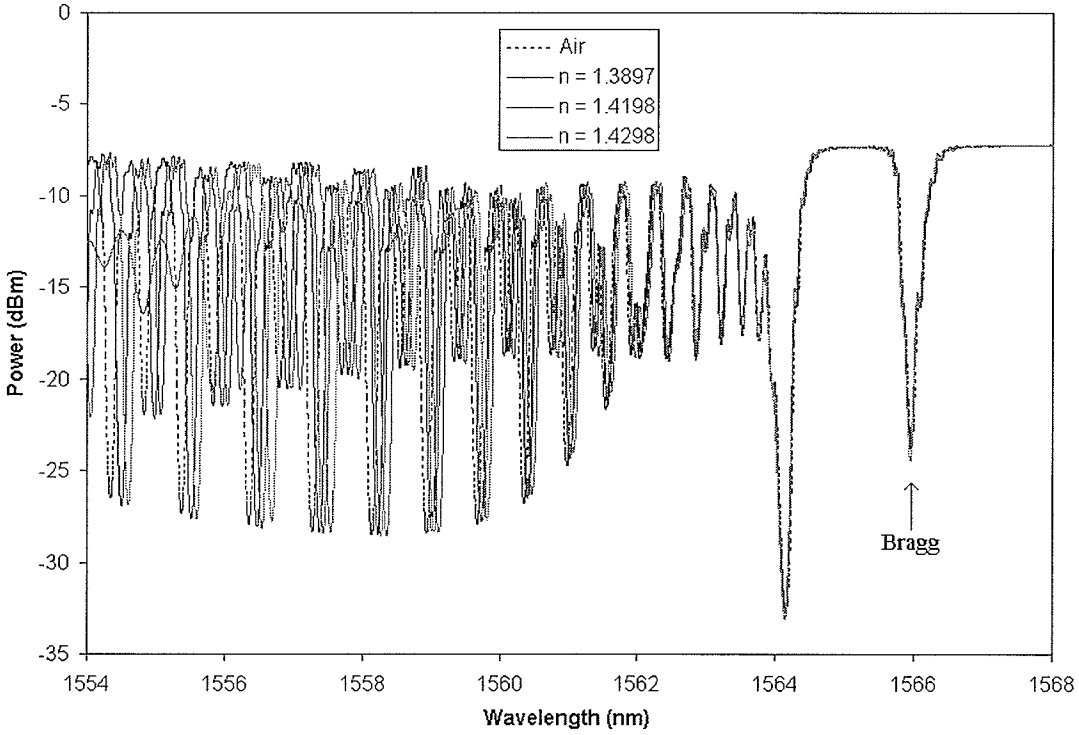

Figure 6.7 Transmission spectra of a tilted FBG to different external refractive indices.

Select cladding modes, located at 8, 14, and 23 nm away from the Bragg resonance, were chosen for analysis because the simulation results were represented by these modes. Relative distances between the chosen cladding modes and the Bragg resonance were calculated, and the amount of wavelength shifts was calculated with reference to the relative distances when the tilted FBG sensors were surrounded by air. The relative wavelength shifts are plotted in Figure 6.8, with no lines connecting through the data points. Error bars are included and errors are specified at ±3 pm in terms of the wavelength (the repeatability and resolution of the swept wavelength measurement system) and ±0.0002 for refractive index values (specified by Cargille Corporation for their refractive index liquids).

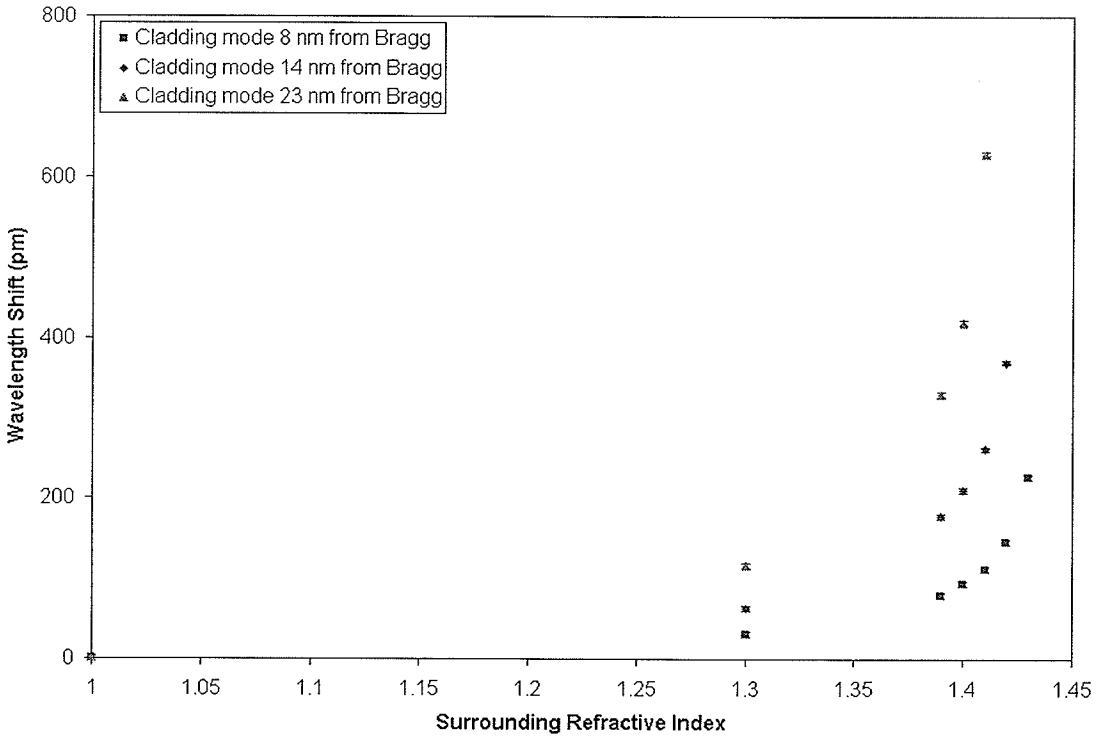

Figure 6.8 Relative distances between cladding modes and the Bragg resonance at different surrounding refractive index values (taken with JDS Uniphase swept wavelength system).

Slope from the final two data points of each curve (each cladding mode) indicates the maximum refractive index sensitivity of each cladding mode. For the cladding mode located at 23 nm away from the Bragg resonance, the maximum sensitivity determined from the experimental data is 21 nm/riu around $n_{ext} = 1.405$. The maximum sensitivities of the cladding modes 14 and 8 nm away from the Bragg resonance are 10.8 nm/riu and 8.1 nm/riu, near $n_{ext} = 1.415$ and $n_{ext} = 1.425$, respectively. When assuming a 3 pm repeatability (which was the case with the JDS Uniphase measurement system), cladding modes at 23, 14, and 8 nm away from the Bragg can detect a Δn_{ext} of 1.43×10^{-4}, 2.79×10^{-4}, and 3.69×10^{-4}, respectively.

The same refractive index liquids experiments were repeated using the Micron Optics si720 Model as the interrogator. A minimum of 600 data points for each cladding mode were analyzed for each of the refractive index values tested. Again, shifts of the relative distances between the exact same cladding modes were calculated with reference to the relative distances when the tilted FBG sensors were surrounded by air. The results are plotted in Figure 6.9 without any lines connecting through the data points to accurately portray the experimental results. Error bars are specified as ±0.6 pm for wavelength (the experimentally verified repeatability of the interrogator) and ±0.0002 for refractive index values.

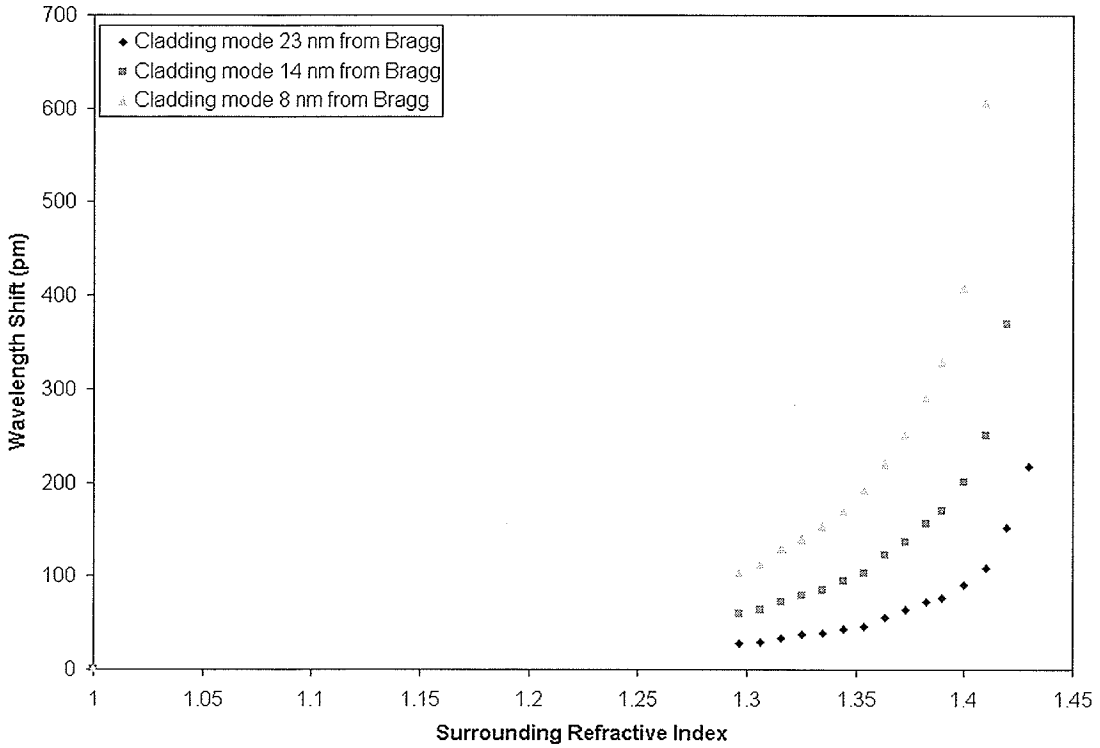

Figure 6.9 Relative distances between cladding modes and the Bragg resonance at different surrounding refractive index values (data taken with MicronOptics si720 interrogator).

Again, slope from the final two data points of each cladding mode curve indicates the maximum refractive index sensitivity of each cladding mode. For the cladding mode located at 23 nm away from the Bragg resonance, the maximum sensitivity determined from the experimental data is 19.8 nm/riu around $n_{ext} = 1.405$. The maximum sensitivities of the cladding modes 14 and 8 nm away from the Bragg resonance are 11.8 nm/riu and 6.54 nm/riu, near $n_{ext} = 1.415$ and $n_{ext} = 1.425$, respectively. When assuming a 1 pm repeatability (although the experimentally verified repeatability of the Micron Optics si720 was 0.6 pm, 1 pm was used as a safer assumption), cladding modes at 23, 14, and 8 nm away from the Bragg can detect a Δn_{ext} of 5.01×10^{-5}, 8.44×10^{-5}, and 1.53×10^{-4}, respectively. As both sets of experimental data suggest, tilted FBG sensors have the ability to detect better than 1×10^{-4} of refractive index change in the surrounding

medium in a large range from 1.38 to 1.43, simply by choosing different cladding modes for analysis.

6.5 Simulation Prediction versus Experimental Results

The simulation data were taken to be compared against the experimental results taken from both the JDS Uniphase measurement system and Micron Optics si720 interrogator. The results are plotted in Figure 6.10 with the lines representing the simulated results and the individual points representing the experimental results. The experimental data and simulation results show excellent agreement, implying that the simulation can be used to predict the actual refractive indices of the surrounding medium given a known spectrum and an unknown value of surrounding refractive index with a reference spectrum (transmission spectrum of tilted FBG surrounded by air).

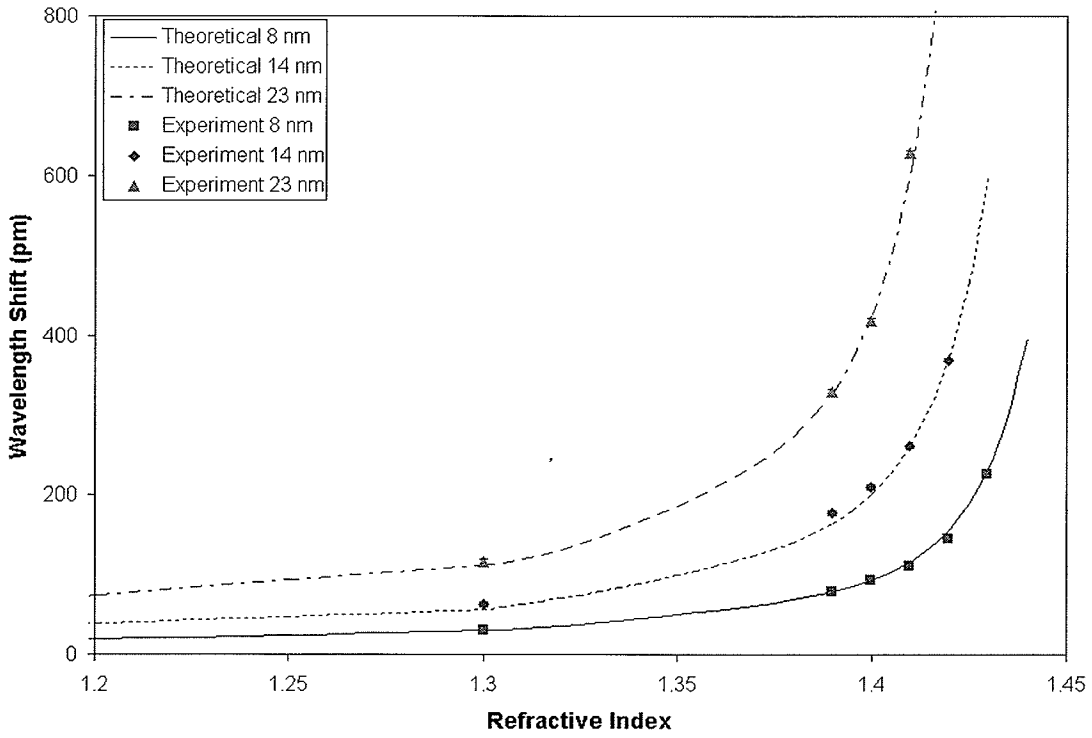

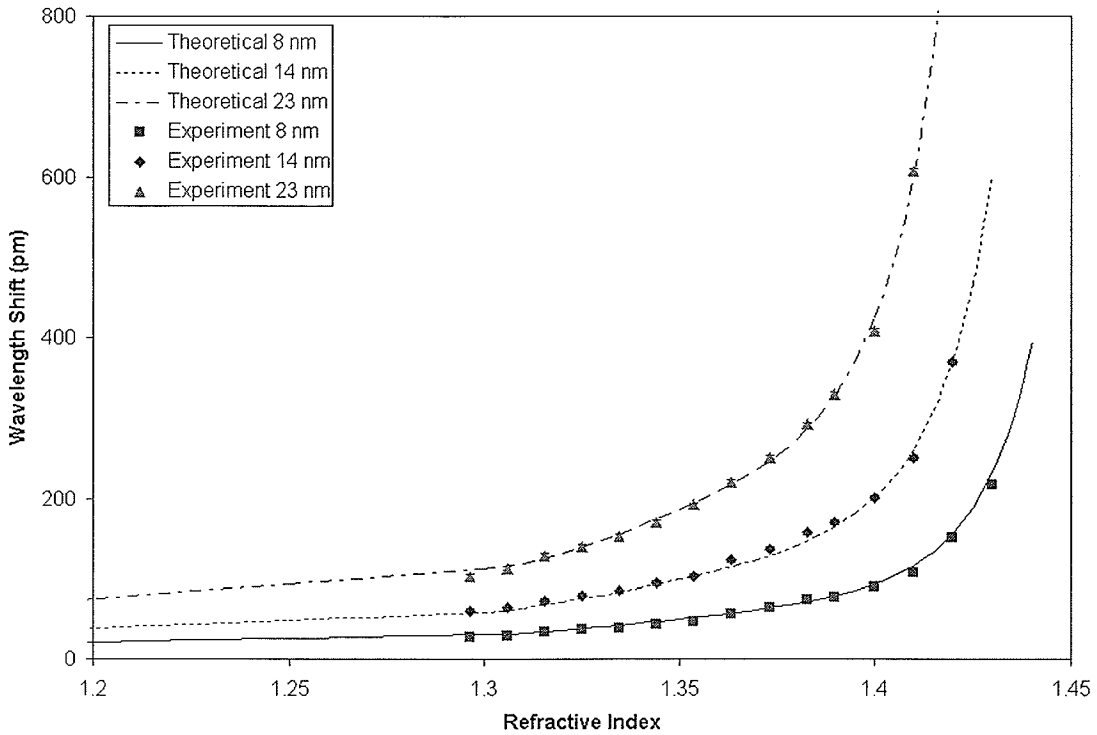

Figure 6.10 Tilted FBG experimental data compared with Opti*Grating* simulation results, top) experimental results taken with JDS Uniphase system; bottom) results taken with MicronOptics si720.

Since the simulation results serve as an excellent prediction tool, experimentally obtained Bragg-cladding mode distances were used to find the surrounding refractive index value the simulations suggest they were. Results from the three cladding modes were averaged to reduce statistical errors in terms of the measurements. Tilted grating measured surrounding refractive index values were then plotted against the actual refractive indices used in the experiments, with the results shown in Figure 6.11, including a linearly fitted line showing its slope and R^2 value.

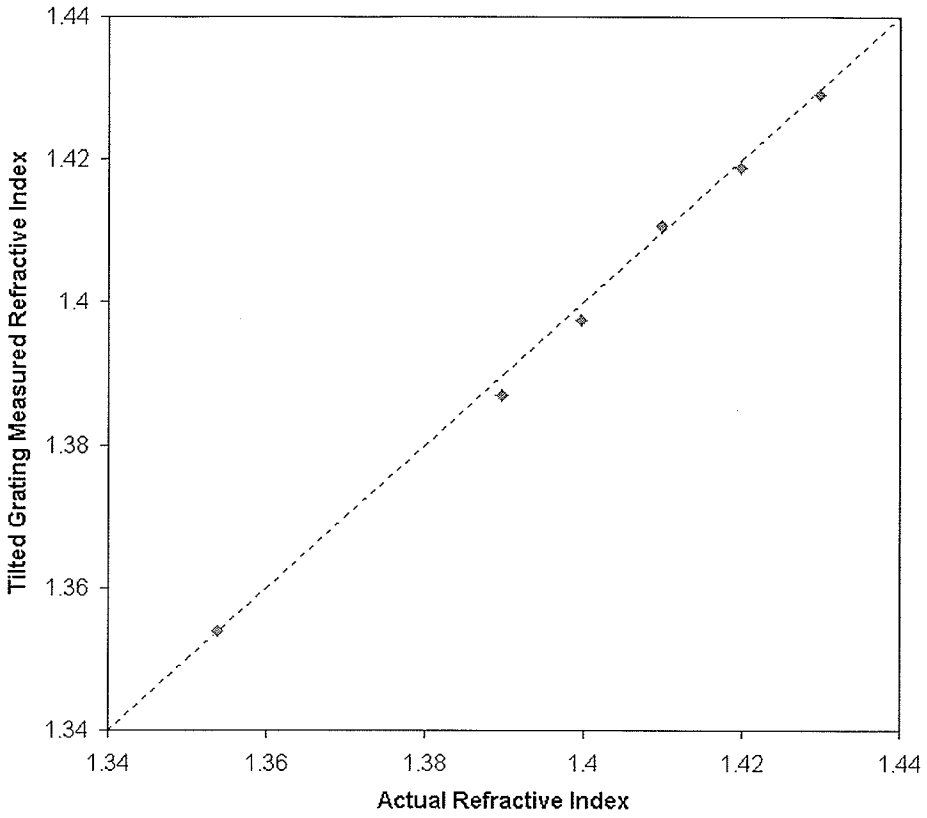

Figure 6.11 Tilted FBG measured refractive index versus actual refractive index.

The slope of the linear fit is very close to 1, meaning that the predicted refractive index values almost exactly matches those of the actual surrounding media. The R^2 value (0.9972) suggests that the standard deviation (or discrepancy) of between the fitted line and the actual data set is very small, meaning that the error is small. This means that if one was given a reference tilted FBG spectrum (when the tilted FBG was surrounded by air only) and an unknown spectrum; one may compare the relative distance shifts between the selected cladding modes and the Bragg resonance to accurately obtain the surrounding refractive index of the unknown spectrum.

Chapter 7

Summary and Conclusion

7.1 Refractive Index Sensitivity Comparison and Enhancement

Sensitivities to surrounding refractive indices for the side-polished fiber Bragg grating and tilted fiber Bragg grating sensors are listed in Table 7.1 for comparison. The wavelength shifts per refractive index unit are listed for more accurate comparison, and the ability to detect changes in the surrounding refractive index depends on the types of interrogation systems used. If both the side-polished and tilted fiber Bragg grating sensors were interrogated with the same system, Micron Optics si720 for example, then the maximum refractive index sensitivities would be 2.38×10^{-4} for the side-polished fiber Bragg gratings (when the surrounding refractive index is near 1.44) and better than 1.53×10^{-4} for the tilted fiber Bragg gratings (for the surrounding refractive index range from 1.38 to 1.43).

Table 7.1 Summary of refractive index sensitivities of the fiber modes analyzed.

Mode	Maximum wavelength shift per refractive index unit (nm/riu)	Repeatability of measurement equipment used (pm)	Smallest Δn_{ext} detected	n_{ext} at which the maximum sensitivity is obtained
SFBG, Bragg	4.20	3	7.14×10^{-4}	1.440
TFBG, cladding mode 8 nm from Bragg	6.54	1	1.53×10^{-4}	1.425
TFBG, cladding mode 14 nm from Bragg	11.80	1	8.44×10^{-5}	1.415
TFBG, cladding mode 23 nm from Bragg	19.80	1	5.01×10^{-5}	1.405

Even though both sensors exhibit similar sensitivities, the tilted fiber Bragg grating sensors can detect a wider range of surrounding refractive index values than the side-polished fiber Bragg gratings at their respective maximum sensitivities. In addition, temperature cross sensitivity becomes problematic in side-polished fiber Bragg gratings if no reference gratings were used; whereas it is negligible in tilted fiber Bragg gratings. Furthermore, no cladding removal was necessary for tilted fiber Bragg gratings yet they demonstrated better refractive index sensitivities than side-polished fiber Bragg gratings.

To enhance the refractive index sensitivity further, one may remove some cladding from the tilted fiber Bragg gratings by chemical etching. Thinner cladding leads to reduced number of cladding modes and increased inter-modal spacing, and it also leads to better evanescent wave coupling to the surrounding media. This is not recommended as noted in the previous chapter that to enhance the sensitivity by a factor of 2, the cladding diameter needs to be reduced from 125 μm to 50 μm. The much reduced mechanical stability outweighs the added benefits. One may increase the tilt angle of the tilted fiber Bragg gratings to achieve maximum sensitivities at shorter wavelengths, which means maximum sensitivities occur at lower surrounding refractive index values. This property of tilted fiber Bragg gratings allow for more choices of the chemical polymer to be deposited on the fiber Bragg grating for chemical sensing purposes as the choice of refractive index value for the polymer is much less restricted. The maximum sensitivity of side-polished fiber Bragg gratings can be enhanced by further reducing the residual cladding thickness, or by etching a slot into the core of the optical fiber along the length of the grating [47].

7.2 Conclusion

Both the side-polished and tilted fiber Bragg gratings demonstrated high surrounding refractive index sensitivities at 7.14×10^{-4} and 1.53×10^{-4} riu, respectively. While the side-polished fiber Bragg gratings showed maximum sensitivity when the surrounding refractive index is near 1.44, the tilted fiber Bragg gratings showed maximum sensitivity over a much wider range of surrounding refractive index values (1.38 to 1.43). The ability to differentiate between the temperature-induced wavelength shift and refractive index induced wavelength shift in tilted fiber Bragg gratings makes them better candidates for sensing purposes as multiple parameters can be measured with one single sensing element. Modifications to the fiber geometry are not necessary when fabricating tilted fiber Bragg grating sensors, thus making them relatively easy to manufacture than the side-polished fiber Bragg grating sensors. Their mechanical strength is also better compared to that of the side-polished fiber Bragg gratings.

7.3 Recommendations for Future Work

Tilted fiber Bragg gratings can also be used for refractive index sensing via surface plasmon with a thin layer of gold deposited on the surface of the fiber along the grating [48]. Tilted fiber Bragg gratings may be side-polished to enhance the surface plasmon coupling into the core and cladding modes and consequently increase its refractive index sensitivity. One may try to side-polish the tilted fiber Bragg gratings and leave the mounting (used for the polishing) attached to the fiber Bragg grating to better protect the sensor. The flat surface after the side-polishing allows for easier metal

deposition and better control of the thin-film thickness. It is beyond the scope of this thesis and thus is only recommended for future work.

To make a fiber optic based corrosion sensor for structural health monitoring, it will involve the use of chemically sensitive polymers. Polymers that selectively react only with the hydroxyl ions (OH^-) or hydrogen ions (H^+) can be deposited as a thin film on top of the fiber grating. These polymers must possess the property that their refractive indices change as the environment's acidity (pH) changes so that the fiber Bragg grating refractive index sensors can be used as corrosion sensors for structural health monitoring purposes.

REFERENCES

[1] R.C. Tennyson, T. Coroy, G. Duck, G. Manuelpillai, P. Mulvihill, D. Cooper, P.W.E. Smith, A.A. Mufti, and S.J. Jalali, "Fiber optic sensors in civil engineering structures," *Canadian Journal of Civil Engineering*, **27**, p 880-889 (2000).

[2] R.C. Tennyson, W.D. Morrison, and G. Manuelpillai, "Intelligent pipelines using fiber optic sensors," *Proceedings of the SPIE*, **vol. 5050**, p 295-304 (2003).

[3] J. Seim, E. Udd, W. Schulz, and H. Laylor, "Composite strengthening and instrumentation of the Horsetail Falls Bridge with long gauge length fiber Bragg grating strain sensors," *Proceedings of the SPIE*, **vol. 3746**, p 196-199 (1999).

[4] A. Iadicicco, S. Campopiano, A. Cutolo, M. Giordano, and A. Cusano, "Nonuniform thinned fiber Bragg gratings for simultaneous refractive index and temperature measurements," *IEEE Photonic Technology Letters*, **17**, p 1495-1497 (2005).

[5] A.L. Triques, M.F. Silva Jr., D.M. Gonzales, J. Celnik, V.G. Schlueter, A.R. D'Almeida, F. Pereira, L.C.G. Valente, A.M. Braga, M.L. Dias, "Fiber Bragg grating sensing for indirect evaluation of corrosion in oil and gas facilities," *Proceedings of the SPIE*, **vol. 5502**, p 283-286 (2004).

[6] T.M. Niemczyk, "Refractive index measurement," in *Physical Methods in Modern Chemical Analysis*, T. Kuwana, ed. (Academic, 1980), **vol. 2**, p 337-400.

[7] V. Bathia, "Applications of long-period gratings to single and multi-parameter sensing," *Optics Express*, **4**, p 457-466 (1999).

[8] S.W. James and R.P. Tatam, "Optical fiber long-period grating sensors: characteristics and application," *Measurement Science and Technology*, **14**, p R49-R61 (2003).

[9] A.N. Chryssis, S.M. Lee, S.B. Lee, S.S. Saini, and M. Dagenais, "High sensitivity evanescent field fiber Bragg grating sensor," *IEEE Photonic Technology Letters*, **17**, p 1253-1255 (2005).

[10] H.J. Patrick, "Analysis of the response of long period fiber gratings to external index of refraction," *Journal of Lightwave Technology*, **16**, p 1606-1612 (1998).

[11] T. Allsop, F. Floreani, K.P. Jedrzejewski, P.V.S. Marques, R. Romero, D.J. Webb, and I. Bennion, "Spectral characteristics of tapered LPG device as sensing element for refractive index and temperature," *Journal of Lightwave Technology*, **24**, p 870-878 (2006).

[12] G. Laffont and P. Ferdinand, "Tilted short-period fiber-Bragg-grating induced coupling to cladding modes for accurate refractometry," *Measurement Science and Technology*, **12**, p 765-770 (2001).

[13] C. Caucheteur and P. Megret, "Demodulation technique for weakly tilted fiber Bragg grating refractometer," *IEEE Photonic Technology Letters*, **17**, p 2703-2705 (2005).

[14] C. Chen, L. Xiong, A. Jafari, and J. Albert, "Differential sensitivity characteristics of tilted fiber Bragg grating sensors," *Proceedings of the SPIE*, **vol. 6004**, pp 600413 (2005).

[15] C.-F. Chan, G.A. Ferrier, D.J. Thomson, T. Coroy, P. Lefebvre, and A. Vincelette, "Evanescent field fiber Bragg grating sensors for index of refraction sensing with applications to structural health monitoring," *Proceedings of the SPIE*, **vol. 6176**, pp 617614 (2006).

[16] C.-F. Chan, C. Chen, A. Jafari, A. Laronche, D.J. Thomson, and J. Albert, "Optical fiber refractometer using narrowband cladding-mode resonance shifts," *Applied Optics*, **47** (1), p. 1142-1149 (2007).

[17] C.-F. Chan, G.A. Ferrier, D.J. Thomson, C. Chen, J. Albert, A. Vincelette, and P. Lefebvre, "Side-polished and tilted fiber Bragg grating sensors for structural health monitoring applications," *Proceedings of the SPIE*, **vol. 6530**, pp 65300F (2007).

[18] A.J. Rogers, "Essential Optics," Chap. 3 in *Optical Fiber Sensors, Vol. 1: Principles and Components*, J.C. Dakin and B. Culshaw, ed. (Artech House, 1988), p 25-106.

[19] F.A. Jenkins and H.E. White, "Reflection," Chap. 25 in *Fundamentals of Optics* (*4th Ed.*), (McGraw-Hill, 1976), p 523-43.

[20] M.V. Klein and T.E. Furtak, "Optics of Planar Interfaces," Chap. 2 in *Optics* (*2nd Ed.*), (John Wiley & Sons, 2001), p 59-121.

[21] E. Hecht, "The Propagation of Light," Chap. 4 in *Optics* (*2nd Ed.*), (Addison-Wesley, 1987), p 79-121.

[22] M. Born and E. Wolf, "Basic properties of the electromagnetic field," Chap. 1 in *Principles of Optics: Electromagnetic Theory of Propagation, Interference, and Diffraction of Light* (*7th Ed.*), (Cambridge University Press, 1999), p 1-70.

[23] M.N.O. Sadiku, "Electromagnetic Wave Propagation," Chap. 10 in *Elements of Electromagnetics* (*3rd Ed.*), (Oxford University Press, 2001), p 410-464.

[24] A. Gaston, F. Perez, and J. Sevilla, "Optical fiber relative-humidity sensor with polyvinyl alcohol film," *Applied Optics*, **43** (21), p 4127-4132 (2004).

[25] T.L. Yeo, S. Tong, K.T.V. Grattan, D. Parry, R. Lade, B.D. Powell, "Polymer-coated fiber Bragg grating for relative humidity sensing," *IEEE Sensors Journal*, **5** (5), p 1082-1089, 2005.

[26] K.O. Hill, Y. Fujii, D.C. Johnson, and B.S. Kawasaki, "Photosensitivity in optical fiber waveguides: application to reflection filter fabrication," *Applied Physics Letters*, **7**, p 647-649 (1978).

[27] A. Othonos and K. Kalli, "Properties of Fiber Bragg Gratings," Chap. 3 in *Fiber Bragg Gratings: Fundamentals and Applications in Telecommunications and Sensing*, (Artech House, 1999), p 95-147.

[28] P. St. J Russell, J.L. Archambault, and L. Reekie, "Fibre gratings," *Physics World*, **6** (10), p 41-46 (1993).

[29] V. Mizrahi and J.E. Sipe, "Optical properties of photosensitive fiber phase gratings," *IEEE Journal of Lightwave Technology*, **11**, p 1513-1517 (1993).

[30] H. Kogelnik and C.W. Shank, "Coupled wave theory of distributed feedback lasers," *Journal of Applied Physics*, 43, p 2327-2335 (1972).

[31] A. Yariv, "Coupled-mode theory for guided-wave optics," *IEEE Journal of Quantum Electronics*, **QE-9**, p 919-933 (1973).

[32] A. Othonos and K. Kalli, "Fiber Bragg Grating Theory," Chap. 4 in *Fiber Bragg Gratings: Fundamentals and Applications in Telecommunications and Sensing*, (Artech House, 1999), p 189-222.

[33] K.O. Hill and G. Meltz, "Fiber Bragg grating technology fundamentals and overview," *IEEE Journal of Lightwave Technology*, **15**, p 1263-1276 (1997).

[34] T. Erdogan, "Cladding-mode resonances in short- and long-period fiber grating filters," *Journal of the Optical Society of America A*, **14**, p 1760-1773 (1997).

[35] T. Erdogan and J.E. Sipe, "Tilted fiber phase gratings," *Journal of the Optical Society of America A*, **13**, p 296-313 (1996).

[36] T. Erdogan, "Fiber grating spectra," *IEEE Journal of Lightwave Technology*, **15**, p1277-1294 (1997)

[37] K. Schroeder, W. Ecke, R. Mueller, R. Willsch, and A. Andreev, "A fiber Bragg grating refractometer," *Measurement Science and Technology*, **12** (7), p 757-764 (2001).

[38] Technical specifications for fused silica (Technical products division, Advanced Products Department, Corning Inc. MP-21-4, Corning, N.Y. 14831).

[39] C.L. Liou, L.A. Wang, M.C. Shih, "Characteristics of hydrogenated fiber Bragg gratings," *Applied Physics A (Material Science Processing)*, **A64** (2), p 191-197 (1997).

[40] K.O. Hill, B. Malo, F. Bilodeau, D.C. Johnson, and J. Albert, "Bragg gratings fabricated in monomode photosensitive optical fiber by UV exposure through a phase mask," *Applied Physics Letters*, **62**, p 1035-1037 (1993).

[41] C. Shafai, M.J. Brett, J.N. Broughton, "Passivation and performance analysis of thin film Peltier heat pumps," *Journal of Vacuum Science & Technology A: Vacuum, Surfaces, and Films*, **17** (1), p 306-309 (1999).

[42] L. Fuller, (2006), "Wet Etch for Microelectronics," Microelectronic Engineering, Rochester Institute of Technology, April 2007. www.rit.edu/~lffeee/wet_etch.pdf

[43] Semiconductor & Microsystems Fabrication Laboratory (2007), "Wet etch rates," Rochester Institute of Technology, April 2007. smfl.microe.rit.edu/Process%20Information/Film%20Etch%20Rates.htm

[44] D.R. Lide (Editor), CRC Handbook of Chemistry and Physics, 86th Edition. © CRC Press, 2005.

[45] E. Rivera, "Improving Fiber Bragg Grating Strain Measurements Using Peak Location Algorithms and Wavelength References," M.Sc. Thesis, University of Manitoba, 2004.

[46] High resolution swept wavelength laser interrogator, Model Si720, from Micron Optics Inc., Atlanta, Ga.

[47] T. Baehr-Jones, M. Hochberg, G. Wang, R. Lawson, Y. Liao, P.A. Sullivan, L. Dalton, A.K.-J. Jen, and A. Scherer, "Optical modulation and detection in slotted silicon waveguides," *Optics Express*, 13 (14), p 5216-5226 (2005).

[48] Y.Y. Shevchenko and J. Albert, "Plasmon resonances in gold-coated tilted fiber Bragg gratings," *Optics Letters*, **32** (1), p 211-213 (2007).